Advanced OFDM Receivers for Underwater Acoustic Communications

Jianghui Li

Doctor of Philosophy

University of York
Electronics

November 2016

Abstract

In underwater acoustic (UWA) communications, an emerging research area is the high data rate and robust transmission using multi-carrier modulation, such as orthogonal frequency-division multiplexing (OFDM). However, difficulties in the OFDM communications include Doppler estimation/compensation, beamforming, and channel estimation/equalization. In this thesis, to overcome these difficulties, advanced low complexity OFDM receivers of high performance are developed. A novel low complexity Doppler estimation method based on computing multi-channel autocorrelation is proposed, which provides accurate Doppler estimates. In simulations and sea trials with guard-free OFDM signal transmission, this method outperforms conventional single-channel autocorrelation method, and shows a less complexity than the method based on computing the cross-ambiguity function between the received and pilot signals with a comparable performance. Space-time clustering in UWA channels is investigated, and a low complexity multi-antenna receiver including a beamformer that exploits this channel property is proposed. Various space-time processing techniques are investigated and compared, and the results show that the space-time clustering demonstrates the best performance. Direction of arrival (DOA) fluctuations in time-varying UWA channels are investigated, and a further developed beamforming technique with DOA tracking is proposed. In simulation and sea trials, this beamforming is compared with the beamforming without DOA tracking. The results show that the tracking beamforming demonstrates a better performance. For the channel estimation, two low complexity sparse recursive least squares adaptive filters, based on diagonal loading and homotopy, are presented. In two different UWA communication systems, the two filters are investigated and compared with various existing adaptive filters, and demonstrate better performance. For the simulations, the *Waymark* baseband UWA channel model is used, to simulate the virtual signal transmission in time-varying UWA channels. This model is modified from the previous computationally efficient *Waymark* passband model, improving the computational efficiency further.

Contents

List of Figures

List of Tables

Acknowledgements

I would like to express my great thanks particularly to my supervisor, Dr. Yuriy V. Zakharov, for all his guidance, advice, and inspiration throughout the course of my Ph.D. study.

I am very grateful to Dr. Paul Mitchell, who is my thesis advisor. Paul provided a lot of ideas and helped me a lot especially during the beginning of my Ph.D. study.

I would also like to thank Mr. Bemjamin Henson for his effective cooperation, and all my other colleagues in the Communications Research Group.

To the MTS/IEEE OCEANS'16 Shanghai Organizing Committee, who gave me a much treasured opportunity to be a Session Chair in the conference.

To the IEEE Signal Processing Society (SPS), who awarded me one of the SPS travel grants for attending the IEEE SAM 2016 conference.

To the IEEE Oceanic Engineering Society (OES) Scholarship Committee, who awarded me the first OES Scholarship in UK, making both University of York and myself very proud of it.

This thesis is dedicated to my parents who always show their love to me, understand me, support and encourage me, and give me confidence all the time.

Declaration

All work presented in this thesis as original is so, to the best knowledge of the author. Acknowledgements and references to other researchers have been given as appropriate.

Some of the research presented in this thesis has resulted in some publications. These publications are listed as below.

Journal Papers

1. J. Li, Y. V. Zakharov and B. Henson, "Multi-channel autocorrelation method for Doppler estimation in UWA channels", *IEEE Journal of Oceanic Engineering*, 2016, submitted.

2. J. Li and Y. V. Zakharov, "Efficient use of space-time clustering for UWA OFDM communications", *IEEE Journal of Oceanic Engineering*, 2016, second review round.

Conference Papers

1. J. Li, "DOA tracking in time-varying underwater acoustic communication channels", *IEEE Oceans'17*, *Aberdeen*, *UK*, 2017, submitted.

2. J. Li and Y. V. Zakharov, "Sliding-window homotopy adaptive filter for estimation of sparse UWA channels", *The Ninth IEEE Sensor Array and Multichannel Signal Processing Workshop (SAM)*, *Rio de Janeiro*, *Brazil*, pp. 1-4, 2016.

3. J. Li and Y. V. Zakharov, "Sliding window adaptive filter with diagonal loading for estimation of sparse UWA channels", *IEEE Oceans'16*, *Shanghai*, *China*, pp. 1-5, 2016.

4. J. Li, L. Liao and Y. V. Zakharov, "Space-time cluster combining for UWA communications", *IEEE Oceans'16*, *Shanghai*, *China*, pp. 1-6, 2016.

5. Y. V. Zakharov and J. Li, "Autocorrelation method for estimation of Doppler parameters in fast-varying underwater acoustic channels", *Underwater Acoustic Conference and Exhibition* (*UACE*), *Crete*, *Greece*, pp. 1-6, 2015.

6. B. Henson, J. Li, Y. V. Zakharov and C. Liu, "Waymark baseband underwater acoustic propagation model", *IEEE Underwater Communications and Networking* (*UComms*), *Sestri Levante*, *Italy*, September, pp. 1-5, 2014.

Chapter 1

Introduction

Contents

1.1 Underwater Acoustic Communications

For millions of years, in the vast oceans, some marine mammals like dolphins and whales have used acoustic waves as a way of communicating with each other. In recorded human history, around 350 years B.C., Aristotle noted that humans can hear sound in water as well as in the air [5]. In 1490, Leonardo da Vinci observed that the sound of ships can be heard at great distances underwater [6]. In 1743, Abbé J. A. Nollet conducted a series of trials, and verified that sound can travel underwater, even easier than that travels in the air [7].

It is not until the Second World War, for military purposes, the underwater wireless communication technique started to develop [8], eliminating physical connection of tethers. After the War, underwater communications started to extend into commercial fields. In recent years, the demand for it has motivated extensive research in a growing number of oceanic applications, e.g., discovery of new resources, marine and oceanographic research, marine commercial operations, speech transmission between divers, remote control in off-shore oil industry, scientific data collection from ocean-bottom stations, control of surface vessels, unmanned or autonomous underwater vehicles (UUVs, AUVs), ocean floor mapping, pollution monitoring in environmental systems, and so on [9, 10]. Driven by these demands, the utilisation of underwater communications will likely experience a surge in the near future.

Currently, for employing such wireless communications, three completely different underwater wireless waves are commonly used, which are: radio waves, optical waves, and acoustic waves. The radio waves are commonly used for communication in the air, due to their fast-speed propagation and wide available frequency spectrum as well as their capability of propagation without medium. The optical waves are commonly used for their small propagation delay and high possible data rates. However, the radio waves suffer from tremendous attenuation, i.e., require large antennas and high power for transmission, only over short distances (usually at ranges of just a few metres) underwater [9]. The optical waves are severely scattered in a few hundred metres in water mediums [9]. Acoustic waves, on the contrary, are attractive for underwater communications, due to their capability of propagating over distances as large as hundreds or even thousands of miles [9].

Even though the acoustic waves possess the significant merit in underwater communications, they also offer a great deal of challenges, due to issues like [10–15]:

1. Doppler effect, induced by the motion of the transmitter, the receiver, and the propagation medium with a low propagation speed of sound (normally 1.5 km/s);
2. multipath propagation, induced by reflections on the sea surface and bottom, refraction of sound waves, scattering from inhomogeneities in the water column, resulting in intersymbol interference, signals spreading (typically tens of milliseconds) and frequency-selective signal distortion;
3. time-variation, from the ocean surface waves, internal waves, turbulence, and tides;
4. small available bandwidth, from roughly 1 to 100 kHz;
5. ocean noise from numerous mechanisms, including weather, surface wave action, marine life, shipping, and off-shore industry;
6. geometrical shadow zones, where no acoustic power is transferred to, bent by uneven speed of sound in a designated direction;

7. strong signal attenuation, due to absorption, i.e., transfer of acoustic energy into heat, especially for high frequencies over long distances.

The aforementioned issues reach a point, where the design of a single communication system that is capable of handling all these issues seems hopelessly complicated. Accordingly, to exploit and minimize these issues, advances in techniques of underwater acoustic (UWA) communications have been made in the past few decades, especially in terms of UWA communication channel modelling and system design. Underwater channel models, e.g., the *VirTEX* model [16], and the *Waymark* model [1] have been developed and applied to UWA communications for simulating the acoustic propagation in real underwater environments; multiple multi-carrier modulation schemes have been used for UWA communications [10, 17, 18]; multi-antenna systems were demonstrated [19–22] for UWA communications especially in low signal-to-noise ratio (SNR); adaptive channel estimators [19, 23] were proposed to improve UWA channel estimation performance; and so on.

However, high demands in reliable UWA communication schemes call for more effective techniques, some of these techniques are being improved, in terms of throughput, performance, and robustness. Examples can be listed like the development of advanced signal processing algorithms, such as Doppler estimation and compensation algorithms [24–29], and sparse channel estimation algorithms [17, 30–34]; the development of direction of arrival (DOA) estimation and beamforming algorithms, such as the fractional delay beamforming algorithm [35]; the design of adaptive multi-carrier modulation, such as guard-free orthogonal frequency-division multiplexing (OFDM) [4]; and so on.

1.2 Underwater Acoustic Signal Processing Techniques

Originally, signal processing techniques were developed for terrestrial wired and wireless channels in the air [14]. For suiting UWA channels, these techniques need significant modifications [14]. The research area of UWA signal processing began with development efforts can date back to the late 1910's, when the manned submarines were developed and the need to communicate with them [14]. The UWA signal processing emerged as a distinct discipline in its own right until many articles in UWA communications published in the past decades.

Some articles deal primarily with basic architectures and algorithms for UWA channel modelling [1,36], Doppler estimation [26], array processing [37,38], and adaptive filtering [12,25], with many of them considering real underwater environment and emphasizing practical applications [11].

However, for reliable UWA communications, there are many problems, involving severe Doppler effect, complicated channel multipath, and fast time-varying underwater environment. The unknown underwater environment represents some of the most difficult problems in demodulating received data. Some components in UWA channels must be estimated, such as Doppler shift; some components can be learned, such as space-time clustering; and some components are changing in an unknown manner and therefore should be tracked, such as time-varying DOAs. Quite frequently, all of these components exist in UWA signal processing. However, the research of the UWA signal processing provides approaches for removing distortions resulted from the complicated UWA channels, as well as extracting information about unknown UWA channels [39].

In UWA communication channels, the distortions are often present. Examples are as follows.

1. Doppler effect, which is a common problem in UWA channels, induced by the transmitter/receiver motion and time-varying water column. This presents a severe effect and can degrade the detection performance of an underwater receiver.
2. In a long distance UWA communication, the detection performance of a multi-antenna receiver is usually depending on the combination of received signals from array elements directly. However, it is often difficult for the receiver to achieve a good performance especially with a low SNR, and the complexity can be high.
3. Multipath propagation, resulted from refraction, reflection and scattering in complicated time-varying underwater physical environment, affects the communication data to a great extent or even distorts the original data severely.

Other examples can also be presented, but the three examples above are sufficient to illustrate some of the main reasons for the requirement of advanced signal processing in UWA communications. In the first example above, with the time-varying ocean surface/internal waves or platforms motion, the Doppler effect is usually unavoidable. Therefore, to remove the distortion and demodulate the data effectively, the Doppler effect must be estimated accurately. Also, other problems, such as high complexity, or inaccurate compensation of Doppler shift, are also need to be solved. Therefore, low complicated and effective Doppler estimation/compensation methods, that are capable of estimating and compensating for fast time-varying Doppler shift, are important signal processing techniques which need to be developed.

The second example above concerns DOA estimation and beamforming. In the UWA channels, spatial signals are usually analysed by DOA estimation with multi-element vertical linear array (VLA). In order to separate the spatial signals, beamforming techniques are often applied. The power of spatial signals from different angles are usually different, which indicates different SNRs. Maximizing the SNR of spatial signals offers better performance of the receiver. Moreover, by distinguishing different arrivals, a beamformer makes it possible to apply different Doppler shifts and delay spreads to each arrival, which potentially maximizes performance and reduces complexity of the receiver. Therefore, developing efficient beamforming techniques as well as optimizing equalizers, are key factors to maximize the performance of the receiver.

The third example above concerns the channel estimation. The UWA communication channel is characterized by complicated multipath [12]. For example, when the transmitter is moving (e.g., towed by a surface vessel) during the data transmission, the underwater propagation paths between the transmitter and receiver are changing, sometimes rapidly. In such conditions, problems like data symbol timing, and propagation loss, are unknown to the communication system. Therefore, designing a flexible and robust channel estimator, which is capable of handling the wide range of possible solutions of these problems, is necessary for improving quality of the UWA communication system.

Recent developments in UWA communications have made it clear that significant performance improvement can be achieved by using advanced signal processing techniques, e.g., Doppler estimation algorithms [24–28], antenna array beamforming algorithms [35, 40, 41], sparse adaptive filtering algorithms [17, 23, 31], adaptive equalization algorithms [12, 42–46] and direct spread spectrum techniques [47–51]. An insight into some of the UWA signal processing techniques will be provided, and some new effective techniques of solving distortion problems and producing desired results will be developed, with an emphasis on complexity reduction and performance improvement.

1.3 OFDM Signal Transmission in Underwater Acoustic Channels

OFDM [52] has emerged as one of the attractive techniques for the signal transmission in multipath channels [18]. Originally, OFDM was adopted in radio communication systems as an efficient technique to attain high data rate transmission with high bandwidth efficiency in frequency selective fading channels [53]. It divides the available channel into a number of closely-spaced narrowband sub-channels, with each sub-channel orthogonal to all the others. The number of sub-channels is chosen to generate a sufficiently small spacing sub-carrier, such that the frequency response in each sub-carrier can be considered flat. Each sub-carrier can be modulated with a conventional modulation scheme at a low symbol rate [54].

In an OFDM system, each sub-channel is processed independently from all the others, making OFDM capable of coping with severe channel conditions such as multipath and narrowband interference, and therefore simplifies the channel equalization and demodulation algorithms. Moreover, it offers easy reconfiguration for use with different bandwidths, and requires low computational complexity based on fast Fourier transform (FFT) signal processing. Due to these significant merits, in recent years, OFDM has been considered as a promising technique for high data rate transmission in UWA channels, providing robustness against frequency selective fading [15, 55–59].

Even though OFDM has such merits, it is still a challenging task to apply OFDM in UWA channels due to its sensitivity to frequency shift in underwater. Also, because of the non-negligible bandwidth of the acoustic signals with respect to the centre frequency, Doppler effects induced by the relative motion result in such problems as the non-uniform frequency shift across the signal bandwidth and intercarrier interference [23, 59].

To achieve high spectral efficiencies, in this thesis we consider guard-free OFDM signals with superimposed data and pilot symbols [1, 31, 60, 61]. Guard-free OFDM symbols do not have any guard interval, such as cyclic prefix or zero padding. The duration of the OFDM symbol is the same as the orthogonality interval, and the OFDM symbols are transmitted one-by-one. A binary pseudo-random sequence of the same length as the OFDM symbol, serves as the superimposed pilot signal; this is the same in all OFDM symbols. In the UWA communication channels, the using of the guard-free OFDM signals with superimposed data and pilot symbols is considered to benefit the spectral efficiency [4, 62].

Multiple sea trials with data transmission using guard-free OFDM signals, were carried out by the Acoustics Institute (Moscow) in the Pacific and Indian Oceans in 1987-1989 [57,60,63]. In these sea trials, the guard-free OFDM signals were transmitted by a moving underwater transducer at low (≈ 0.5 m/s) to high (6 to 8 m/s) speeds. Antenna arrays were used for receiving the signals. Distances between the transducer and the receiver varied from 30 to 110 km.

1.4 Underwater Acoustic Channel Models

For assessing the signal processing techniques in UWA communication channels, experimental data are required. Sea trials are the ultimate means of collecting experimental data and assessing the techniques performance [1]. However, the sea trials are confined to expensive and lengthy experimental preparation. Also, in some situations, the parameters are difficult if not impossible to control. Instead, the simulation of the propagation channel can be applied. Therefore, designing an UWA channel model, that is capable of modelling underwater acoustic signal transmission in similar conditions, is clearly desirable.

Modelling acoustic signal transmission underwater is a difficult problem, taking into consideration the specific time-varying Doppler spreading and multipath propagation due to the complicated motion of a transmitter and receiver, giving severe signal distortions [64]. The effect of the relatively slow propagation of sound through water is that the Doppler effect in UWA communications is a significant factor in performance [36]. This is especially an issue when the specific time-varying multipath propagation is taken into consideration due to the complicated motion of a receiver and transmitter.

For such a virtual signal transmission, i.e., the transmission that mimics a real sea trial, the

VirTEX underwater propagation channel model was developed [65] and used [66]; this model is based on the *Bellhop* ray/beam tracing [67] to compute the channel impulse response in different acoustic propagation environments. A similar approach was implemented in the *Waymark* model [1] developed to efficiently simulate the UWA signal transmission in long communication sessions, potentially allowing for less computation. However, the passband signal processing in the *Waymark* model developed in [1] can be replaced by baseband signal processing, which would potentially reduce the complexity further.

1.5 Motivation and Contributions

1.5.1 Motivation

Advanced signal processing techniques are essential for UWA communications. Developing such techniques will improve our ability to communicate and exchange information in UWA channels, and is essential for underwater applications in marine research, oceanography, marine commercial operations, autonomous underwater vehicle (AUV) design, the off-shore oil industry, and defence [10]. In recent years, many signal processing techniques for UWA communications have been developed. However, researchers in UWA communications are still facing challenges. The aim of this thesis is to build high data rate robust UWA communication systems, more specifically, developing advanced signal processing techniques for such systems.

Guard-free OFDM transmission allows high data rate communications underwater. However, receivers in guard-free UWA communication systems can be complex, and so far only single-antenna receivers are known in the literature; the single-antenna configuration has a limited performance [4]. The key signal processing techniques that define the complexity and performance of the receiver are the Doppler estimation and compensation, channel estimation and equalization, and the antenna array beamforming. In this thesis, new techniques will be developed for Doppler estimation, channel estimation and beamforming that reduce the complexity of the receiver, while keeping or improving its performance.

1.5.2 Major contributions

The major contributions of this thesis are summarized as follows.

1. The *Waymark* UWA channel model [1], based on an approach for setting waymark sampling interval, is modified for acoustic signal propagation underwater, that processes signals in the baseband. The baseband model processes signals at a low sampling rate. Therefore, the computational complexity of the model is reduced. Moreover, the performance of it is comparable to that of a relatively mature UWA channel model *VirTEX* [16].

2. A multi-channel autocorrelation (MCA) method is proposed for Doppler estimation. The method can be used in communication systems with periodically transmitted pilot signals or repetitive data transmission. This method requires a small number of Doppler estimation channels, which provides low computational complexity, while providing accurate Doppler estimation.

3. Space-time clustering in UWA channels is illustrated, and space-time clusters combining is proposed to improve detection performance and reduce the computational complexity of a receiver. Based on the illustrated space-time clustering, a spatial filter is proposed for DOA estimation, beamforming and producing directional signals. The angles for producing directional signals are based on the discrete space-time clusters, which usually results in a small number of diversity branches of the receiver. Based on the delay spread estimation of a directional signal, an equalizer length is optimized to reduce the computational complexity of each diversity branch. Moreover, due to the Doppler-delay spread of signals in a single cluster is smaller than that in multiple clusters, extra performance improvement can be achieved with a reduced complexity.

4. The time-varying UWA channels are exploited with DOA estimation, and a beamforming technique with DOA tracking is proposed to produce directional signals in time-varying UWA communication channels. In the channels, the DOAs are often varying rapidly within small angular intervals, which are usually produced mostly by moving boundaries (ocean surface), internal waves and drifting hydrophones/sensors. Based on the proposed beamforming technique with DOA tracking, a receiver shows capability

of tracking the time-varying DOA and demonstrates better detection performance than that without DOA tracking.

5. Two sliding-window sparse recursive least squares (RLS) adaptive filters, based on diagonal loading and homotopy, are proposed and used in UWA channel estimator. They are used for UWA sparse impulse response estimation. Sea trial results suggest that the two proposed sparse RLS adaptive filters achieve better performance than the classic and existing sparse RLS adaptive filters used for comparison.

1.6 Thesis Outline

This thesis is organized into seven chapters and one appendix. It develops advanced signal processing techniques in UWA communications. Following the introduction in Chapter 1, Chapter 2 describes the *Waymark* baseband propagation channel model. Chapter 3 proposes the multi-channel autocorrelation method for Doppler estimation. Chapter 4 investigates the space-time clustering of the channel propagation and applies it to the receiver design. Chapter 5 contains the DOA fluctuation analysis and the beamforming technique with DOA tracking in the receiver. Chapter 6 proposes and compares various RLS adaptive filters in UWA channel estimators for sparse channel estimation. Chapter 7 provides a summary of this thesis, conclusions and suggestions for future work. More specifically, the context of the chapters is as follows.

Chapter 2 presents the *Waymark* baseband UWA channel model, which extends the work in [1] where a computationally efficient underwater passband propagation channel model is described. The extended model creates a time-varying channel model as a baseband equivalent representation, allowing the signal propagating through the channel at baseband frequencies. Due to the processing in baseband is performed at a lower sampling rate than that in passband, the simulation time is reduced. In addition, longer channel impulse responses can be modelled with the same resources, giving the model the ability to accommodate more complicated and extreme underwater environments.

Chapter 3 presents the MCA Doppler estimation method in UWA channels. This method provides accurate Doppler estimates with a low complexity. This method can be used in communication systems with periodically transmitted pilot signals or repetitive data transmission. The MCA method is compared with conventional single-channel autocorrelation (SCA) method and the method based on computing the cross-ambiguity function (CAF) between the received and pilot signals. The comparisons are performed using simulation data in four shallow water scenarios and sea trial data in two deep water scenarios. The results demonstrate that the proposed MCA method outperforms the SCA method and comparable in the performance with the CAF method.

Chapter 4 investigates space-time clustering in UWA channels, and proposes a receiver that exploits the space-time clustering. The proposed receiver is designed for an UWA communication system with guard-free OFDM signals and superimposed pilot signals, and a VLA of hydrophones. Various space-time processing techniques are investigated and compared. The results show that the space-time clustering demonstrates the best performance with a relatively low complexity. The comparison has been done using signals transmitted by a fast moving transducer, and recorded on a 14-element VLA in a sea trial at a distance of 105 km.

Chapter 5 investigates the DOA fluctuation in the time-varying UWA channels, and proposes a beamforming technique with DOA tracking in the receiver. The DOA fluctuation is investigated from the ocean dynamics, including surface and internal waves. Taking into account the fluctuation, a beamforming technique with DOA tracking is proposed and used in a receiver. The receiver with DOA tracking demonstrates an improved detection performance than that without DOA tracking. The comparison is based on data recorded on a 14-element non-uniform VLA, in a simulation at a distance of 80 km, and in two sea trials at distances of 30 km and 105 km.

Chapter 6 presents two RLS adaptive filters for sparse identification of UWA channels. The first adaptive filter is based on sliding-window, diagonal loading, and dichotomous coordinate descent (DCD) iterations. It has a complexity that is only linear in the filter length. The adaptive filter is used for channel estimation in an UWA communication system with the transmission of guard-free OFDM signals and superimposed pilot symbols. A LMS adaptive filter and various RLS adaptive filters are investigated and compared. The results show that the proposed sliding-window sparse RLS adaptive filter with diagonal loading demonstrates the best performance. We also show that adaptive filters with a sliding-window outperform adaptive filters with an exponential-window. The comparison has been done using signals recorded in a sea trial at a distance of 80 km transmitted by a fast moving transducer, resulting in fast-varying channels. In these conditions, a low-error-rate transmission is achieved at a spectral efficiency of 0.5 bps/Hz. The second adaptive filter is based on sliding-window, homotopy, and DCD iterations. It is used in a multi-antenna receiver of an UWA communication system with guard-free OFDM signals and superimposed pilot symbols. More specifically, it is used for channel estimation in the channel-estimate-based equalizer. We compare the proposed sliding-window homotopy RLS adaptive filter with exponential-window homotopy and classic RLS algorithms. The results show that the proposed algorithm provides an improved performance compared to other adaptive filters. The comparison is based on signals recorded on a 14-element vertical antenna array in a sea trial at a distance of 105 km transmitted by a fast moving transducer. In these conditions, error-free transmission is achieved with a spectral efficiency of 0.33 bps/Hz.

Finally, Chapter 7 presents the main conclusions of this thesis, and ideas for future work are discussed.

Chapter 2

Waymark Baseband UWA Propagation Channel Model

Contents

2.1 Introduction

It is difficult to model acoustic wave propagation underwater, due to distortions from severe Doppler spreading and multipath [64]. The relatively slow propagation of sound through water makes the Doppler effect significant in performance of UWA communications [36]. This is especially apparent when the specific time-varying multipath propagation is taken into consideration due to the complicated motion of a transmitter/receiver. It is clearly desirable to be able to make a computer simulation of the propagation of an acoustic signal through the ocean, especially for testing signal processing algorithms for UWA communications. Not only are sea trials expensive and time consuming, but also the parameters are difficult if not impossible to control, therefore trying out different design ideas in similar conditions or environments becomes infeasible.

Currently, a number of approaches to deal with this problem have been presented in literatures, for example using a static channel impulse response [15] obtained from acoustic field computation [68, 69], or a model based on random fluctuations of complex amplitudes of eigenpaths. Some models approximate the Doppler effect by introducing frequency shifts in eigenpaths and statistical model for multipath amplitudes [70]. Other approaches are based on direct replay using a measured time-varying channel response [71], random local displacements [66], and so on.

Among these approaches, a promising one for dealing with this problem is the 'virtual' signal transmission [16,65]. For such a virtual signal transmission, i.e., the transmission that mimics a real sea trial, the *VirTEX* underwater propagation channel model was developed [65] and used [66]; this model is based on the *Bellhop* ray/beam tracing [67] to compute the channel impulse response in different acoustic propagation environments. A similar approach was implemented in the *Waymark* model [1] developed in this research group to efficiently simulate the UWA signal transmission in long communication sessions, potentially allowing for less computation. However, the passband signal processing in the *Waymark* model developed in [1] can be replaced by baseband signal processing, which would potentially reduce the complexity further.

A new *Waymark* model described in this chapter with the aim to further reduce the computational complexity is developed by my colleague Mr. Benjamin Henson. The new developed model uses baseband processing for modelling the signal transmission. The author verifies the new developed model with three simulations, and use the new model to model the signal transmission for designing UWA receivers in the following paragraphs.

2.2 Underwater Channel Simulation

A received signal in a time-varying linear channel may be described in the general case by [72] without considering noise:

$$y(t) = \int_{-\infty}^{\infty} h(t,\tau)s(t-\tau)d\tau, \quad t \in [0, T_{sig}], \tag{2.1}$$

where $h(t,\tau)$ is the impulse response of the channel, $s(t)$ is the transmitted signal, T_{sig} is the signal duration. At time t the baseband channel impulse response may be represented as the sum of multipath components [73] given by:

$$h(t,\tau) = \sum_{p=1}^{L} c_p(t)\delta(\tau - \tau_p(t)), \tag{2.2}$$

where

$$c_p = A_p(t)e^{-j2\pi f_c \tau_p(t)}, \tag{2.3}$$

L is the multipath components, c_p is the complex amplitude of path p, $j = \sqrt{-1}$, $\tau_p(t)$ is the time-varying delay for path p, $A_p(t)$ is the time-varying complex amplitude for path p, f_c is the signal carrier frequency. The delay $\tau_p(t)$, would be affected by the path geometry, which would encompass any movement in the system ultimately representing the Doppler effect.

In the passband *Waymark* model [1], the impulse response are calculated for a set of points or waymarks along the transmitter/receiver trajectory. The relative delay in the impulse responses between these points is then estimated, allowing the shape of the impulse response and the delays to be interpolated separately, giving an improved result.

Different from the *Waymark* model, the *VirTEX* model [16] uses a regularly spaced grid to describe the water volume that the signal propagates through. The model interpolation is performed on the amplitude and time of arrivals of the multipath components. An interpolated point between the grid points is the weighted sum of the arrivals at the four surrounding points. So, for instance, if there were two multipath arrivals at each of the surrounding grid points then the interpolated point would comprise of eight multipath arrivals. The delays are adjusted according to the local speed of sound, the geometric distance and incident angle from the interpolated point to the grid point. The *VirTEX* system also includes an ocean surface wave model, however for our experiment it is set up as a flat surface.

In the chapter both the *Waymark* and *VirTEX* models use the *Bellhop* ray-tracing program [67] to simulate the physics of the propagation. Other simulators could be used, however the *VirTEX* model is restricted to a ray traced input. The *Waymark* model can use any model that can produce a frequency response. This would perhaps be more versatile for lower frequency signals and more complicated bottom profiles where normal-mode models such as KRAKEN [68] may be more appropriate.

From the passband discrete form convolution the baseband signal is given by:

$$y_e(nT_s) = \sum_{i=0}^{I-1} h(nT_s, iT_s)s_e(nT_s - iT_s), \quad n = 0, \ldots, N-1, \tag{2.4}$$

where $s_e(nT_s)$ can be approximated by:

$$s_e(nT_s) = \sum_{k=0}^{K-1} \left[s(kT_s)e^{-j2\pi f_c kT_s}\right] r(nT_s - kT_s), \tag{2.5}$$

and the $r(nT_s)$ is given by [74]:

$$r(nT_s) = \text{sinc}(f_0 nT_s)\frac{\cos(\pi f_0 \alpha nT_s)}{1 - (2f_0 \alpha nT_s)^2}, \tag{2.6}$$

$y_e(nT_s)$ is the baseband output signal, $s_e(nT_s)$ is the baseband equivalent signal, T_s is the sample period, I is the number of channel taps in the channel finite impulse response (FIR) filter, $N = T_{sig}/T_s$, $r(nT_s)$ is the raised cosine low pass filter impulse response, K is the raised cosine filter length, f_0 is the upper bound of baseband bandwidth, and α is the roll-off factor.

The original signal spectrum is shifted to centre around zero and a low pass filter (LPF) applied. The LPF chosen is a raised cosine filter [75]. Once the signal has been moved to be the baseband equivalent then the sampling frequency may, with reference to the baseband bandwidth, be decimated from T_s to give a lower sample period T_d.

Figure 2.1 shows a diagram of the system with the development from the original system in [1]. In this development the waymark impulse response is created in the baseband, in addition the input signal is converted to a downsampled baseband signal and passed through the time-varying delay and time-varying FIR filter. The splitting of the channel into these two components allows a more accurate interpolation of the channel impulse response (for more details see [4]) between waymarks, thus increasing the waymark interval and consequently reducing the computation. However, the time-varying delay requires a phase correction when upshifting the signal as shown in Figure 2.1.

The bandlimited channel frequency response at waymark m is generated from multipath arrivals with their respective excess delays and baseband equivalent complex amplitudes. As

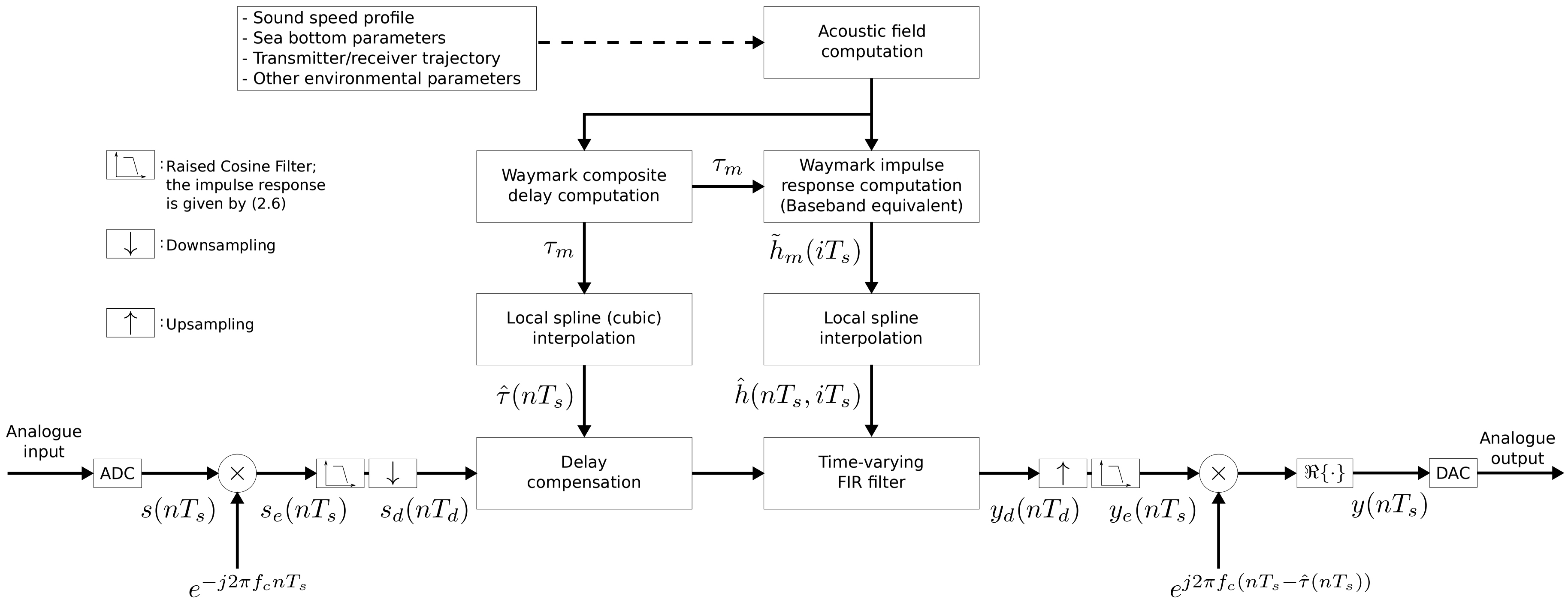

Figure 2.1: A block diagram of the UWA simulator as a development on the system presented in [1]. The link between the delay compensation for the impulse response and taking account for this in the upshifting can be seen represented with $\hat{\tau}(nT_s)$.

described in [1], the common propagation delay is removed from all of the arrivals thus reducing the size of the required impulse response. The frequency response $H_m(f_k)$ at waymark m is computed using an acoustic field computation program, *Bellhop* in this case [67]. The acoustic field is defined by a set of environmental parameters such as sound speed profile, the sea bottom parameters, the transmitter/receiver trajectory, and other environmental parameters. The bandwidth for the channel representation (frequencies f_k) should be selected with reference to the bandwidth of the signal plus any Doppler shift from the environment and movement.

The channel impulse response for each waymark is calculated from the inverse discrete Fourier transform (DFT) of the waymark frequency response. With the waymark composite delay computation, a signal is filtered by the impulse response and an extra delay τ_m. With the delay compensation this gives a set of responses with an alignment based on the cross-correlation of the waymark impulse responses giving a better interpolation between the waymarks. However, the variation of the channel impulse response from one signal sample to another can often be considered slow. Therefore, the computation of the impulse response for every signal sample will be redundant, and the trajectory sampling interval can be made much higher than the signal sampling interval. Then, a local spline interpolation procedure is used for recovering the time-varying impulse response for all signal sampling instants [1]. Cubic splines are used here which provides good trade off between the complexity and accuracy of approximation compared to other spline orders [76].

Due to the low speed of sound, a small deviation of the transmitter/receiver position may result in significant deviation of the multipath propagation delays. With a high sampling interval, this condition can result in significant interpolation errors [77]. To overcome this problem, the delay shifts between consecutive waymark impulse responses are compensated.

Once passed through the channel the signal may be upsampled and upshifted back to the original sampling frequency and passband. Due to the relatively low speed of sound the delays are important in the restoration of the signal to the passband, therefore, the upshift of the signal needs to take into account the delay that is applied to the input signal at each sample point. The upshifted post channel signal may be calculated as follows.

$$y(nT_s) = \Re\{y_e(nT_s)e^{j2\pi f_c(nT_s-\tau_n)}\}, \tag{2.7}$$

where $y(nT_s)$ is the output signal, $y_e(nT_s)$ is the low frequency equivalent signal, τ_n is the estimated additional delay at each output sample instant, and $\Re\{\cdot\}$ denotes the real part of a complex number.

2.3 Shallow Water Experiments

In order to compare the *Waymark* and *VirTEX* models, three experiments are performed. The first is with a flat sound speed profile (SSP), the second is in a summer environment, the third is in a winter environment.

In the three simulations, a pseudo-random binary sequence (PRBS) data signal is passed through the channel models, and a cross-ambiguity function (CAF) [78] is computed. In order to obtain a fine resolution for Doppler and delay in the CAF, a PRBS is generated using an m-sequence of a length of 255 [79]. Five periods of the PRBS are generated at a bit rate of 1250 Hz. A square root raised cosine filter is used for pulse shaping [80] the sequence, with a roll-off factor of 0.25, thus producing a signal with the bandwidth 1562.5 Hz. The carrier frequency is 5 kHz and the sampling frequency is 40 kHz. The transmitted signal duration is 100 s.

2.3.1 Flat sound speed profile

In this simulation, the environment is as follows.

- Flat SSP at 1.5 km/s;
- Flat bottom at 200 m. Sound speed in sea bed 1.6 km/s;
- Flat calm surface;
- Transmitter and Receiver depth 100 m;
- Range $1000 + v_c t$ metres, ($v_c = 5$ m/s);

- Decimation factor 8, giving $T_d = 0.2$ ms.

The decimation factor is 8, giving a large saving in the channel impulse response interpolation and convolution calculations (at least linear in the decimation factor) compared to the original *Waymark* model in [1].

The waymark interval is 0.0512 s. For the *Waymark* model, two minutes of transmission time is simulated requiring 2344 field calculations, this number being proportional to the duration of the transmission time. As for the *VirTEX* model, to cover the whole area for ranges between 0 and 2 km and depths between 0 and 200 m with a resolution of 0.254 m, the same as that in the *Waymark* model, the *VirTEX* model would require 6.2×10^6 field computations; however this figure is constant for any transmission time.

An estimate of the differential delay and Doppler shift between the generated PRBS signal and the demodulated sequences in the receiver a CAF was calculated using:

$$A(\tau, f) = \int_0^T s_1(t) s_2(t + \tau) e^{-j2\pi f t} dt, \tag{2.8}$$

where $s_1(t)$ is the complex envelop of the generated PRBS, $s_2(t)$ is the complex envelop of the demodulated signal from the channel, τ is the multipath arrival delay, and f is the Doppler shift. Figures 2.2(a) and 2.2(b) show the CAF of the generated PRBS and demodulated sequence from the *Waymark* and *VirTEX* channel models.

One period of the signal is chosen for analysis. The images in Figures 2.2(a) and 2.2(b) show some similarities: both have three main paths (direct, and reflected paths from the surface and bottom) showing comparable excess delays. Also, both have similar Doppler shifts (around 16.67 Hz). The variation is considered to be due to the differences in the interpolation in the two models and a different processing window from the removal of the initial propagation delay for all paths.

2.3.2 Summer environment

In this simulation, the environment is as follows.

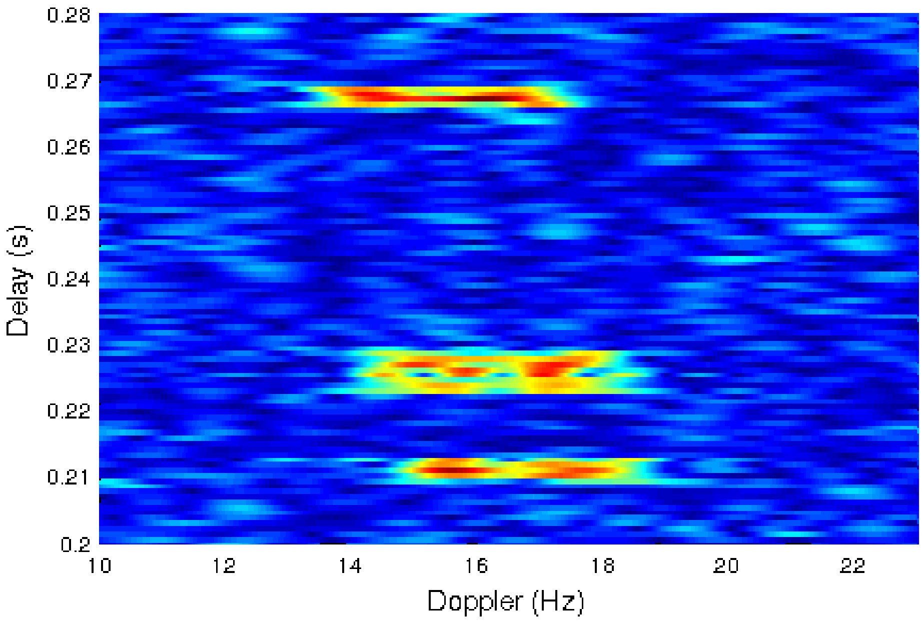

(a) Waymark.

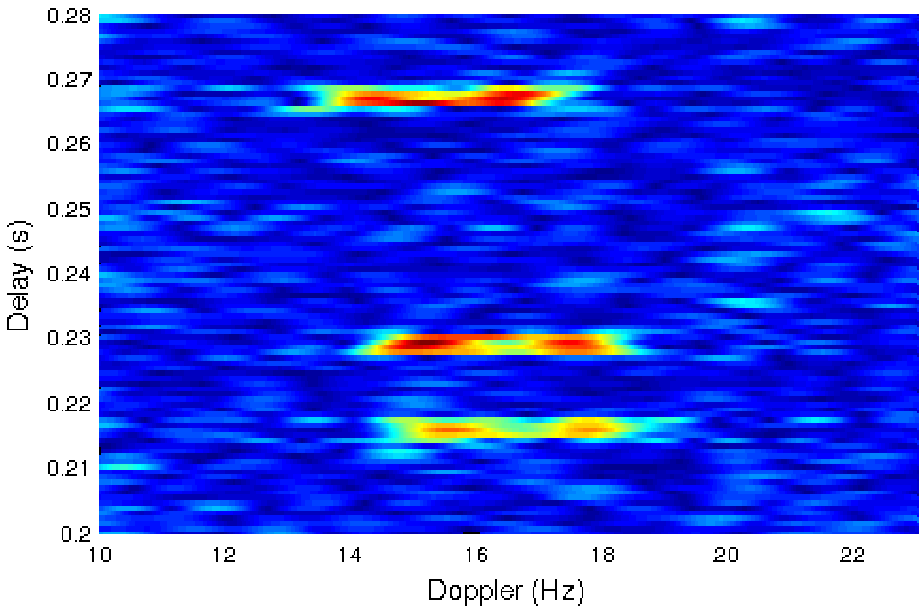

(b) VirTEX.

Figure 2.2: CAF for the two propagation models with a flat SSP.

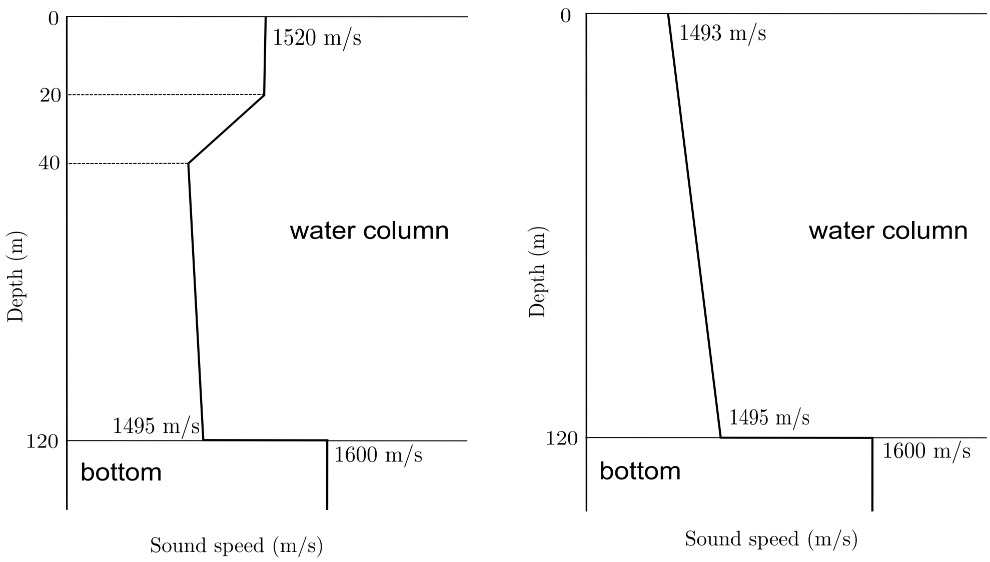

(a) Summer profile

(b) Winter profile

Figure 2.3: The canonical shallow water SSPs [2, 3] used in the simulation.

- The SSP in the summer environment is shown in Figure 2.3(a);
- Flat bottom at 120 m. Sound speed in sea bed 1.6 km/s;
- Flat calm surface;
- Transmitter and Receiver depth 60 m;
- Range $1000 + v_c t$ metres, ($v_c = 5$ m/s);
- Decimation factor 8, giving $T_d = 0.2$ ms.

Figures 2.4(a) and Figure 2.4(b) show the CAF of the generated PRBS and demodulated sequence from the *Waymark* and *VirTEX* channel models, respectively.

One period of the signal is chosen for analysis. The images in Figures 2.2(a) and Figure 2.2(b) show some similarities: both have four main paths (direct, and reflected paths from the surface and bottom) showing comparable excess delays. Also, both have similar Doppler shifts (around 16.67 Hz).

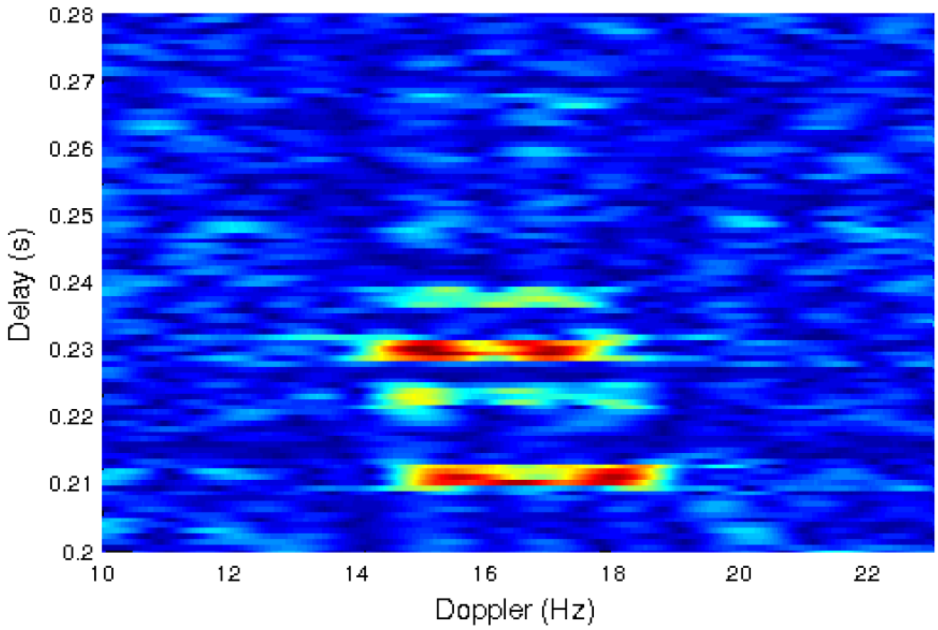

(a) Waymark.

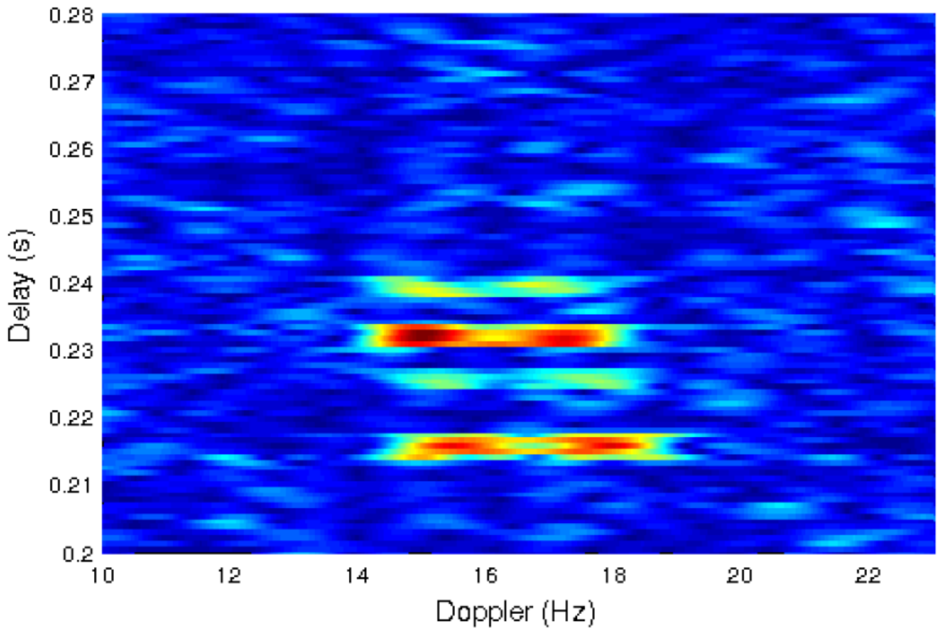

(b) VirTEX.

Figure 2.4: CAF for the two propagation models in the summer environment.

2.3.3 Winter environment

In this simulation, the environment is the same as that described in Section 2.3.2, apart from the winter SSP shown in Figure 2.3(b).

Figures 2.5(a) and Figure 2.5(b) show the CAF of the generated PRBS and demodulated sequence from the *Waymark* and *VirTEX* channel models, respectively.

One period of the signal is chosen for analysis. The images in Figures 2.2(a) and Figure 2.2(b) show some similarities: both have four main paths (direct, and reflected paths from the surface and bottom) showing comparable excess delays. Also, both have similar Doppler shifts (around 16.67 Hz).

The three experiments are conducted with a flat surface to give a clear comparison with *VirTEX*, however a surface model implementation similar to *VirTEX* has been incorporated into the *Waymark* model and simulations will be shown in Chapter 5.

2.4 Summary

In this chapter, the proposed *Waymark* baseband UWA propagation channel model requires a lower computational complexity than the *Waymark* passband UWA propagation channel model [1], and the performance of it is comparable to that of a relatively mature UWA propagation channel model (*VirTEX*) [16]. This chapter involves developing the channel model and signal representation at the baseband. This however represents a significant challenge; the time-varying phase shift introduced into the upshifted signal at the channel output, should be perfectly synchronized with the time-varying delay introduced in the transmitted signal before the baseband time-varying convolution. This is in addition to the decimation process being taken into account. This challenge is similar to that in the baseband Doppler effect compensation in underwater acoustic modems. In this work, three experiments were considered, in which the *Waymark* and *VirTEX* models were compared. The results show similarity with a qualitative comparison, with the major feature such as the Doppler shifts and delays being the same. It is not expected that the results show perfect agreement, since different interpolation procedures are used in the models.

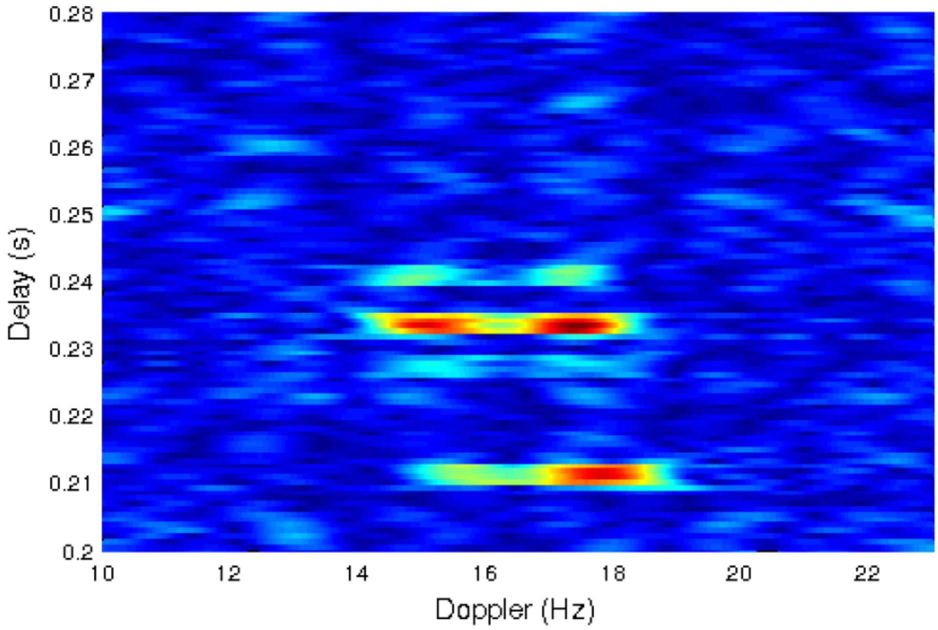

(a) Waymark.

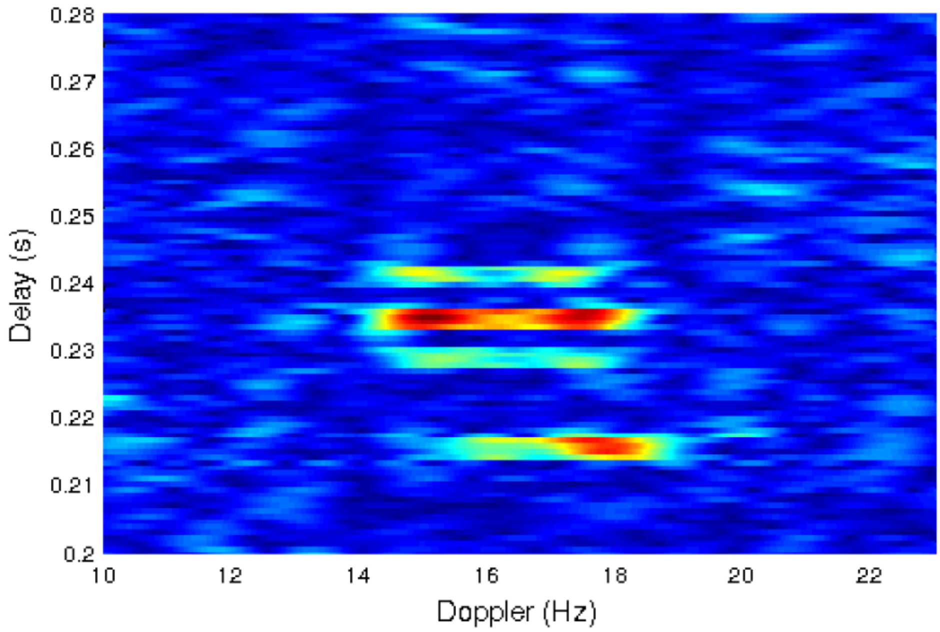

(b) VirTEX.

Figure 2.5: CAF for the two propagation models in the winter environment.

One of significant problems of testing signal processing algorithms for UWA communications is the modelling of the signal transmission, taking into consideration the specific time-varying multipath propagation due to the complicated motion of a receiver and transmitter. For such a virtual signal transmission, we use the developed *Waymark* model to test the Doppler estimation methods in communication sessions with complicated motion of the transmitter and receiver in Chapter 3, and to test the beamforming algorithms with multiple receive antennas in Chapter 5.

Chapter 3

Multi-channel Autocorrelation Method for Doppler Estimation in Fast-varying UWA Channels

Contents

3.1 Introduction

In UWA communications, due to the low propagation speed of acoustic waves, the Doppler effect introduces significant distortions in propagated signals [17, 18, 26, 81]. To achieve a high detection performance accurate Doppler estimation and compensation techniques are required [25, 26, 29, 82]. The Doppler effect is caused by transmitter/receiver motion, by surface waves, by fluctuations of the sound speed, and other phenomena [1, 36, 83]. The Doppler effect on signals is often described as time compression/diletion with a compression factor constant over a measurement interval, i.e., a constant-speed movement [84–87]. For specific underwater tasks, such as underwater imaging, environment monitoring, and sea bottom searching, fast-moving platforms such as autonomous underwater vehicles (AUVs) can use complicated trajectories [88–93], where the constant-speed assumption is not valid. Such movements require frequent re-estimation of the Doppler effect to support a high detection performance of UWA communications [94]. The Doppler estimation then becomes a complicated task dominating the complexity of the receiver [4].

Many Doppler estimation methods are currently used in UWA communications. One such method involves transmitting Doppler-insensitive preamble and postamble around a data package and estimation of the time difference between their arrivals, transformed into the time-compression factor [26, 95, 96]. This method however assumes that the time compression (the transmitter/receiver velocity) is constant over the data package, which is often not the case with a fast-moving and manoeuvring transmitter/receiver. With fast-varying movements, the Doppler estimation should also be performed within the data package, sometimes requiring updates with every received data symbol [94]. Such Doppler estimation techniques have been specifically developed for different single-carrier modulation schemes [24,25,27,28]. These techniques however cannot be directly applied to multicarrier transmission, such as the orthogonal frequency-division multiplexing (OFDM); besides, multicarrier schemes are more sensitive to Doppler distortions and require more accurate Doppler estimation [97].

One efficient method of Doppler estimation in multipath channels is based on computing the cross-ambiguity function (CAF) between received and transmitted signals [60, 61, 97]. The CAF is computed on a two-dimensional (2D) grid of channel delays and Doppler compression factors. The position of maximum of the CAF magnitude over the Doppler grid provides an estimate of the Doppler compression. However, due to a large number of Doppler estimation channels, the CAF method is computationally intensive, even if fast Fourier transforms and a two-step (coarse and fine estimation) approach is used to reduce the number of Doppler channels and speed up the computations [4, 29, 84]. Significantly less complicated is the single-channel autocorrelation (SCA) method [84, 98–101]. This method is applied to periodic transmitted signals and it exploits the fact that, with a moving transmitter/receiver, the signal period changes; the SCA method measures this change to estimate the time-compression factor. Apart from being of low complexity due to a single estimation channel, another benefit of this method is the efficient combining of multipath components. However, the method can fail in cases where the motion of transmitter/receiver involves accelerations.

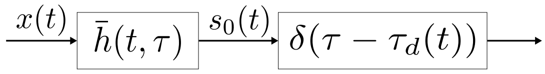

Figure 3.1: Channel model.

In this chapter, we propose a multi-channel autocorrelation (MCA) method that is capable of estimating the Doppler effect in UWA channels with fast moving and manoeuvring transmitter/receiver, having significantly lower complexity than the CAF method and outperforming the SCA method.

The Doppler estimation methods are implemented in a communication system with the transmission of guard-free OFDM and superimposed data and pilot signals [1,31,60,61]. The comparison of the three methods (CAF, SCA and MCA) in a number of simulation scenarios, as well as in two real sea trials, shows that the MCA method outperforms the SCA method, also its performance is comparable to that of the CAF method, but with a less complexity.

3.2 Channel Model

The UWA channel is often modelled as a time-variant linear system with an impulse response $h(t,\tau)$ that describes multipath and Doppler spreads in the channel. The received signal is then given by

$$r(t) = \int_{-\infty}^{\infty} h(t,\tau)s(t-\tau)d\tau + \nu(t), \tag{3.1}$$

where $\nu(t)$ is the additive noise.

In UWA communications, when the transmitter and/or the receiver is moving, the channel can be represented using two time-varying components described by a dominant time-varying channel delay $\tau_d(t)$ and a slower time-varying channel impulse response $\bar{h}(t,\tau)$ as shown in Figure 3.1 [4]. The component $\delta(\tau - \tau_d(t))$ can be thought of as caused by the varying distance between the transmitter and receiver. The component $\bar{h}(t,\tau)$ incorporates variations in the lengths of acoustic rays due to the movement. Thus, the time-varying channel impulse response $h(t,\tau)$ can be represented as a convolution of $\delta(\tau - \tau_d(t))$ and $\bar{h}(t,\tau)$.

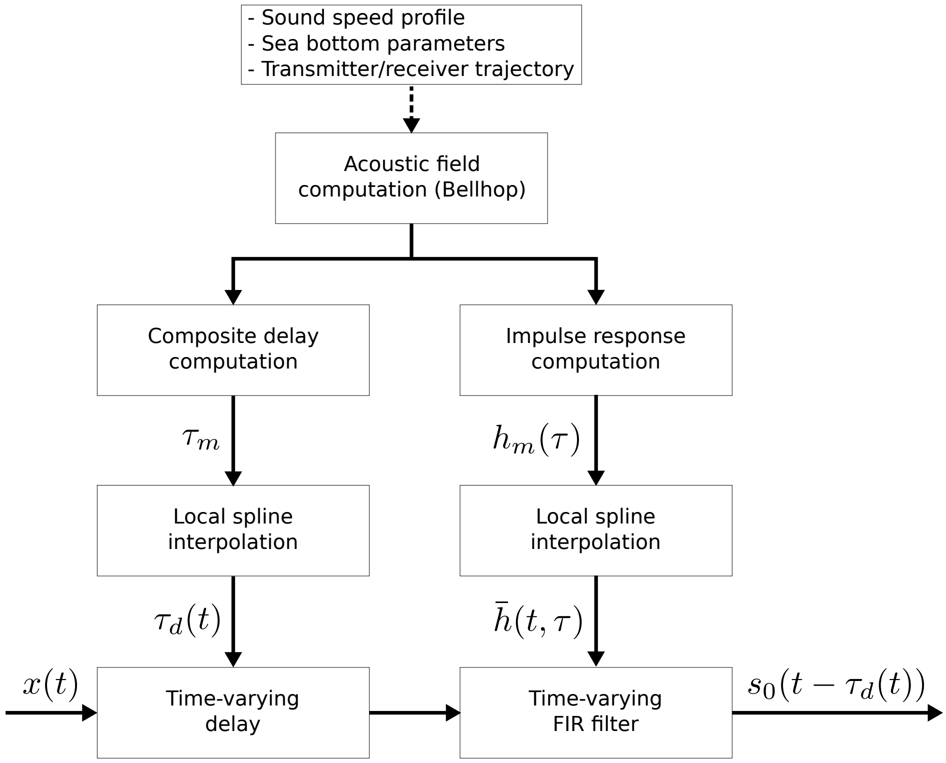

Figure 3.2: A block diagram of the *Waymark* underwater acoustic simulator; adapted to this chapter.

The *Waymark* channel simulator [1] shown in Figure 3.2 implements the channel model in Figure 3.1 using the acoustic field computation for an environment defined by a sound speed profile (SSP) and acoustic bottom parameters. This is done using the Bellhop ray/beam tracing [67]. Using the ray parameters, the *Waymark* simulator computes the dominant delays $\{\tau_m\}$ and channel impulse responses $\{h_m(\tau)\}$ for a set of points (waymarks) along the transmitter/receiver trajectory. These are interpolated in time to obtain the continuous time-varying delay $\tau_d(t)$ and impulse response $\bar{h}(t,\tau)$; in the simulator, the continuous time t is treated as the discrete time at a sampling rate high enough to accurately represent the communication signal. The (fractional) delay $\tau_d(t)$ is then implemented by interpolation of the signals, whereas the convolution with the impulse response $\bar{h}(t,\tau)$ is implemented using a time-varying FIR filter. In this chapter, the *Waymark* simulator is used for numerical investigation of the Doppler estimation methods in a number of scenarios. Note that sea trials with such scenarios would otherwise be difficult to conduct. However, data from sea trials are also used for investigation of the Doppler estimators.

3.3 Multi-channel Autocorrelation Doppler Estimator

Consider the channel model in Figure 3.1. Let the transmitted signal $x(t)$ be represented using an equivalent baseband signal $\widetilde{x}(t)$:

$$\begin{aligned} x(t) &= \Re\{\widetilde{x}(t)e^{j\omega_c t}\} \\ &= \frac{1}{2}\widetilde{x}(t)e^{j\omega_c t} + \frac{1}{2}\widetilde{x}^*(t)e^{-j\omega_c t}, \end{aligned} \tag{3.2}$$

where $\Re\{\cdot\}$ denotes the real part of a complex-valued number. Similarly, we have

$$\begin{aligned} s_0(t) &= \Re\{\widetilde{s}_0(t)e^{j\omega_c t}\} \\ &= \frac{1}{2}\widetilde{s}_0(t)e^{j\omega_c t} + \frac{1}{2}\widetilde{s}_0^*(t)e^{-j\omega_c t}, \end{aligned} \tag{3.3}$$

where $\widetilde{s}_0(t)$ is an equivalent baseband signal for $s_0(t)$.

Let the signal $\widetilde{x}(t)$ be periodic with a period T_s, so that

$$\widetilde{x}(t + T_s) = \widetilde{x}(t). \tag{3.4}$$

Assume that the first component in the channel model, shown in Figure 3.1, is time-invariant, i.e., $\bar{h}(t, \tau) = \bar{h}(\tau)$. Then, the baseband signal $\widetilde{s}_0(t)$ is also periodic with the same period T_s, i.e.,

$$\widetilde{s}_0(t + T_s) = \widetilde{s}_0(t). \tag{3.5}$$

The second channel component in Figure 3.1 is modelled as a time-varying delay $\tau_d(t)$, so the output of the channel without noise is given by

$$\begin{aligned} s(t) =& s_0(t - \tau_d(t)) \\ =& \frac{1}{2}\widetilde{s}_0(t - \tau_d(t))e^{j\omega_c(t-\tau_d(t))} + \frac{1}{2}\widetilde{s}_0^*(t - \tau_d(t))e^{-j\omega_c(t-\tau_d(t))}. \end{aligned} \tag{3.6}$$

In a receiver, typical front-end processing includes a frequency shifting of the received signal $s(t)$ by ω_c via multiplying the signal by $e^{-j\omega_c t}$ and further low-pass filtering. Therefore, the second component in (3.6) is filtered out, and the front-end processing produces a baseband signal

$$\widetilde{s}(t) = \widetilde{s}_0(t - \tau_d(t))e^{-j\omega_c \tau_d(t)}. \tag{3.7}$$

3.3.1 Single-channel autocorrelation estimator

The delay $\tau_d(t)$ can often be represented as a linear function of time, described by two parameters, an initial delay a_0 and a time-compression factor a_1 [17, 81]:

$$\tau_d(t) = a_0 + a_1 t, \quad t \in [-\Theta/2, \Theta/2], \tag{3.8}$$

where Θ is a measurement interval. For estimation of the parameter a_1, the autocorrelation function

$$\rho(\tau) = \int_{-\Theta/2}^{\Theta/2} \widetilde{s}^*(t)\widetilde{s}(t+\tau)dt \tag{3.9}$$

of the baseband signal $\widetilde{s}(t)$ can then be used [102]. More specifically, a_1 can be estimated by searching for the maximum of $|\rho(\tau)|$ over delays in vicinity of the signal period T_s:

$$\tau_{\max} = \arg \max_{T_s - \tau_M \le \tau \le T_s + \tau_M} |\rho(\tau)|, \tag{3.10}$$

where $[\tau - \tau_M, \tau + \tau_M]$ is a search interval defined by the maximum possible delay τ_M due to the time compression, i.e., due to the maximum relative speed between the transmitter and receiver. The ratio $\hat{a}_1 = 1 - T_s/\tau_{\max}$ can be considered as an estimate of a_1 (see below). We call such an estimator of a_1 the SCA estimator.

3.3.2 Multi-channel autocorrelation estimator

However, the SCA estimator is limited in accuracy when the Doppler compression factor varies over the measurement interval, i.e., when the delay line in Figure 3.1 is described by a polynomial of a higher degree, e.g., if $\tau_d(t)$ is a quadratic polynomial:

$$\tau_d(t) = a_0 + a_1 t + a_2 t^2, \quad t \in [-\Theta/2, \Theta/2], \tag{3.11}$$

where a_2 is a parameter describing the acceleration. Let a be an uniform acceleration between the transmitter and receiver. Due to this acceleration, the distance $d(t)$ between the transmitter and receiver varies in time as $d(t) = at^2/2$ in a straight line. Since $\tau_d(t) = d(t)/c$, we have $a_2 = a/(2c)$, where c is the sound speed.

In fast-varying channels, for estimation of Doppler parameters, we propose to use the following statistic:

$$\rho(\tau, \omega, \mu) = \int_{-\Theta/2}^{\Theta/2} \widetilde{s}^*(t)\widetilde{s}(\mu t + \tau)e^{j\omega t}dt. \tag{3.12}$$

Specifically, the position of the peak of $|\rho(\tau, \omega, \mu)|$ over delay τ in vicinity of the signal period T_s and over the angular frequency $\omega = 2\pi f$ and compression factor μ:

$$\{\tau_{\max}, \omega_{\max}, \mu_{\max}\} = \arg\max_{\tau,\omega,\mu} |\rho(\tau, \omega, \mu)|, \tag{3.13}$$

will define the Doppler estimate as explained below.

We now show how the position of the maximum of $|\rho(\tau, \omega, \mu)|$ relates to the Doppler parameters a_1 and a_2 in (3.11). Denote the product in the integral (3.12) as

$$z(t) = \widetilde{s}^*(t)\widetilde{s}(\mu t + \tau)e^{j\omega t}. \tag{3.14}$$

Using (3.7), we obtain that

$$z(t) \quad = \quad \widetilde{s}_0^*[t - \tau_d(t)]\widetilde{s}_0[(\mu t + \tau) - \tau_d(\mu t + \tau)]e^{j\omega_c[\tau_d(t) - \tau_d(\mu t + \tau)] + j\omega t}. \tag{3.15}$$

In order to achieve a maximum of $|\rho(\tau, \omega, \mu)|$, according to the Cauchy-Bunyakovsky-Schwarz inequality [103], the following should be satisfied

$$\widetilde{s}_0[t - \tau_d(t)]e^{-j\omega_c[\tau_d(t) - \tau_d(\mu t + \tau)] - j\omega t} = \beta\widetilde{s}_0[(\mu t + \tau) - \tau_d(\mu t + \tau)], \tag{3.16}$$

where β is an arbitrary constant independent of time. To satisfy this equality, we need, in particular, to guarantee that the exponent in (3.16) is independent of time t. With the approximation of the channel delay $\tau_d(t)$ as in (3.11), the component $\tau_d(t) - \tau_d(\mu t + \tau)$ in the exponent can be represented as

$$\tau_d(t) - \tau_d(\mu t + \tau) \quad = \quad -(a_1\tau + a_2\tau^2) \tag{3.17}$$

$$+ \quad (a_1 - a_1\mu - 2a_2\mu\tau)t \tag{3.18}$$

$$+ \quad a_2(1 - \mu^2)t^2. \tag{3.19}$$

The first (time-independent) term (3.17) is absorbed in the constant β, and therefore it can be ignored. Below, we will show that the third term (3.19) can also be ignored. In order to make the second term (3.18) equal zero for any t, the following should be satisfied:

$$\omega_c(a_1 - a_1\mu - 2a_2\mu\tau) + \omega = 0. \tag{3.20}$$

From this relationship, we arrive at the following estimate of the parameter a_2:

$$\hat{a}_2 = \frac{\omega_{\max} + a_1(1-\mu_{\max})\omega_c}{2\mu_{\max}\tau_{\max}\omega_c}, \tag{3.21}$$

where instead of a_1 its estimate can be substituted. Note that in many scenarios $\mu_{\max} \approx 1$ and therefore, the estimate in (3.21) can be simplified as

$$\hat{a}_2 = \frac{\omega_{\max}}{2\tau_{\max}\omega_c}. \tag{3.22}$$

To guarantee (3.16), we also need to equate arguments of $\widetilde{s}_0(\cdot)$ in both sides of this equation. Thus, we arrive at the relationship

$$t - \tau_d(t) = (\mu t + \tau) - \tau_d(\mu t + \tau) - T_s, \tag{3.23}$$

where we also take into account that the signal $\widetilde{s}_0(t)$ is periodic with the period T_s. Using (3.11), this condition takes the form

$$\begin{aligned} & (-a_1\tau - a_2\tau^2 + \tau - T_s) && (3.24)\\ + \quad & (a_1 - a_1\mu - 2a_2\mu\tau + \mu - 1)t && (3.25)\\ + \quad & a_2(1-\mu^2)t^2 = 0. && (3.26) \end{aligned}$$

Due to the time dependence present in this equation, we have to make all the three terms equal zero. Note that the last term (3.26) can be shown to be close to zero for all $t \in [-\Theta/2, \Theta/2]$ (see below), and therefore it can be ignored.

Making the first term (3.24) equal zero results in the following relationship:

$$\begin{aligned} \tau_{\max} &= \frac{1}{2a_2}\left(k - \sqrt{k^2 - 4a_2 T_s}\right) \\ &\simeq \frac{T_s}{k}\left(1 + \frac{a_2 T_s}{k^2}\right), \end{aligned} \tag{3.27}$$

where $k = 1 - a_1$. This approximation is based on the facts that $k \simeq 1$, $a_2 T_s \ll 1$ (see below), and the approximation $\sqrt{1-\varepsilon} \approx 1 - \varepsilon/2 - \varepsilon^2/8$, applicable if $|\varepsilon| \ll 1$. If $a_2 = 0$, we arrive at the estimate of the parameter a_1 given by

$$\hat{a}_1 = 1 - \frac{T_s}{\tau_{\max}}, \tag{3.28}$$

which is exploited in the SCA estimator. For $a_2 \neq 0$, from (3.27), after some algebra, we arrive at the following estimate of a_1:

$$\hat{a}_1 = 1 - \frac{T_s}{\tau_{\max}} - \alpha\frac{\omega_{\max}}{2\omega_c}, \tag{3.29}$$

where $\alpha = [T_s/(k\tau_{\max})]^2 \simeq 1$.

Making the second term (3.25) equal zero results in the following relationship:

$$\mu_{\max} = \frac{1}{1 - \frac{2a_2\tau_{\max}}{k}}, \tag{3.30}$$

where instead of a_2 its estimate from (3.22) can be used. Note that $\mu_{\max}$ has a weak dependence on a_1, since $k = 1 - a_1 \approx 1$, and therefore we can approximately write:

$$\mu_{\max} \approx \frac{1}{1 - \omega_{\max}/\omega_c}. \tag{3.31}$$

Thus, $\mu_{\max}$ can be found from $\omega_{\max}$. This simplifies the Doppler estimation. According to (3.13), the statistic $|\rho(\tau, \omega, \mu)|$ needs to be computed at a three-dimensional (3D) grid. However, as $\mu_{\max}$ and $\omega_{\max}$ are inter-dependent, only a 2D grid over (τ, ω) is sufficient.

Previously, the term $a_2(1-\mu^2)t^2$ has been ignored for $t \in [-\Theta/2, \Theta/2]$ in (3.19) and (3.26); we now justify this step in our derivation. In many applications, it can be assumed that $a < 1$ m/s^2 [94, 97, 101]. Assuming also that Δ is the time-correlation interval of the signal

$\widetilde{s}_0(t)$, which is given by $\Delta \approx 1/F$, the term $a_2 t^2(1-\mu^2)$ can be ignored if

$$|a_2 t^2(1-\mu_{\max}^2)| \ll \Delta \approx \frac{1}{F}. \tag{3.32}$$

From (3.30), taking into account that, for $|\varepsilon| \ll 1$, $(1-\varepsilon)^{-2} \simeq 1+2\varepsilon$ and $\tau_{\max} \simeq T_s/k$, we approximately have

$$1-\mu_{\max}^2 \cong -\frac{4a_2 T_s}{k^2}. \tag{3.33}$$

Therefore, it is sufficient to require that

$$\frac{a^2\Theta^2 T_s F}{4c^2} \ll 1. \tag{3.34}$$

In our experimental scenarios, we have $\Theta = 1$ s, $T_s = 1$ s, $F = 1024$ Hz, $c = 1.5$ km/s, and $a < 1$ m/s^2. For all these scenarios, $a^2\Theta^2 T_s F/(4c^2) < 10^{-4} \ll 1$; thus, this requirement is satisfied with a significant margin.

When deriving (3.29), it was assumed that $a_2 T_s \ll 1$. Indeed, in our scenarios, $a_2 T_s = aT_s/(2c) \approx 1/3000 \ll 1$, i.e., the assumption is satisfied with a significant margin.

We now analyse a possibility of setting $\mu = 1$ in (3.13) to further simplify the Doppler estimator. Such setting is possible if

$$|\Theta - \Theta\mu_{\max}| \ll \Delta \approx \frac{1}{F}, \tag{3.35}$$

or $\Theta F|1-\mu_{\max}| \ll 1$, i.e., if the signal compression due to the factor $\mu_{\max}$ over the observation interval Θ does not exceed the signal autocorrelation interval Δ. For our scenarios, from (3.30) we obtain

$$\Theta F|1-\mu_{\max}| < 0.3 \ll 1, \tag{3.36}$$

i.e., this requirement is satisfied and we can set $\mu = 1$. Indeed, with higher values of the measurement interval Θ and the frequency bandwidth F, one of the components in (3.13) needs to be prescaled with a compression factor μ related to the frequency ω as $\mu = (1-\omega/\omega_c)^{-1}$.

The estimates of parameters a_1 and a_2, obtained in the MCA Doppler estimator, are used for approximation of the delay $\tau_d(t)$ and resampling the received signal (see Figure 3.4).

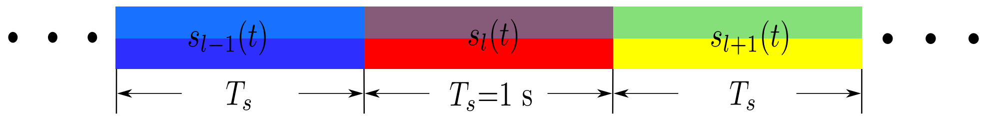

Figure 3.3: Guard-free OFDM symbols.

Note that in the SCA method, the term $\frac{\omega_{max}}{2\omega_c}$ as in (3.29) is ignored, which makes the SCA method less accurate when there is a non-zero acceleration a. However, the main disadvantage of the SCA method against the MCA method is that, with non-zero acceleration, the amplitude of the autocorrelation peak in the vicinity of the signal period T_s is reduced. For example, for pseudo-noise signals, such as the m-sequence [104], with a δ-like ambiguity function, the amplitude at $\omega = 0$ will be close to zero if $\omega_{\max}\Theta > 2\pi$; e.g., for our scenarios, it corresponds to accelerations $a > 0.5$ m/s^2.

3.4 Transmitted Signal and Receiver

In this section, the transmitted signal and the receiver structure are described.

3.4.1 Transmitted signal

OFDM symbols without any guard interval, such as a cyclic prefix or zero padding, are considered. The duration of the transmitted OFDM symbol is the same as the orthogonality interval, shown in Figure 3.3. The transmitted signal consists of a continuous sequence of guard-free OFDM symbols [4, 60] is given by:

$$s_l(t) = \Re\left\{ e^{j2\pi f_c t} \sum_{k=-N_s/2}^{N_s/2-1} [M_p(k) + jD_l(k)] e^{j\frac{2\pi}{T_s}kt} \right\}, \tag{3.37}$$

where $l = 1, 2, \ldots, L$, L is the number of OFDM symbols in the transmitted data package, $N_s = 1024$ the number of sub-carriers, $f_c = \omega_c/(2\pi) = 3072$ Hz the carrier frequency, $F = 1024$ Hz the frequency bandwidth, $T_s = 1$ s the symbol duration, and $j = \sqrt{-1}$. The sequence $M_p(k) \in [-1, +1]$ is a binary pseudo-random sequence of length N_s, serving as the superimposed pilot signal, the same for all OFDM symbols. Therefore, the pilot signal is periodic in time with the period T_s. The sequence $D_l(k)$ represents the information data in the lth OFDM symbol; it is obtained by interleaving and encoding original data across sub-carriers using rates 1/2 or 1/3 convolutional codes [104].

Note that in the sea trial described in Section 3.6.1 later on, the guard-free OFDM symbols at the carrier frequency $f_c = 768$ Hz with a frequency bandwidth of $F = 256$ Hz were transmitted.

Such a superimposed combining of the information data and pilot does not solve completely the problem of available resources as half of the signal energy is allocated to the pilot, i.e., half of signal energy is wasted. However, in the UWA communication channels, the using of the guard-free OFDM signals with superimposed data and pilot symbols is considered to benefit the spectral efficiency [4, 62], due to the fact that the channel capacity is directly proportional to the available frequency bandwidth, but proportional to the logarithm of the signal energy. Furthermore, compared to the radio communications in the air, the UWA communication is characterised with much lower speed propagation and more complicated multipath, which makes the delay much larger. In this case, the conventional cyclic prefix is unable to act as a buffer region to protect OFDM signals from intersymbol interference.

3.4.2 Receiver

Figure 3.4 shows the block diagram of the receiver. The front-end processing implements the frequency shifting of the received signal $r(t) = s(t) + n(t)$ by ω_c, where $n(t)$ is a noise signal, the low-pass filtering, and analogue-to-digital conversion of the baseband signal

$$\widetilde{r}(t) = \widetilde{s}(t) + \widetilde{n}(t), \tag{3.38}$$

where $\widetilde{n}(t)$ is a baseband noise signal, into signal samples $\widetilde{r}(i)$ taken with a sampling interval $\Delta\tau = T_s/(N_s N_\tau)$, where N_τ is the time oversampling factor, which is set to $N_\tau = 2$ for our experiments.

The Doppler estimation consists of two steps: coarse and fine estimation. The coarse estimation is implemented using one of three methods: CAF; SCA; or MCA. In the CAF method, $2N_d + 1$ Doppler sections of the ambiguity function is computed with a period

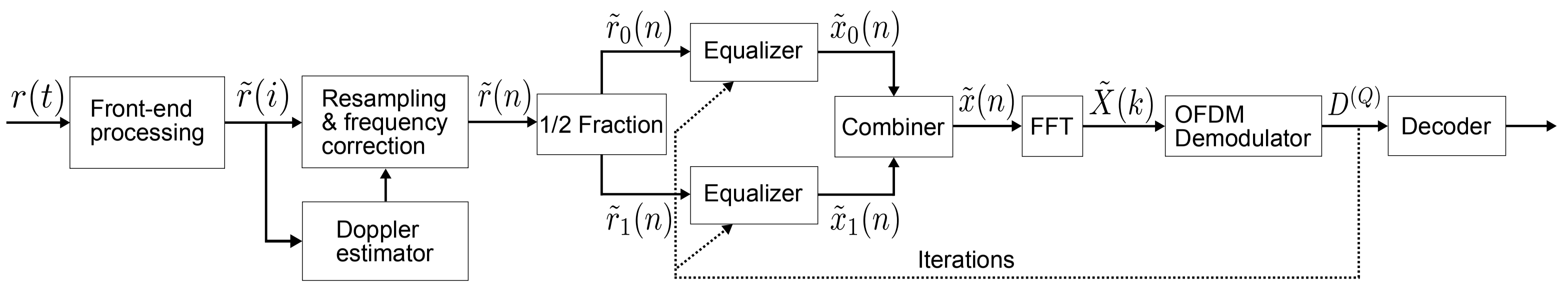

Figure 3.4: Block diagram of the receiver of guard-free OFDM signal.

T_{est} by cross-correlating the scale-distorted received signal and one period of the pilot signal (see [26] and [4] for more details). The ambiguity function is computed on the *delay-Doppler scale* grid. The delay step on the grid is $\Delta\tau$. The Doppler scale step is chosen so that the corresponding frequency shift Δf is a predefined fraction of the subcarrier spacing F/N_s: $\Delta f = F/(N_s N_D)$, with the frequency oversampling factor N_D set to $N_D = 2$. In [4], it is shown that such a coarse resolution is enough for operation of the receiver, whereas higher N_D would proportionally increase the complexity of the Doppler estimator. However, this coarse resolution would not be good enough for equalization and demodulation. Therefore, the coarse estimate is refined by using parabolic interpolation as detailed in [4].

The SCA method is implemented by computing the autocorrelation of the received signal,

$$A_{\text{SCA}}(\tau) = \sum_{i=0}^{N_\tau N_s - 1} \widetilde{r}^*(i)\widetilde{r}\left(i + \frac{\tau}{\Delta\tau}\right), \tag{3.39}$$

where $\tau/\Delta\tau \in \{N_\tau N_s - \tau_M/\Delta\tau, N_\tau N_s + \tau_M/\Delta\tau\}$, and finding the maximum

$$\tau_{\max} = \arg\max_{\tau} |A_{\text{SCA}}(\tau)|. \tag{3.40}$$

The parameter a_1 is then estimated as in (3.28).

The MCA method is implemented by computing $2N_d + 1$ autocorrelation functions with a set of frequency shifts ω_m, $m = -N_d, \ldots, N_d$:

$$A_{\text{MCA}}(\tau, \omega_m) = \sum_{i=0}^{N_\tau N_s - 1} \widetilde{r}^*(i)\widetilde{r}\left(i + \frac{\tau}{\Delta\tau}\right) e^{j\omega_m \Delta\tau i}, \tag{3.41}$$

where $\tau/\Delta\tau \in \{N_\tau N_s - \tau_M/\Delta\tau, N_\tau N_s + \tau_M/\Delta\tau\}$ and $\omega_m = 2\pi\Delta f m$. The parameter a_1 is then estimated as in (3.29), where

$$\{\tau_{\max}, \omega_{\max}\} = \arg\max_{\tau,\omega_m} |A_{\text{MCA}}(\tau, \omega_m)|. \tag{3.42}$$

Note that the complexity of each of the three methods is directly proportional to the number of Doppler estimation channels $(2N_d + 1)$. It can be shown that the complexity of a single channel is approximately the same in all the methods. Therefore, to compare the complexity, we need to know the number of Doppler channels. For the CAF method, N_d is approximately

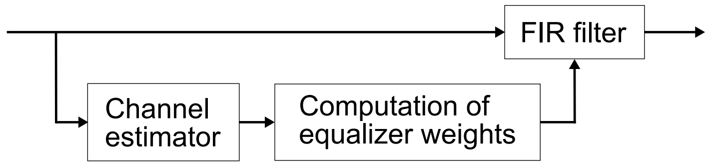

Figure 3.5: Block diagram of a single branch of the equalizer [4].

given by

$$N_d = \text{round}\left[\frac{V_{\max} f_c}{c\Delta f}\right], \tag{3.43}$$

where round[·] denotes the closest integer number, $\Delta f = 0.5$ Hz the Doppler frequency step, $f_c = 3072$ Hz the carrier frequency, $c = 1.5$ km/s the underwater sound speed, and $V_{\max}$ the maximum speed of transmitter/receiver. For the MCA method, N_d is given by

$$N_d = \text{round}\left[\frac{U_{\max} T_s f_c}{c\Delta f}\right], \tag{3.44}$$

where $U_{\max}$ is the maximum acceleration of transmitter/receiver.

The discrete-time estimates of the Doppler scale factor obtained with the time interval T_{est} (in our experiments, $T_{\text{est}} = T_s/4$) are linearly interpolated, and used to compensate for the dominant time-varying Doppler effect by resampling and frequency correcting the signal $\widetilde{r}(i)$ (see [4] for details).

The resampled and frequency corrected signal $\widetilde{r}(n)$ is divided into two fractional diversity signals $\widetilde{r}_0(n)$ and $\widetilde{r}_1(n)$, corresponding to odd and even samples of $\widetilde{r}(n)$, respectively. The two signals are independently time-domain equalized. Figure 3.5 shows the block diagram of a single branch of the equalizer. Assuming perfect compensation of the dominant Doppler compression described by the time-varying delay $\tau_d(t)$, the equalization deals with the distortions of the signal caused by the slow variant impulse response $\bar{h}(t,\tau)$ (see Figure 3.1).

The equalized signals $\widetilde{x}_0(n)$ and $\widetilde{x}_1(n)$ from the two diversity branches are combined to produce one combined signal $\widetilde{x}(n)$. The equalizer is implemented using the channel-estimate-based FIR scheme with a channel estimator based on an RLS adaptive filter [31, 43]. The linear equalizer compensates for scale factors of different multipath components and combines these components. The channel estimates are transformed into spline coefficients for the impulse response of the equalizer FIR filter to trace the time-varying channel fluctuations (see [4, 31] for details).

The combined signal is then converted into a frequency domain signal $\widetilde{X}(k)$. The frequency domain signal is demodulated to produce tentative data estimates D, further refined in Q iterations; in our experiments, $Q = 1$. The final data estimate $D^{(Q)}$ is applied to the Viterbi decoder [104] to recover transmitted data.

3.5 Numerical Results

In this section, we investigate the detection performance of three versions of the receiver of guard-free OFDM signals, shown in Figure 3.4. These versions differ in the Doppler estimator, which are the CAF, SCA, or MCA estimator. The investigation is performed using the *Waymark* simulator [1] to model the time-varying multipath distortions of signals, caused by moving transmitter and/or receiver in specific acoustic environments. The required signal-to-noise ratio (SNR), from 7 dB to 17 dB, is then achieved by adding independent Gaussian noise to the distorted signal. The SNR is defined as the ratio of the energy of the distorted signal over the whole length of the communication session to the noise energy over the same time interval, in the frequency bandwidth of the transmitted signal (from 2560 Hz to 3584 Hz). The SNR is computed in the passband as:

$$SNR = 2E_{pass}/N_0, \tag{3.45}$$

where E_{pass} is the signal energy in the passband, and the N_0 is the noise energy in the passband.

In the simulation, the following three scenarios are considered:

- Scenario 1: the transmitter moves with a sinusoid-like trajectory towards the receiver at a speed of 6 m/s, while the receiver is stationary, as shown in Figure 3.6(a);
- Scenario 2: the transmitter moves with a sinusoid-like trajectory past the receiver at a speed of 6 m/s, while the receiver moves towards the transmitter at a speed of 6 m/s, as shown in Figure 3.6(b);
- Scenario 3: the transmitter performs a slow *flower circle* movement, while the receiver

moves towards the transmitter at a speed of 6 m/s, as shown in Figure 3.6(c).

The depth of both the transmitter and the receiver is 60 m. The data transmission lasts for 200 s, i.e., $L = 200$ OFDM symbols are continuously transmitted in a communication session.

3.5.1 Transmitter moves towards receiver

In this scenario, two shallow water environments are considered, with summer and winter SSPs [2, 3], shown in Figure 3.7(a) and Figure 3.7(b), respectively. The transmitter moves towards the receiver with a sinusoid-like trajectory as shown in Figure 3.6(a). Such a movement can be caused when a transducer is towed by a surface vessel. Indeed, the sinusoid-like trajectory is only an approximation of a real movement affected by the surface waves [1]. The distance $\mathrm{D}(t)$ between the transmitter and receiver varies in time as

$$\mathrm{D}(t) = \mathrm{D}_0 - v_t t + K \sin\left(\frac{2\pi t}{T}\right), \tag{3.46}$$

where D_0 is an initial distance at $t = 0$, $K = 2$ m is the sinusoid amplitude, $T = 10$ s is a typical period of surface waves, and $v_t = 6$ m/s is the speed of the vessel. Thus, the maximum speed between the transmitter and receiver is $V_{\max} = 7.3$ m/s and the maximum acceleration $U_{\max} = 0.79$ m/s^2.

Based on the maximum velocity and acceleration, from (3.43) and (3.44) we obtain the number of Doppler channels in the CAF and MCA estimators as 61 and 7, respectively. As the complexity of the estimators is proportional to the number of Doppler channels, it can be seen that the MCA estimator requires almost 9 times less computations. Indeed, the SCA method requires a single estimation channel and it has the lowest complexity of the three methods. However, as will be seen from our investigation, the SCA method is incapable of providing reliable detection.

1. **Experiment with the summer SSP**

   This experiment starts at the distance $D_0 = 10$ km. Figure 3.8(a) shows fluctuations of the channel impulse response. Figure 3.9(a) shows the bit-error-rate (BER) performance of the receiver with the three Doppler estimation methods. It can be seen that the SCA method is unable to provide a reliable detection, whereas the MCA estimator

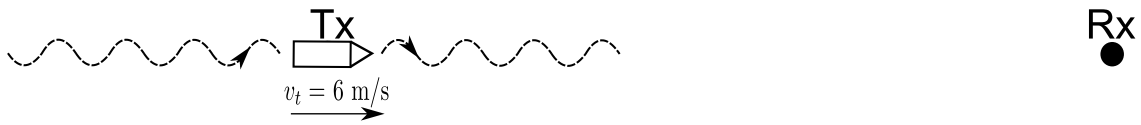

(a) Transmitter moves towards receiver

(b) Transmitter moves past receiver

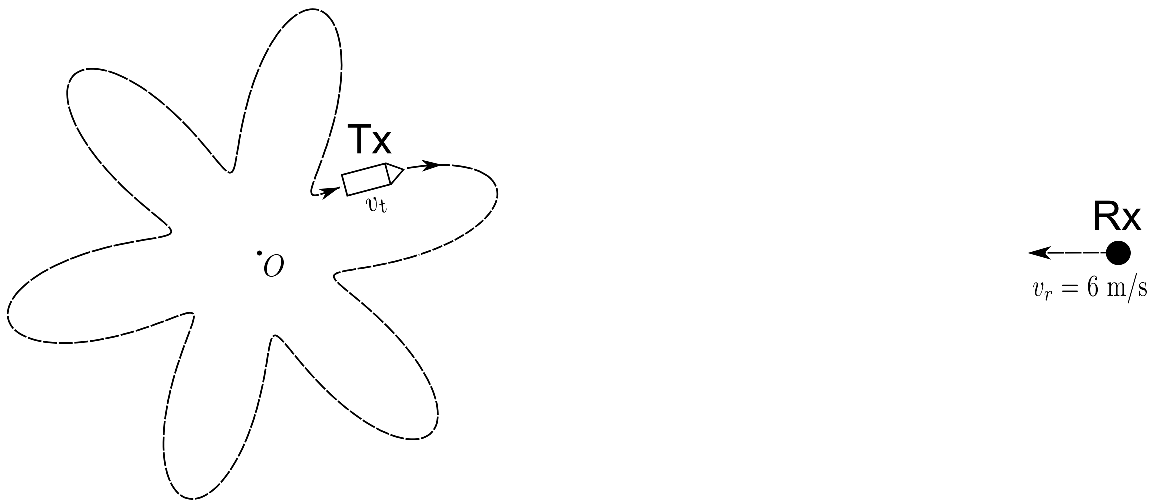

(c) Flower circle movement of the transmitter

Figure 3.6: Simulation scenarios (top view; Tx is the transmitter, and Rx is the receiver).

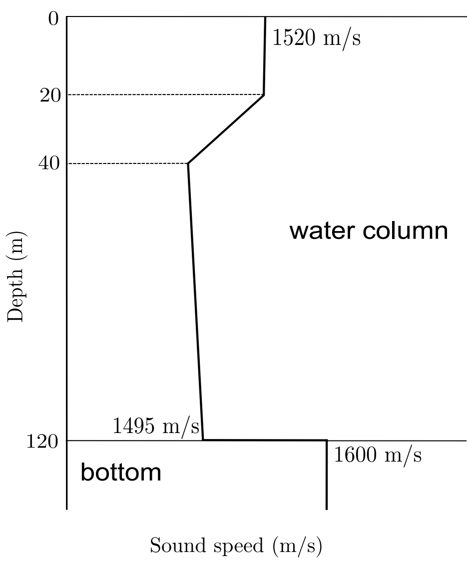

(a) Summer profile

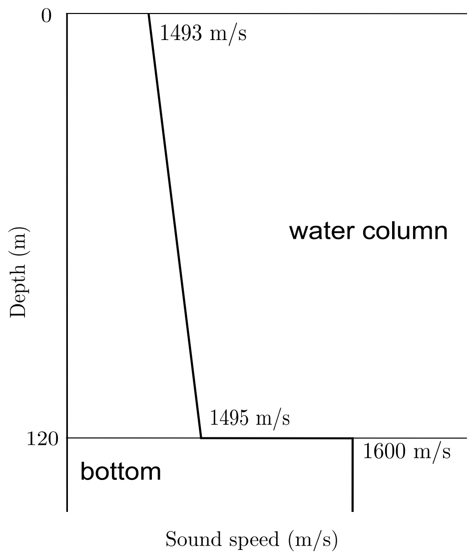

(b) Winter profile

Figure 3.7: The canonical shallow water SSPs [2, 3] used in the simulation; For convenience, Figure 2.3 is shown here again.

provides a BER performance comparable to that of the CAF method.

2. **Experiment with the winter SSP**

In this case, the SSP is as shown in Figure 3.7(b), and the initial distance is set to $\mathrm{D}_0 = 20$ km. Figure 3.8(b) shows fluctuations of the channel impulse response in this case. It is seen that the multipath structure of this channel is more complicated than in the channel with the summer SSP. However, as seen in Figure 3.9(b), the proposed MCA method still provides a performance comparable to that of the CAF method. It is also seen that the SCA method cannot provide reliable detection.

3.5.2 Transmitter moves past receiver

In this scenario, the summer SSP is used for simulation, and the distance $\mathrm{D}(t)$ between the transmitter and receiver is described as

$$\mathrm{D}(t) = \sqrt{(\mathrm{D}_0 - v_r t)^2 + (v_t t + K \sin(2\pi t/T))^2}, \tag{3.47}$$

where $\mathrm{D}_0 = 2$ km is the initial distance at $t = 0$, $K = 2$ m, $T = 10$ s and $v_t = v_r = 6$ m/s. Figure 3.8(c) shows fluctuations of the channel impulse response in this scenario. Figure 3.9(c)

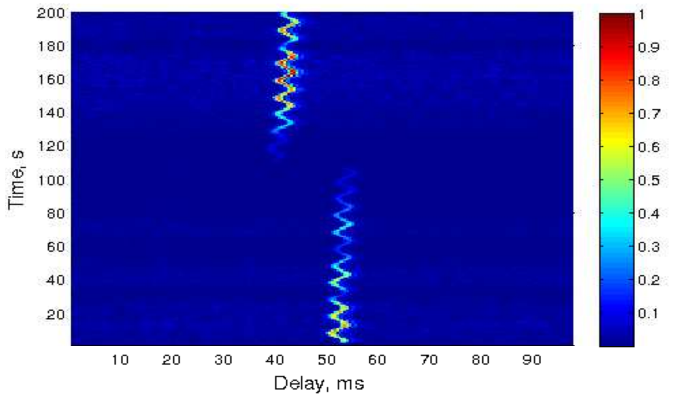

(a) Summer SSP, transmitter moves towards receiver (10 km).

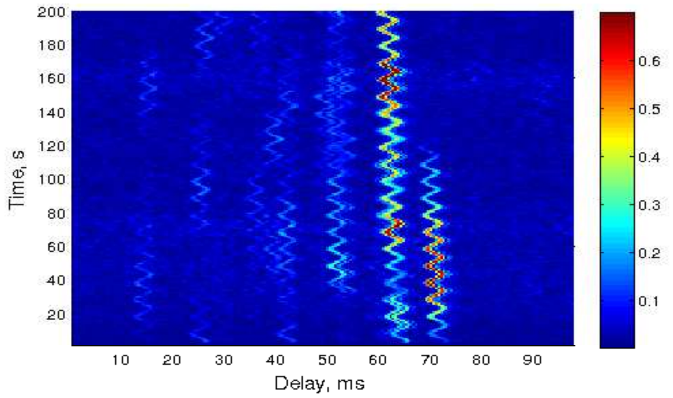

(b) Winter SSP, transmitter moves towards receiver (20 km).

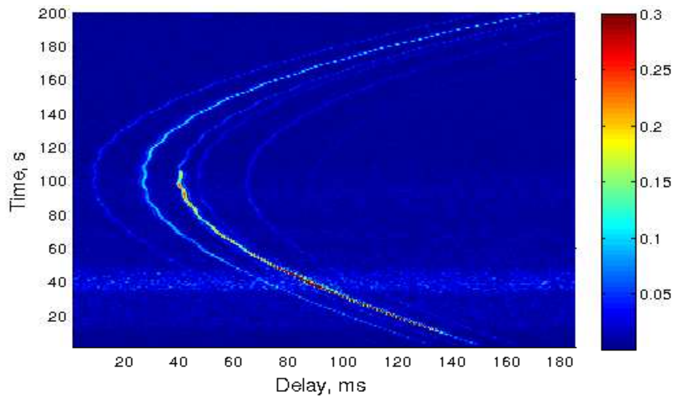

(c) Summer SSP, transmitter moves past receiver (2 km).

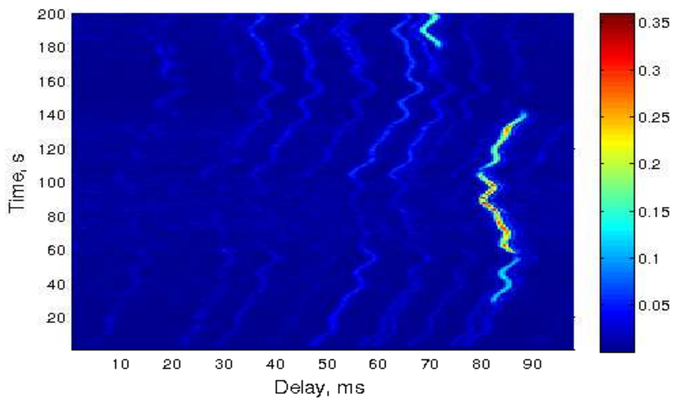

(d) Summer SSP, flower circle movement (5 km).

Figure 3.8: Fluctuations of the channel impulse response in the simulation scenarios (distance).

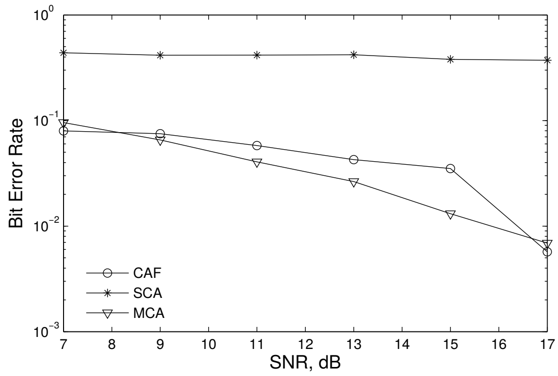

(a) Summer SSP, transmitter moves towards receiver, 10 km, 1/2 bps/Hz.

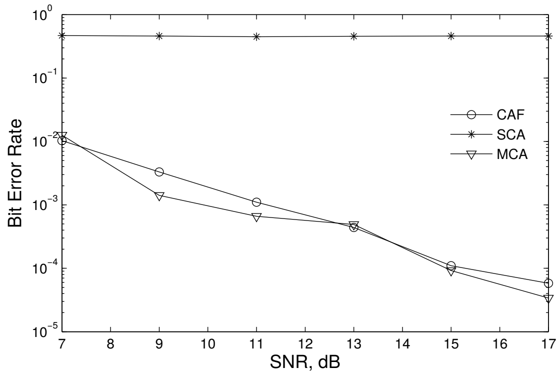

(b) Winter SSP, transmitter moves towards receiver, 20 km, 1/2 bps/Hz.

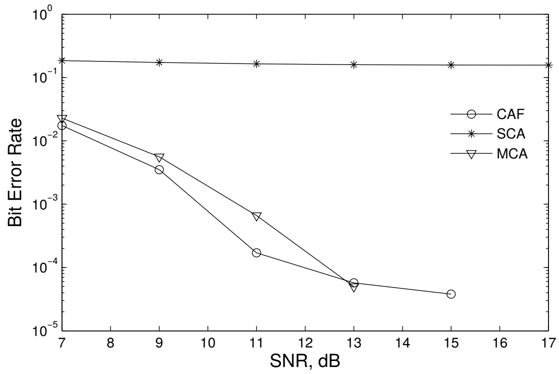

(c) Summer SSP, transmitter moves past receiver, 2 km, 1/3 bps/Hz.

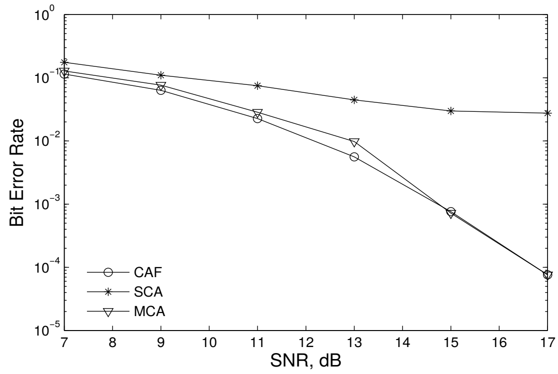

(d) Summer SSP, flower circle movement, 5 km, 1/3 bps/Hz.

Figure 3.9: BER performance of the receiver with the three Doppler estimation methods in the four simulation scenarios (environment, scenario, distance, spectral efficiency).

shows the BER performance of the receiver with the three Doppler estimation methods. It can be seen that the SCA method shows poor performance, whereas the MCA estimator again shows a performance similar to that of the CAF method.

In this scenario, the maximum transmitter/receiver speed is $V_{max} = 6$ m/s and the maximum acceleration is $U_{max} = 0.7$ m/s^2. From (3.43) and (3.44) we obtain that the CAF method requires 51 Doppler channels and the MCA method requires 7 channels, i.e., the MCA method requires 7 times less computations than the CAF method.

3.5.3 Flower circle movement of transmitter

AUVs can use complicated trajectories for underwater imaging, monitoring and sea bottom searching [88–93]. A complicated trajectory is considered in this scenario as shown in Figure 3.6(c); the trajectory of the transmitter looks like a petaled flower. The receiver moves at a speed of $v_r = 6$ m/s. The distance D(t) between the transmitter and receiver is described as

$$D(t) = \sqrt{(D_0 - v_r t)^2 + [K \sin(12\pi t/T) + 2]^2 - 2(D_0 - v_r t)[K \sin(12\pi t/T) + 2] \cos(2\pi t/T)}, \tag{3.48}$$

where $D_0 = 5$ km is the initial distance at $t = 0$ between the central point (point O in Figure 3.6(c)) of the flower and receiver, $K = 2$ m, and $T = 100$ s the period of passing one flower circle; the external radius of the flower is 3 m.

Figure 3.8(d) shows fluctuations of the channel impulse response in this scenario and Figure 3.9(d) shows the BER performance of the receiver. It can be seen that the SCA method is outperformed by the other two methods, which show similar performance.

In this scenario, the transmitter moves with a relatively low time-varying speed, $v_t \leq 0.38$ m/s. The maximum transmitter/receiver speed is $V_{\max} = 6.8$ m/s, and the maximum acceleration is $U_{\max} = 0.29$ m/s^2. From (3.43) and (3.44), we obtain that the CAF method requires 59 Doppler channels and the MCA method requires only 3 channels; thus the MCA method has almost 20 times less complexity than the CAF method.

From this numerical investigation, we can conclude that the proposed MCA method significantly outperforms the SCA method and provides a performance similar to that of the CAF method. However, the complexity of the MCA method is significantly lower than the CAF complexity.

3.6 Sea Trial Results

In this section, we compare the performance of the three Doppler estimation methods using data recorded in two deep-water sea trials, with low and high speeds, respectively.

3.6.1 Low speed of transmitter

In the first sea trial, the communication signals (guard-free OFDM symbols) with a duration of 33 minutes were transmitted in the frequency interval 640-896 Hz at a distance of 3 km from a drifting transmitter to a drifting omnidirectional receiver; the relative speed was about 0.5 m/s. The depth of both the transmitter and receiver were at 200 m. Figure 3.10(a) shows fluctuations of the channel impulse response in this sea trial.

Table 3.1: BER performance of the receiver with the three Doppler estimators in the low speed sea trial; spectral efficiency: 1/2 bps/Hz.

Doppler estimator	**BER for code**		
	[3 7]	**[23 35]**	**[561 753]**
CAF	2.4×10^{-5}	0	0
SCA	1.0×10^{-3}	1.0×10^{-3}	1.4×10^{-3}
MCA	4.1×10^{-5}	0	0

The BER performance of the receivers with the three Doppler estimators is shown in Table 3.1. Note that, since in this sea trial the speed and acceleration of the transmitter/receiver were low, we would expect a similar performance for the SCA and MCA methods. It can be seen that the proposed MCA estimator guarantees the performance comparable to that of the CAF method, and it still outperforms the SCA method. Thus, even in this low-speed case, the proposed estimator results in the performance improvement. Note that in communication

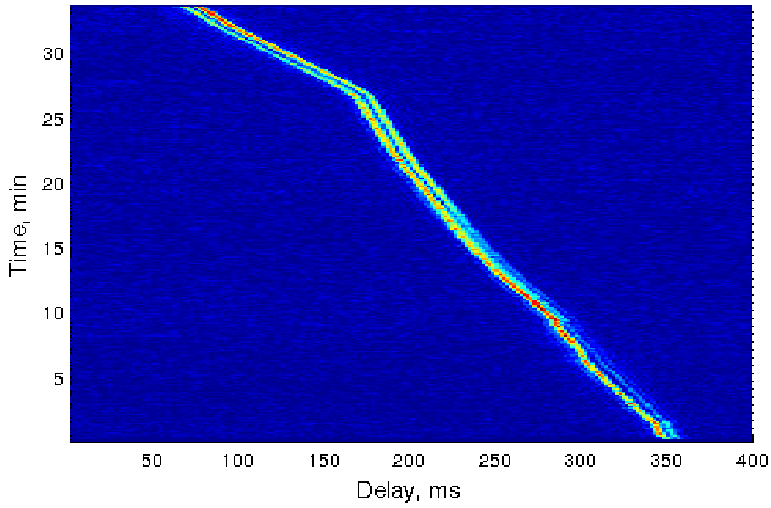

(a) Indian Ocean; low speed, short distance.

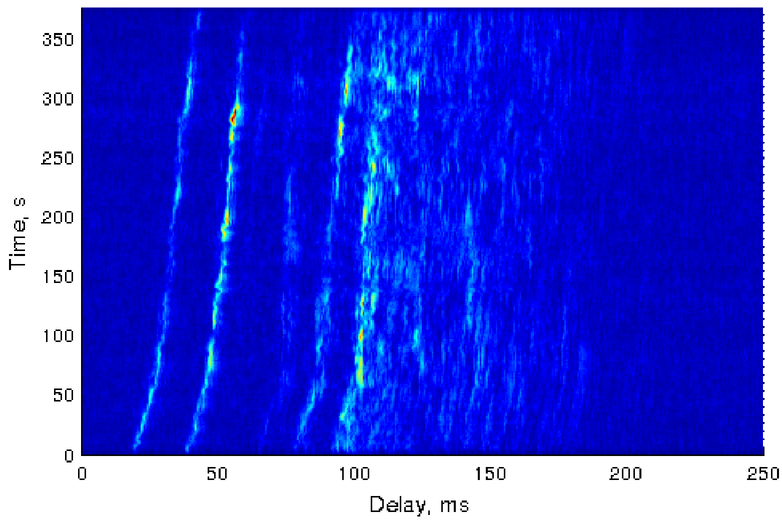

(b) Pacific Ocean; high speed, long distance.

Figure 3.10: Fluctuations of the channel impulse response in the two sea trials.

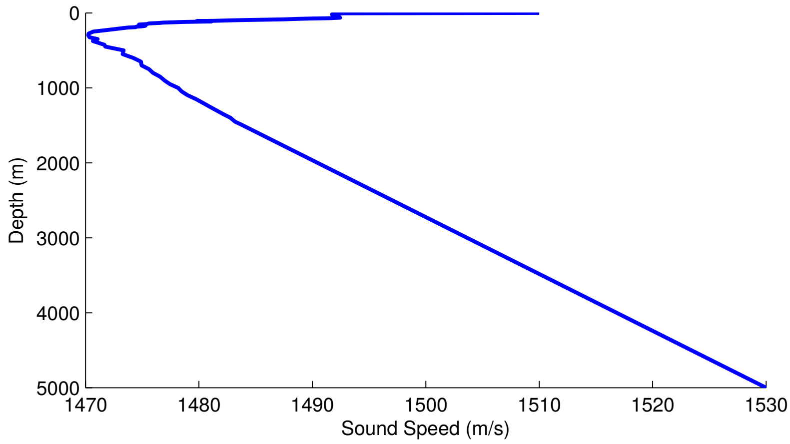

Figure 3.11: SSP in the second sea trial.

systems, the convolutional code is used for error-correcting that generates parity symbols via sliding application of polynomial function to the data stream [105], it is not necessary for a receiver to achieve better error-correcting performance with higher convolutional codes, especially in time-varying and complicated UWA channels.

In this sea trial, the CAF method requires 7 Doppler channels, whereas the MCA method requires only 3 channels; thus, the complexity of the MCA method is significantly lower. However, the BER performance of the two methods is similar, whereas the SCA method cannot provide the reliable detection.

3.6.2 High speed of transmitter

In the second sea trial, described as session F1-10 in [4], 376 guard-free OFDM symbols were transmitted at distances from 81 to 79 km. The transducer was towed at a depth of 200 m by a surface vessel moving at a speed of about 6–7 m/s towards a receiver. Due to the surface waves affecting the towing vessel, the transducer exhibited random oscillations around the main trajectory with an average period about 10 s [4]; this resulted in an acceleration between the transmitter and receiver. The receive omnidirectional hydrophone was slowly drifting at a depth of 400 m. Figure 3.11 shows the SSP in the sea trial. The SNR for the received signals is shown in Figure 3.12. The average SNR during the session is about 11 dB. Figure 3.10(b) shows fluctuations of the channel impulse response in the sea trial, after removing the dominant time-varying delay corresponding to the transmitter speed 6 m/s. It is seen that the

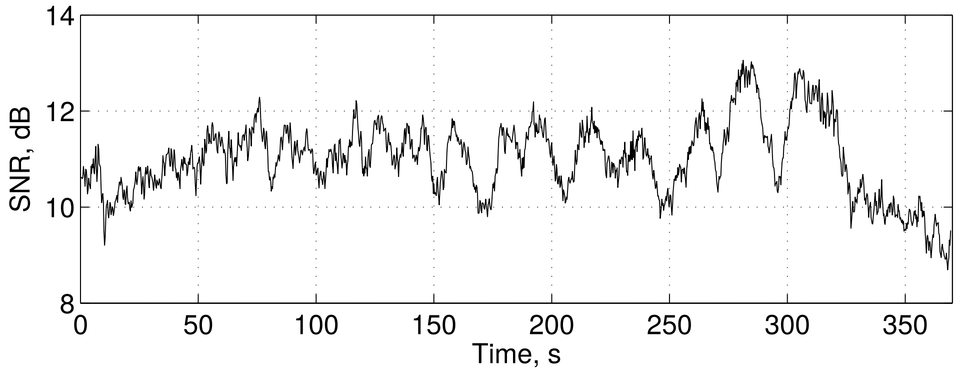

Figure 3.12: Time-varying SNR in the F1-10 sea trial.

channel is characterized by a large number of fast-varying multipath components.

Table 3.2: BER performance of the receiver with the three Doppler estimators in the high speed sea trial; spectral efficiency: 1/2 bps/Hz.

Doppler estimator	**Code [3 7]**	**Code [23 35]**	**Code [561 753]**
CAF	$4.5 \cdot 10^{-3}$	$8.5 \cdot 10^{-4}$	$2.0 \cdot 10^{-5}$
SCA	0.30	0.34	0.37
MCA	$4.8 \cdot 10^{-3}$	$9.2 \cdot 10^{-4}$	0

The BER performance is shown in Table 3.2. The BER is shown for different coding schemes, characterized by the code polynomial, [3 7], [23 35], or [561 753] in octal. It can be seen that for all the codes, the MCA method shows a performance similar to that of the CAF method, and it is significantly better than the performance provided by the SCA method. This result is similar to that obtained in numerical experiments in Section 3.5.

The poor performance of the SCA method can be explained using Figure 3.13(a) and Figure 3.13(b) showing $|A_{\mathrm{MCA}}(\tau, \omega_m)|$ with 7 Doppler channels, $m = 1, \ldots, 7$. The variable $m = 4$ corresponds to $\omega_m = 0$, i.e., $A_{\mathrm{MCA}}(\tau, \omega_4) = A_{\mathrm{SCA}}(\tau)$. Figure 3.13(a) illustrates a case, when the peak of $|A_{\mathrm{MCA}}(\tau, \omega_m)|$ is in the Doppler channel $m = 4$; in this case, the SCA method performs as the MCA method. However, in another case, illustrated by Figure 3.13(b), the peak is at $m = 2$, the SCA method cannot detect the peak, and, consequently, the detection performance of the receiver is poor.

In this sea trial, the CAF method requires 61 Doppler channels, whereas the MCA method requires only 7 channels; thus, the complexity of the MCA method is significantly lower.

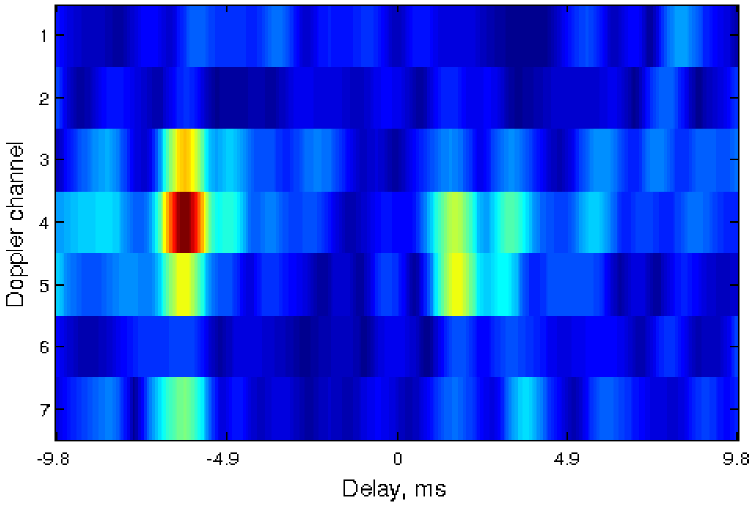

(a) A case of low acceleration.

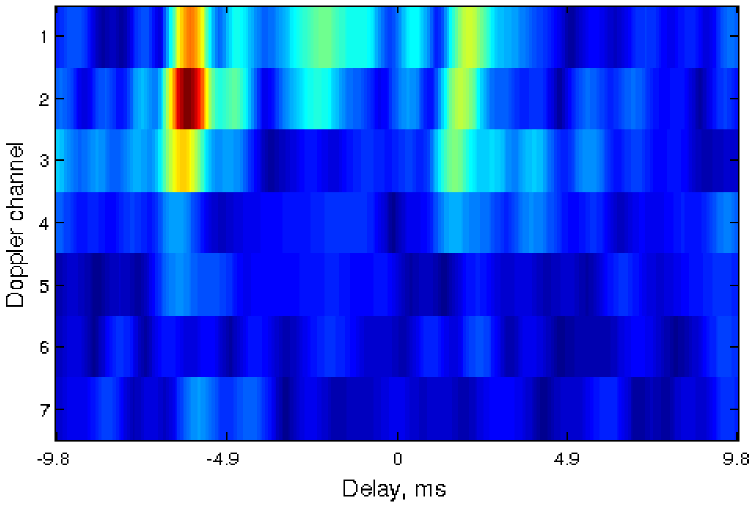

(b) A case of high acceleration.

Figure 3.13: Examples of the time-frequency autocorrelation function $|A_{\mathrm{MCA}}(\tau, \omega_m)|$ in the sea trial.

However, the BER performance of the two methods is similar, whereas the SCA method cannot provide reliable detection.

3.7 Summary

In this chapter, we proposed and investigated a new (multi-channel) autocorrelation method for Doppler estimation in fast-varying UWA channels. The proposed method not only measures the time compression over the estimation interval, but also the gradient of the time compression, thus allowing more accurate (with time-varying sampling rate) resampling of the received signal to compensate for the Doppler distortions. The proposed method has been compared with a single-channel autocorrelation method and a method based on computing the cross-ambiguity function between the received and pilot signals. The results in shallow water simulation scenarios and in the two deep ocean sea trials demonstrate that the proposed method outperforms the single-channel autocorrelation method, and it is comparable in the performance to the method based on computation of the cross-ambiguity function. However, the proposed method requires significantly less computations.

Chapter 4

Efficient Use of Space-time Clustering for UWA OFDM Communications

Contents

4.1 Introduction

In UWA communication channels, received signals are spread in angle and delay of arrival [38]. In many communication scenarios, e.g., in deep-water channels, the spreading is concentrated around a few specific directions of arrival (DOAs) and delays [35, 40, 41, 106]. We refer to this phenomenon as the space-time clustering, and exploit it to improve the detection performance and reduce complexity of a receiver. The receiver that we consider here utilises a vertical linear array (VLA) of hydrophones. For improving the detection performance, an efficient way is to combine signals from multiple diversity branches [38, 107, 108], e.g., from antenna array elements. However, with combining applied directly to antenna elements, a large number of elements is required to achieve a good bit error rate (BER) performance in scenarios with a low signal-to-noise ratio (SNR). In such receivers, the complexity is proportional to the number of antenna elements and can be high.

The space-time clusters introduce a natural diversity, which can be used to improve the detection performance and reduce the complexity. In order to exploit this opportunity, the clusters need to be identified, which, in particular, requires estimation of the spatial signal distribution [35, 109]. Spatial filters (SFs) estimate the spatial signal distribution and choose single or multiple directions from this distribution for diversity combining [35, 40, 41]. If directions for further processing are chosen based on the maximum power of arrived spatial signals, several directions from the same space cluster can be chosen, which limits the receiver performance due to correlation of the diversity branches. For achieving a high performance when processing wideband communication signals, a SF would combine properly delayed signals from antenna elements. This requires delays to be fractional with respect to the sampling interval used for analogue-to-digital conversion (ADC) of the received signals, and for every DOA of interest applying specific sets of delays. As a result, such SFs possess a high complexity.

In this chapter, we investigate a receiver with space-time processing of orthogonal frequency-division multiplexing (OFDM) signals. In the receiver, a SF computes a spatial signal distribution to estimate DOAs, and further uses these estimates in beamformers to form space diversity branches. We propose a SF that does not require delaying the signals from antenna elements and therefore it is of reduced-complexity compared to the SF with fractional delays. In every diversity branch, an equalizer compensates for the Doppler effect and performs the multipath combining. Finally, the equalized signals from the diversity branches are combined using the maximal ratio combining (MRC) [107], demodulated and decoded. We investigate the performance of the receiver with proposed and existing space-time processing techniques, and find that the receiver exploiting the space-time clustering demonstrates an improved performance and reduced complexity. The investigation is based on processing signals recorded on a 14-element VLA in a sea trial at a distance of 105 km with a transducer moved at a speed of 6 m/s. In these conditions, when exploiting the space-time clustering, an error-free data transmission is achieved with a spectral efficiency of 0.33 bps/Hz.

4.2 Space-time Clusters in UWA Channels

In this section, we show examples of space-time clusters observed in sea trials at distances from 30 km to 110 km. The acoustic environment is characterised by the sound speed profile shown in Figure 3.11. The sea depth is about 5 km, and the minimum sound speed is at a depth of about 300 m. In the trials, communication signals are transmitted in the frequency band 2560-3584 Hz; a transducer is towed at a depth of around 250 m and a receive VLA of 14 hydrophones is placed at a depth of around 420 m. Figure 4.1 shows the hydrophone positions within the VLA of a total length of 8.1 m; the inter spacing between hydrophones differs from 0.3 m to 1.2 m.

Space-time distribution of received signals are shown in Figures 4.2-4.3 for various distances between the transmit and receive antennas. It can be seen that in all the cases, the signal distributions are characterised by several peaks representing what we call space-time clusters. These clusters can provide natural diversity branches in a receiver.

When describing the receiver below, data from these experiments can be used. For illustration, we will be using the experimental data obtained at a distance of 105 km, see Figure 4.3(c).

4.3 Transmitted Signal and Channel Model

The transmitted signal $s(t)$ described in Section 3.4 is used here.

The UWA channel is often modelled as a time-variant linear system with an impulse response $h_m(t,\tau)$ that describes multipath and Doppler spreads in the channel. The received signal at the mth hydrophone is then given by

$$r_m(t) = \int_{-\infty}^{\infty} h_m(t,\tau)s(t-\tau)d\tau + \nu_m(t), \quad m = 1,\ldots,M, \tag{4.1}$$

where M is the number of hydrophones in the VLA, and $\nu_m(t)$ is the additive noise. Various models of $h_m(t,\tau)$ can be used; e.g., for a channel with Q discrete multipath components we

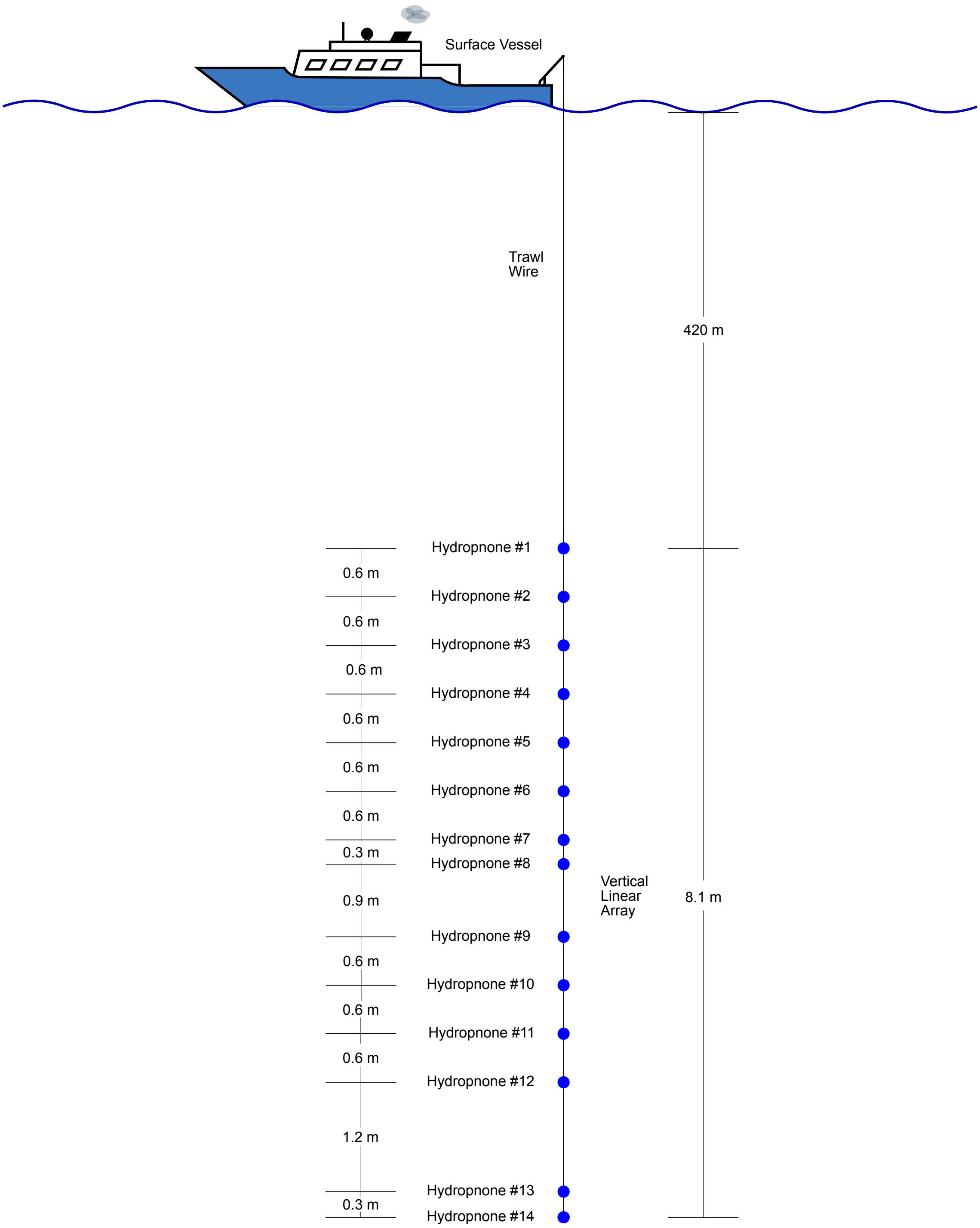

Figure 4.1: Vertical Linear Array of 14 hydrophones deployment in the sea trials.

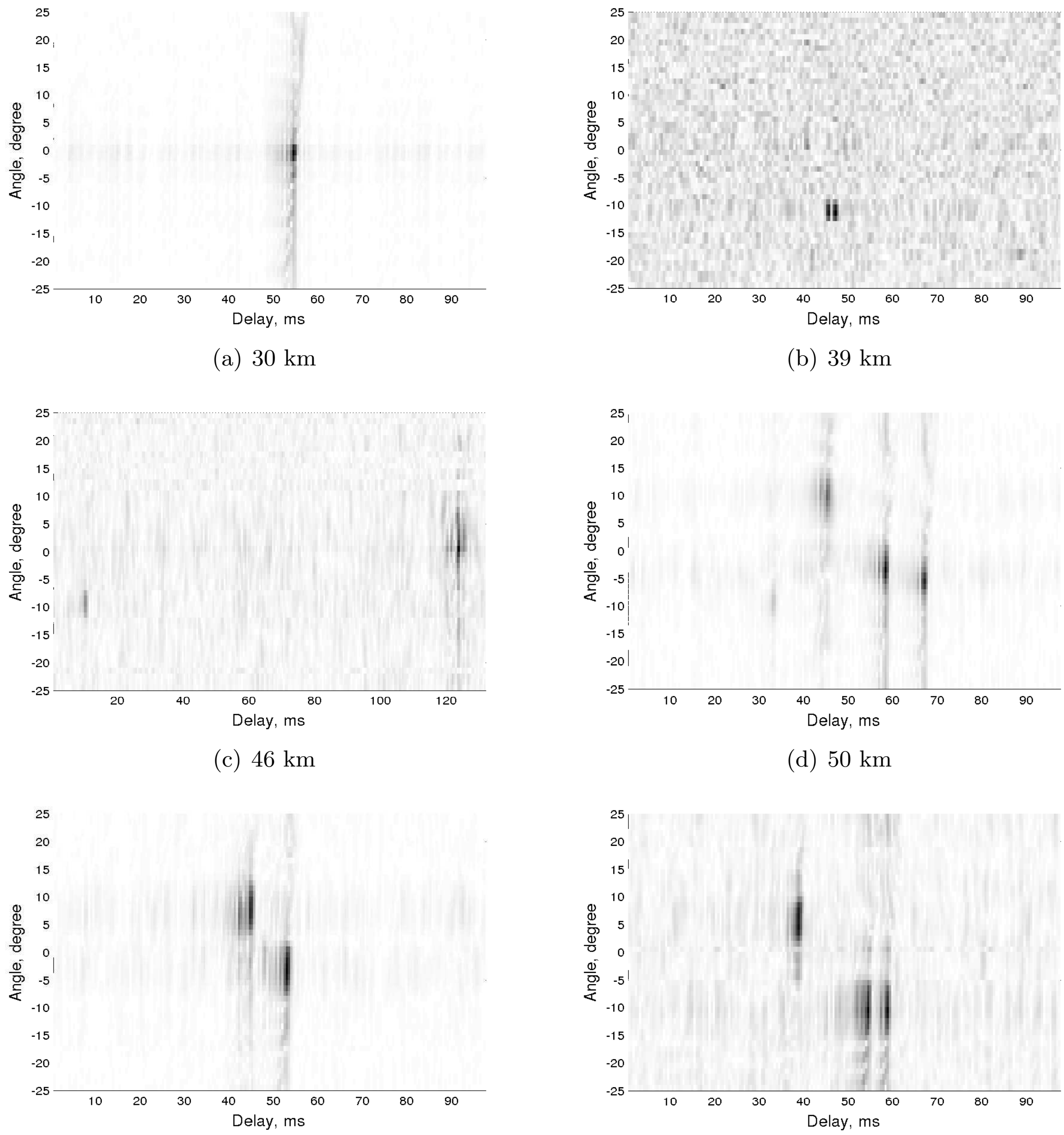

(a) 30 km (b) 39 km

(c) 46 km (d) 50 km

(e) 94 km (f) 100 km

Figure 4.2: Experimental space-time distributions of received signal observed at various distances from 30 km to 100 km.

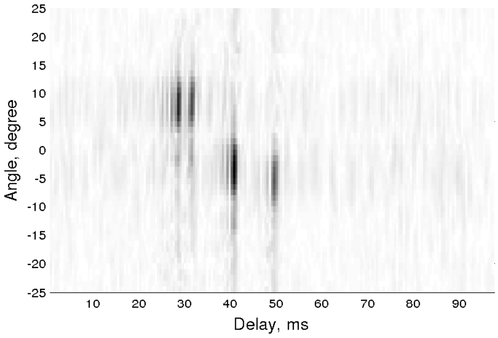

(a) 102 km

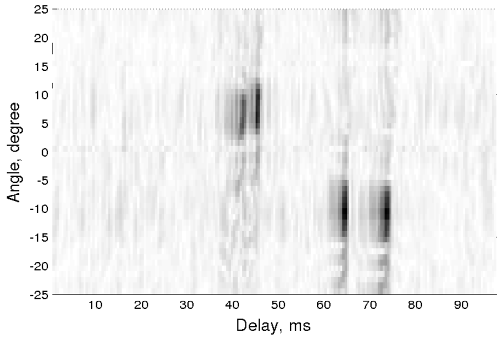

(b) 103 km

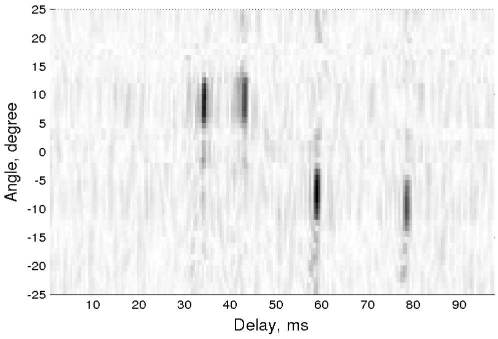

(c) 105 km

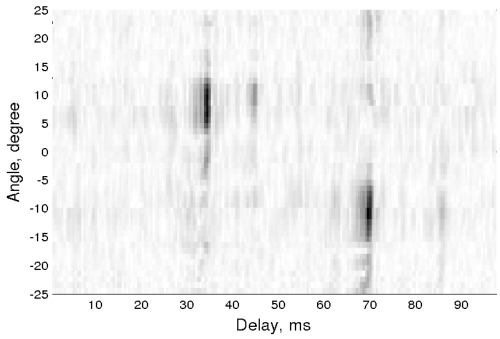

(d) 106 km

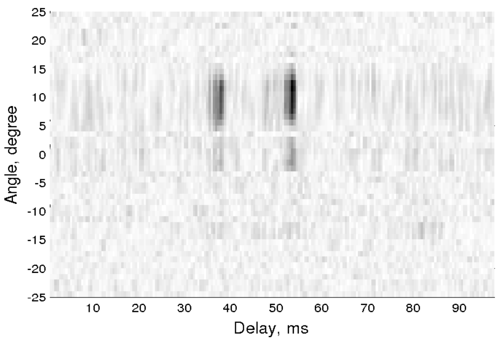

(e) 109 km

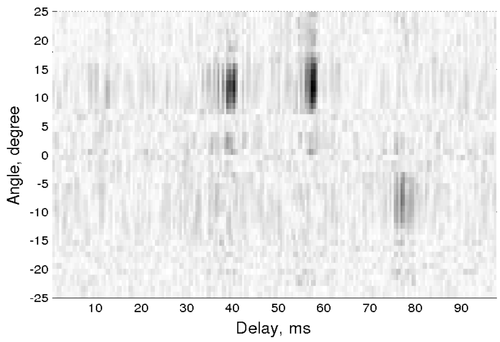

(f) 110 km

Figure 4.3: Experimental space-time distributions of received signal observed at various distances from 102 km to 110 km.

have [18, 110]:

$$h_m(t,\tau) = \sum_{q=1}^{Q} A_{q,m}\delta(\tau - \tau_{q,m}(t)), \tag{4.2}$$

where $A_{q,m}$ is the amplitude of the qth multipath component at the mth hydrophone, and $\delta(t)$ is the Dirac delta function. The time-variation of the impulse response is mainly due to the time-variation of delay rather than the slow time-variation of amplitude, so we can almost consider the amplitude in the (4.2) to be a constant value. The time variation of the delay $\tau_{q,m}(t)$ is caused by the Doppler effect; the slop (gradient) of the time dependence defines the time compression experienced by the signal. One of challenges in processing signals received in such a channel is due to different time compressions of signals received via different multipaths. As a consequence, the simple time compression operation, implemented in practice via resampling the received signal, cannot completely remove the Doppler distortion.

However, multipath components arrived from a particular (jth) direction tend to have close values of the time-compression factor. Therefore, the Doppler distortion in a signal from the jth direction can be accurately compensated by resampling. After the resampling, the channel can be modelled by a time-invariant impulse response

$$h_j(\tau) = \sum_{q=1}^{Q_j} A_{q,j}\delta(\tau - \tau_{q,j}), \tag{4.3}$$

where the delays $\tau_{q,j}$ are now constant and Q_j is the number of multipath components in the jth space branch, $Q_j \leq Q$. The time-invariant property of the impulse response allows a higher accuracy of channel estimation/equalization and, eventually, better detection performance of the receiver. A reduced channel delay spread in directional signals also allows a better detection performance and reduced complexity.

Signals received from several directions and equalized can be combined to further improve the detection performance. The performance after the diversity combining will not only depend on the energy of the received signals, but also on correlation of channels in diversity branches. It is therefore possible that weaker signals from uncorrelated directions after combining will provide a better detection performance compared to combining strong signals received from correlated directions.

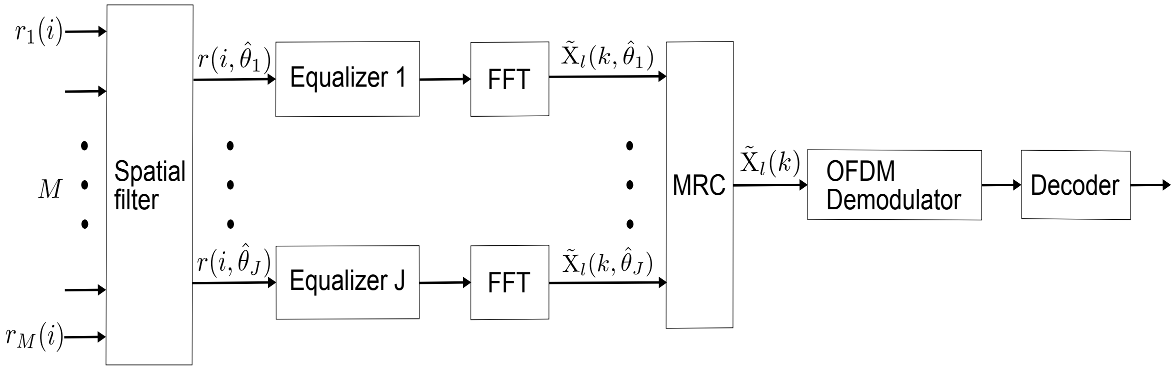

Figure 4.4: Block diagram of the receiver.

4.4 Space-time Processing in Receiver

In this section, we describe the receiver (see Figure 4.4). The analogue signals received by M hydrophones are bandpass filtered within the frequency band of the OFDM transmission and converted into the digital form $r_1(i)$ to $r_M(i)$ at a sampling rate f_s; $f_s = 4f_c = 12288$ Hz in our case. The digital signals $r_1(i)$ to $r_M(i)$ are processed in a SF that produces J directional signals $r(i, \hat{\theta}_j)$, $j = 1, \ldots, J$. The angles $\hat{\theta}_j$ are chosen from the average signal power as a function of DOA. The directional signals are equalized in time-domain, transformed into the frequency domain using the fast Fourier transform (FFT), and combined using the MRC. The combined frequency domain signal $\tilde{X}_l(k)$ is transferred to a demodulator and, after deinterleaving, further to the soft-decision Viterbi decoder [104].

4.4.1 Spatial filters

The following six SFs are considered here:

1. **Single-element SF**

   The signal $r_1(i)$ received at the first hydrophone is the only output of the SF.

2. **Multiple-elements SF**

   The M received signals $r_1(i), \ldots, r_M(i)$ are $J = M$ outputs of the SF.

3. **SF with a single direction corresponding to the maximum power of spatial distribution**

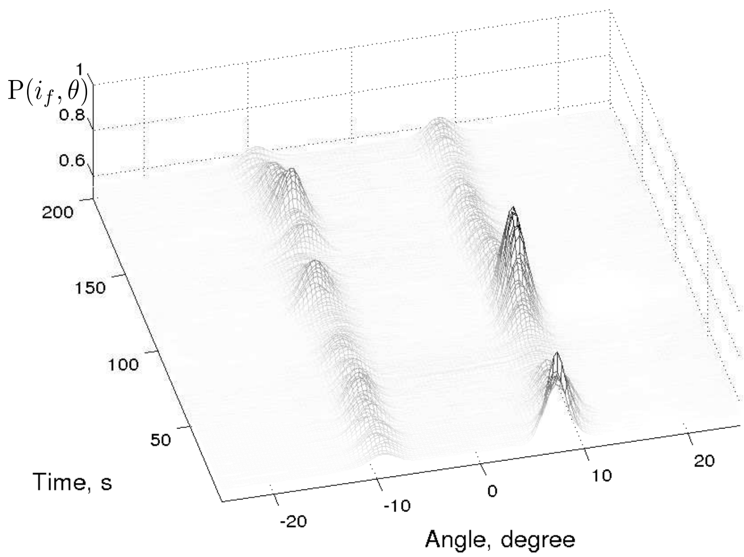

Figure 4.5: Spatial power distribution $\mathrm{P}(i_f;\theta)$ in the sea trial at a distance of 105 km; positive angles correspond to acoustic rays received from the sea surface direction while negative angles show rays from the sea bottom direction.

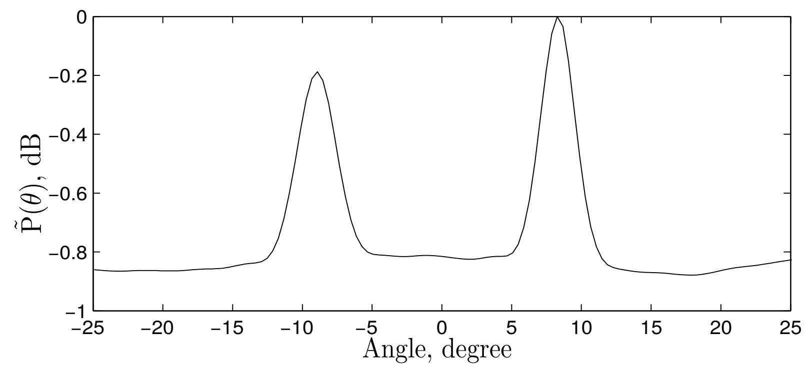

Figure 4.6: The average spatial signal power $\tilde{\mathrm{P}}(\theta)$; obtained at angle step 0.4°.

The time-varying power $\mathrm{P}(i_f;\theta)$ (see Figure 4.5, where i_f is the time instant) and the average power $\tilde{\mathrm{P}}(\theta)$ (see Figure 4.6) are computed in a DOA estimator (see Figure 4.7) as explained below in Section 4.4.2.

Based on the maximum power of the spatial distribution, a single ($J = 1$) direction $\hat{\theta}_1$ is chosen:

$$\hat{\theta}_1 = \arg\max_{\theta} \tilde{\mathrm{P}}(\theta). \tag{4.4}$$

The beamformer produces a single directional signal $r(i, \hat{\theta}_1)$.

4. **SF with J directions corresponding to J maxima of spatial distribution**

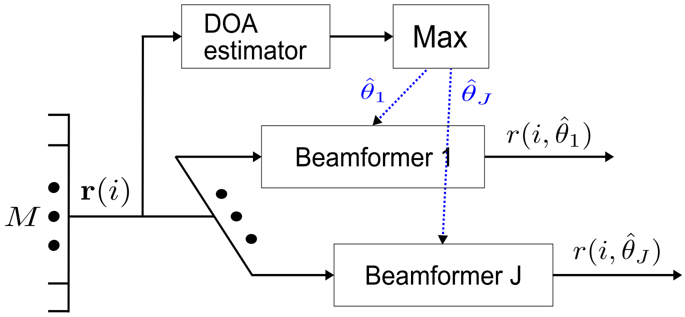

Figure 4.7: Block diagram of the SF with J outputs based on maxima of the spatial signal power.

In this case (see Figure 4.7), several directions ($J \geq 2$) are chosen, corresponding to the first J maxima of the average power distribution $\tilde{\mathrm{P}}(\theta)$:

$$[\hat{\theta}_1, \dots, \hat{\theta}_J] = \arg\max_{\theta} \tilde{\mathrm{P}}(\theta). \tag{4.5}$$

Note that the function $\tilde{\mathrm{P}}(\theta)$ is computed on a grid of angles θ; in our experiments here, we use a grid within the interval $\theta \in [-25^\circ, 25^\circ]$ with a step of 0.4°.

5. **Proposed SF with J directions corresponding to J space clusters**

   In this SF, a peak detector $\mathbb{P}$ (in the software MATLAB, the function "findpeaks" can be used) finds J local maxima of $\tilde{\mathrm{P}}(\theta)$, which are considered to correspond to space clusters. With this technique, two ($J = 2$) space clusters are identified in the experiment at the distance 105 km (see Figure 4.3(c)). The two clusters occupy angle intervals $[6^\circ, 11^\circ]$ and $[-12^\circ, -6^\circ]$, but in each of them, a single angle $\hat{\theta}_j$ ($\hat{\theta}_1 = 8.4^\circ$ and $\hat{\theta}_2 = -9^\circ$, respectively) is chosen for further processing:

$$[\hat{\theta}_1, \dots, \hat{\theta}_J]^T = \mathbb{P}[\tilde{\mathrm{P}}(\theta)]. \tag{4.6}$$

6. **SF with fractional delays and J directions corresponding to J space clusters**

   In SFs 3, 4 and 5 described above, low-complexity DOA estimation and beamforming techniques presented below in Section 4.4.2 are used. More accurate but also more complicated DOA estimation and beamforming are used in the SF with fractional delays. For achieving a high accuracy when processing wideband signals, such as communication signals, both the DOA estimator and beamformer should operate by introducing delays (fractional delays with respect to the sampling interval) in the hydrophone signals, the delays being different for each direction, and processing each direction separately from other directions, which make this SF complicated [35].

4.4.2 DOA estimator and beamformer

The DOA estimator computes the spatial power distribution to estimate DOAs, then beamformers, using these DOA estimates, produce directional signals. In this section, we propose simplified DOA estimator and beamformer not requiring the fractional delays.

1. **DOA estimator**

The DOA estimator computes the spatial power distribution of the received signal by processing the hydrophone signals $r_1(i)$ to $r_M(i)$. The ith time-domain snapshot of received signals is described as an $M \times 1$ vector $\mathbf{r}(i) = [r_1(i), r_2(i), \ldots, r_M(i)]^T$. The snapshots are divided into N_f frames, I_f snapshots each. A frame is divided into N_{sf} non-overlapping subframes of U snapshots each, i.e., $I_f = N_{sf}U$. The subframes are transformed into the frequency domain; the $M \times 1$ frequency domain snapshot at frequency ω_k for a subframe starting at time u is given by

$$\mathbf{z}(u;k) = \sum_{n=0}^{U-1} \mathbf{r}(u+n) e^{-j\omega_k n/f_s}, \tag{4.7}$$

where $k = 0, \ldots, K-1$, $K = 2\pi F/\Delta\omega$, F is the bandwidth of interest, $\omega_k = \omega_0 + k\Delta\omega$, $\Delta\omega = 2\pi f_s/U$, and ω_0 the lowest frequency of interest. For a frame starting at time i_f, for every frequency ω_k, the $M \times M$ spectral density matrix (SDM) is computed as [111]:

$$\mathbf{Y}(i_f;k) = \frac{1}{N_{sf}} \sum_{n_{sf}=0}^{N_{sf}-1} \mathbf{z}(i_f + n_{sf}U;k)\mathbf{z}^H(i_f + n_{sf}U;k) + \kappa \mathbf{I}_M, \tag{4.8}$$

where $(\cdot)^H$ denotes the conjugate transpose, $\mathbf{I}_M$ an $M \times M$ identity matrix, and κ a loading factor which is a small positive number related to the noise level.

The SDM $\mathbf{Y}(i_f;k)$ is used for obtaining the spatial power at every angle of arrival θ. Due to the minimum variance distortionless response (MVDR) algorithm [112, 113] is less sensitive to perturbations and model errors than Maximum Likelihood (ML), Multiple Signal Classification (MUSIC), and Estimation of Signal Parameters via Rotational Invariance Technique (ESPRIT) [114], the MVDR is suitable for both DOA estimation and optimal beamforming in underwater acoustic channels and used in the spatial filter. For a frequency ω_k, the steering vector is given by

$$\mathbf{v}(\theta, k) = \left[1, \ldots, e^{-j\omega_k \frac{\mathrm{D}(m)\sin(\theta)}{c}}, \ldots, e^{-j\omega_k \frac{\mathrm{D}(M)\sin(\theta)}{c}}\right]^T, \tag{4.9}$$

where $\mathrm{D}(m)$ is the distance between the first ($m = 1$) and mth hydrophone (see Figure 4.1) and the sound speed $c = 1.5$ km/s. The power at frequency ω_k from a direction θ is given by

$$\mathrm{P}_k(i_f; \theta) = \left[\mathbf{v}^H(\theta, k)\mathbf{Y}^{-1}(i_f; k)\mathbf{v}(\theta, k)\right]^{-1}. \tag{4.10}$$

The total power over all frequencies

$$\mathrm{P}(i_f; \theta) = \sum_{k=0}^{K-1} \mathrm{P}_k(i_f; \theta), \tag{4.11}$$

is shown in Figure 4.5. The average power over N_f frames (shown in Figure 4.6) is given by

$$\tilde{\mathrm{P}}(\theta) = \frac{1}{N_f} \sum_{n_f=1}^{N_f} \mathrm{P}(i_f; \theta). \tag{4.12}$$

2. **Beamformer**

For a chosen direction $\hat{\theta}_j$, for cancelling the interference arriving from the other directions, the beamformer weight vector $\bar{\mathbf{w}}_{n_f}(\hat{\theta}, k)$ in the n_fth frame is calculated as [112]

$$\bar{\mathbf{w}}_{n_f}(\hat{\theta}_j, k) = \mathbf{Y}^{-1}(i_f; k)\mathbf{v}(\hat{\theta}_j, k)\mathrm{P}_k(i_f; \hat{\theta}_j). \tag{4.13}$$

The weight vector is then smoothed in time:

$$\mathbf{w}_{n_f}(\hat{\theta}_j, k) \leftarrow \lambda \mathbf{w}_{n_f-1}(\hat{\theta}_j, k) + (1 - \lambda)\bar{\mathbf{w}}_{n_f}(\hat{\theta}_j, k), \tag{4.14}$$

where $0 \leq \lambda < 1$ is a forgetting factor, and $\mathbf{w}_0(\hat{\theta}_j, k) = \bar{\mathbf{w}}_1(\hat{\theta}_j, k)$. Since the DOAs are relatively slowly varying in time (see Figure 4.5), the forgetting factor λ can be chosen close to unity, providing a good filtering of the noise and interference; in our experiment, we set $\lambda = 0.998$. The directional signal is then computed as

$$r(i, \hat{\theta}_j) = \sum_{k=0}^{K-1} \mathbf{w}_{n_f}^H(\hat{\theta}_j, k)\mathbf{z}(u; k)e^{j\omega_k n/f_s}, \tag{4.15}$$

where $i = i_f + (n_{sf} - 1)U + n$.

3. **Complexity of the proposed SF**

   For the DOA estimation, the proposed SF requires the time-frequency transform (4.7), computation of the SDM (4.8), and the power computation (4.10); complexity of the other processing steps is significantly lower and can be ignored. The complexity of the three steps are given by $2KMI_f$, $4KN_{sf}M^2$, and $4(KM^3 + KN_\theta M^2)$ real-valued multiply-accumulate operations per second (MACs), respectively, where $I_f = f_s$ in our experiments, and N_θ is the number of angles in the DOA grid. In the beamformer, the frequency-time transform (4.15) needs to be performed; the other operations require significantly lower complexity. This transform requires $(4KMN_{sf} + 4Kf_s)$ MACs; for J beamformers, this should be multiplied by J. For example, with $M = 14$, $K = 32$, $N_{sf} = 32$, $N_\theta = 126$, $J = 2$, and $f_s = 12288$ Hz, which are values used in the receiver in Section 4.5, the total complexity of the SF is 1.9×10^7 MACs. Note that the complexity of the SF with fractional delays [35] with the same parameter values is about 1.3×10^9 MACs; thus, in this scenario, the proposed SF is about 70 times less complicated than the SF with fractional delays.

4.4.3 Equalizer

Once a directional signal $r(i, \hat{\theta}_j)$ has been obtained, it is applied to the equalizer shown in Figure 4.8, where the signal is down-shifted and low-pass filtered (LPF) to produce the baseband digital signal $\tilde{r}(i, \hat{\theta}_j)$. The signal $\tilde{r}(i, \hat{\theta}_j)$ is resampled to compensate for the Doppler effect and linearly equalized.

1. **Doppler estimator**

   Figure 4.9 shows the block diagram of the Doppler estimator, where the time-varying dominant Doppler scale factor and delay are estimated by computing the ambiguity function as follows. Firstly, the baseband signal $\tilde{r}(i, \hat{\theta}_j)$ is resampled with a number

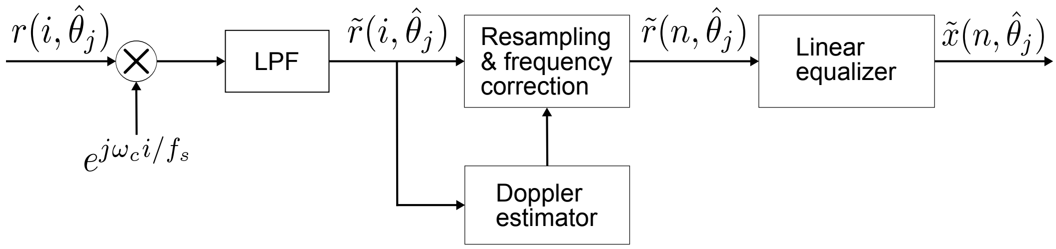

Figure 4.8: Block diagram of the equalizer.

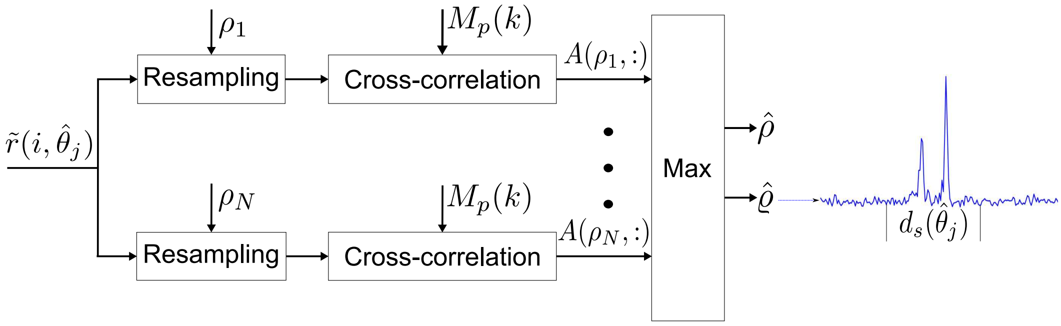

Figure 4.9: Block diagram of the Doppler estimator.

of compression factors ρ_n, $n = 1, \ldots, N$. Then, N Doppler sections of the ambiguity function [26] between the received and pilot signals are computed on the *delay-Doppler scale* grid [26, 57, 115]. The ambiguity function $A(\rho, \varrho)$ (see [4] for details), where ρ indicates the ρth Doppler section and ϱ indicates the ϱth delay, is used to estimate the dominant Doppler compression and delay:

$$[\hat{\rho}, \hat{\varrho}] = \arg\max_{\rho,\varrho} A(\rho, \varrho). \tag{4.16}$$

The estimated dominant channel delay is used for the timing synchronization. In a multipath channel, however, there will be a delay spread. Using the $\hat{\rho}$th Doppler section, the Doppler estimator also estimates the delay spread $d_s(\hat{\theta}_j)$ (see Figure 4.9). The estimated delay spread is used to set the length of the linear equalizer as explained below in Section 4.5.

2. **Linear equalizer**

Figure 4.10 shows the block diagram of the linear equalizer, which is based on channel estimation and finite impulse response (FIR) filtering [31]. The equalizer length is typically chosen as three to five times of the channel delay spread $d_s(\hat{\theta}_j)$ [42], and therefore, if the delay spread is reduced, the equalizer complexity can also be reduced.

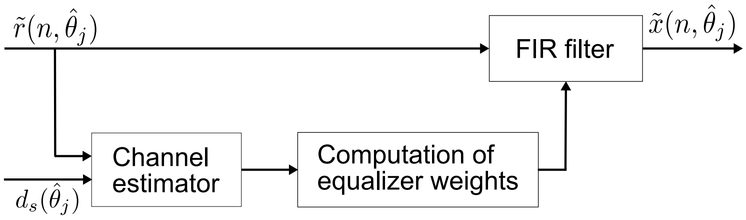

Figure 4.10: Block diagram of the linear equalizer.

In the channel estimator, a sparse recursive least squares (RLS) adaptive filter (see [31] for more details) is used to estimate the multipath structure of the directional signals. The equalizer weights are computed and interpolated as detailed in [4]. After FIR filtering, the equalized signals $\tilde{x}(n, \hat{\theta}_j)$ from all directions are linearly combined.

4.4.4 Diversity combining

The MRC is known to provide the highest SNR in the combined signal [107]. In general, phases of the complex-valued MRC weights should compensate for phase shifts in the directional signals, while the weight magnitudes should be proportional to SNRs in the directional signals. The phase compensation has already been achieved in the equalizer. Therefore, to compute the MRC weights, we only need to estimate SNRs in the equalized directional signals. The SNR estimates can be obtained from the superimposed pilot signal in the frequency domain since, after the equalization, the pilot and data sequences are separated.

In the lth symbol of the jth diversity branch, the residual error $e_l(j,k)$ at frequency k is computed as

$$e_l(j,k) = M_p(k) - \Re\{\tilde{X}_l(k;\hat{\theta}_j),\qquad(4.17)$$

where $\Re\{\tilde{X}_l(k;\hat{\theta}_j)\}$ is an estimate of the pilot sequence after the equalization. Since the pilot energy is $\sum_{k=1}^{N_s}|M_p(k)|^2 = N_s$ and the energy of the residual signal is $E_l(j) = \sum_{k=1}^{N_s}|e_l(j,k)|^2$, we adopt the following SNR estimate:

$$\mathrm{SNR}_l(j) = \frac{N_s}{\bar{E}_l(j)},\qquad(4.18)$$

where

$$\bar{E}_l(j) = \alpha \bar{E}_{l-1}(j) + (1-\alpha) E_l(j), \; l = 1, 2, \ldots, L, \tag{4.19}$$

$\bar{E}_0(j) = E_1(j)$, and the forgetting factor $0 \le \alpha < 1$ is chosen close to unity; in our experiment, $\alpha = 0.99$.

The MRC weight for the lth OFDM symbol in the jth diversity branch is then computed as

$$W_l(j) = \frac{\sqrt{\mathrm{SNR}_l(j)}}{\sum_{n=1}^{J} \sqrt{\mathrm{SNR}_l(n)}}, \; l = 1, 2, \ldots, L. \tag{4.20}$$

The combined signal in the frequency domain is then given by

$$\tilde{X}_l(k) = \sum_{j=1}^{J} W_l(j) \tilde{X}_l(k; \hat{\theta}_j). \tag{4.21}$$

Finally, the sequence $\tilde{X}_l(k)$ is demodulated, deinterleaved, and decoded.

4.5 Sea Trial Results

In this section, we compare BER performance and complexity of the receiver with the six SFs described in Section 4.4.1, firstly when all diversity branches have the same equalizer lengths, and secondly, with the equalizer lengths adaptively adjusted according to the estimated channel delay spreads.

We consider the sea trial at a distance of 105 km as described in Section 4.2. In this sea trial, $L = 200$ guard-free OFDM symbols were continuously transmitted.

When processing received signals in the proposed SF, the frame duration is set to 1 s with a number of subframes $N_{sf} = 32$ and number of snapshots in a subframe $U = 384$; $K = 32$ frequencies are processed in the bandwidth of interest, $F = 1024$ Hz, and the lowest frequency of interest is $\omega_0/(2\pi) = 2560$ Hz. The angles θ for DOA estimation are computed in the interval $[-25°, 25°]$ with an angle step of $0.4°$.

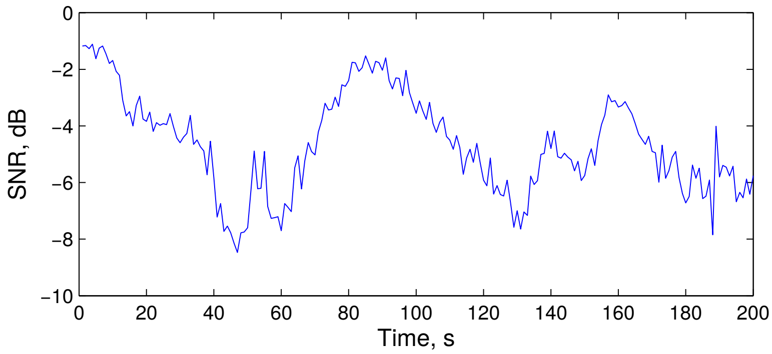

Figure 4.11: SNR at the first hydrophone in the sea trial at a distance of 105 km.

4.5.1 Comparison of spatial filters

In this subsection, results are presented for the case when the RLS filter length in the channel estimator is set to 75 ms, which matches to the channel delay spread at a single hydrophone, while the equalizer length is set to 250 ms.

Table 4.1 compares BER performance and complexity of the receiver with different SFs. It can be seen that the proposed DOA estimator and beamformer (introduced in Section 4.4.2 and used in SFs 3, 4 and 5) reduce the receiver complexity by 15 times compared to the receiver with the SF using fractional delays (SF 6). Note that a single equalizer branch requires about 8.3×10^7 MACs (see the complexity analysis in [4]).

Table 4.1: Comparison of receivers with different spatial filters

SF	**Comments**	**BER**	**Complexity** (10^6 MACs)
1	Single hydrophone	0.45	83
2	All 14 hydrophones	2.1×10^{-3}	1164
3	Single angle 8.4°	9.1×10^{-2}	100
4	Angles 8.4° and 8.8°	8.9×10^{-2}	185
5	**Cluster (8.4° and −9°)**	0	185
6	Cluster (8.4° and −9°)	0	1489

From Table 4.1, it can be seen that the receiver applied to a single hydrophone (SF 1) is unable to recover reliably the transmitted data. This is due to a low SNR on a single hydrophone, as seen in Figure 4.11, which is obtained from the result of the received signal energy divided by recorded noise energy in frames. The receiver with equalizers applied directly to all 14 antenna elements (SF 2) significantly reduces the BER, but the complexity greatly increases. With one or two diversity branches chosen based on the maxima of the average spatial power distribution (SF 3 and 4, respectively), the BER performance improves. The difference in the performance between these two SFs is small, but the complexity of the SF with two branches is almost twice higher. With DOAs corresponding to the two space clusters (SF 5), the receiver provides an error-free transmission. Such a receiver has the best performance and 6.3 times less complexity compared to the receiver with equalizers applied directly to 14 antenna elements (SF 2). SF 6 (with fractional delays) also allows an error-free transmission with the two branches, but its complexity is significantly higher than that of the receiver with the proposed SF 5.

Note that increasing the number of space diversity branches in SF 4 does allow improvement in the detection performance and with $J = 5$ such branches, an error-free transmission is also achieved. However, the complexity in this case would be the summation of the complexity of a spatial filter with 5 beamformers (2.5×10^7 MACs), and 5 equalizer branches complexity (4.15×10^8 MACs), which is 4.4×10^8 MACs, about 2.4 times higher than that of the SF 5 with two branches. Note that one MAC here is one multiplication step.

4.5.2 Equalizer optimization

Figure 4.12(a) shows fluctuations of the channel impulse response over the communication session at the first hydrophone; there can be seen four multipaths. We now consider two signals from directions $\hat{\theta}_1 = 8.4^\circ$ and $\hat{\theta}_2 = -9^\circ$; fluctuations of channel impulse responses for these directions are shown in Figure 4.12(b) and Figure 4.12(c), respectively. It can be seen that the four multipaths are now split between the two directions. As a result, the delay spreads in the diversity branches are also reduced compared to that at a single antenna element. We can exploit this to further reduce complexity of the receiver by setting the channel estimator and equalizer lengths according to the delay spreads of directional signals.

The delay spread of the signal received at the first hydrophone is estimated as about 50 ms. To cover all delay fluctuations throughout the communication session, the RLS filter length

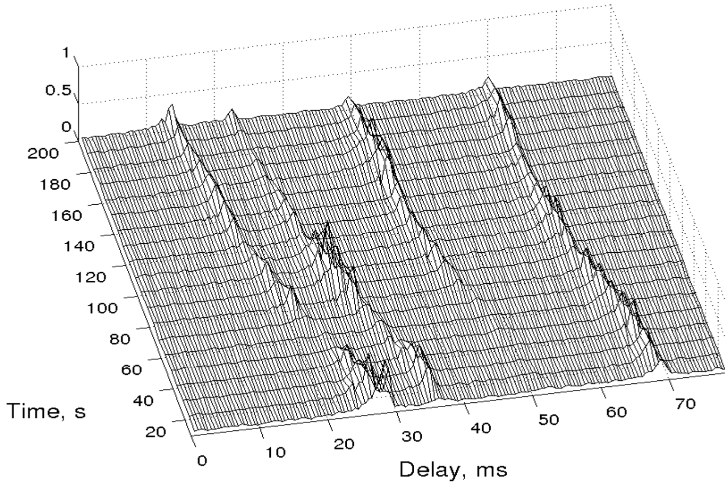

(a) Received signal at the first hydrophone.

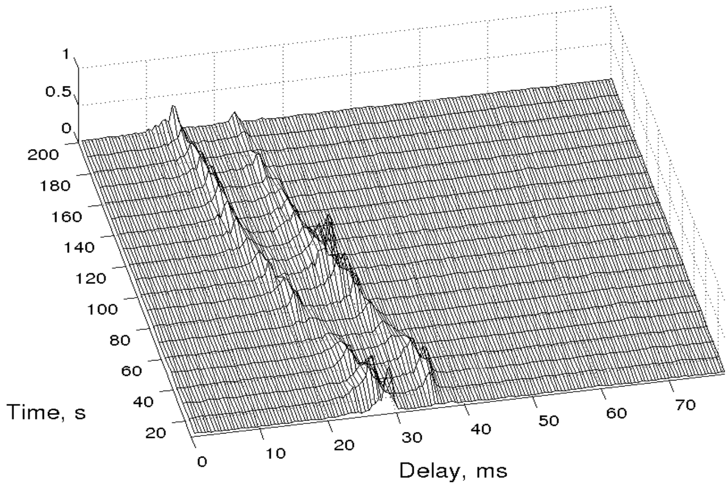

(b) Directional signal at $\hat{\theta}_1 = 8.4°$.

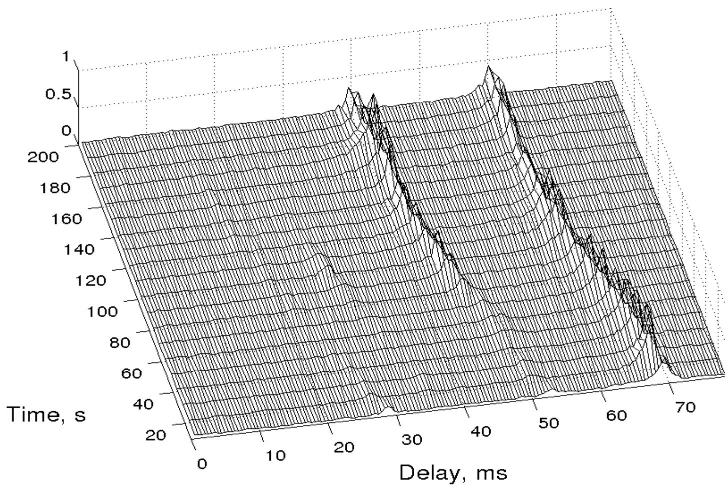

(c) Directional signal at $\hat{\theta}_2 = -9°$.

Figure 4.12: Fluctuations of the channel impulse response in the sea trial.

is set to 75 taps, with approximately 1 ms/tap; then the equalizer length is set to 250 taps. At angle $\hat{\theta}_1 = 8.4°$, the delay spread $d_s(\hat{\theta}_1)$ is estimated as 12 ms; the RLS filter length is set to 18 taps and the equalizer length is set to 60 taps. At angle $\hat{\theta}_2 = -9°$, the delay spread $d_s(\hat{\theta}_2)$ is estimated as 24 ms; the RLS filter length is set to 36 taps and the equalizer length is set to 120 taps.

The reduced delay spread in the diversity branches compared to the delay spread at a single hydrophone allows reduction in the receiver complexity. Moreover, the reduced number of channel taps to be estimated also allows a higher estimation accuracy.

Figure 4.13(a) shows the Doppler-delay spread of the signal arrived at the first hydrophone. It can be seen that the first and second groups of multipaths are Doppler-shifted with respect to each other. Therefore, the Doppler effect cannot be compensated by resampling the hydrophone signals; there will be a residual Doppler effect seen by the equalizer as fast channel fluctuations. Figure 4.13(b) and Figure 4.13(c) show the Doppler-delay spread of the two directional signals at angles $\hat{\theta}_1 = 8.4°$ and $\hat{\theta}_2 = -9°$, respectively. It can be seen that, compared to Figure 4.13(a), Doppler spreads in Figure 4.13(b) and Figure 4.13(c) are reduced, i.e., the speed of channel variation in the two diversity branches are also reduced, thus allowing a better channel estimation and equalization performance.

Table 4.2: Performance of the receiver with optimized equalizers

SF	**Equalizer lengths**	**BER for code**			**Complexity**
		[5 7 7]	[25 33 37]	[225 331 367]	(10^6 MACs)
5	250 taps, 250 taps	3.3×10^{-3}	1.6×10^{-4}	0	185
5	60 taps, 120 taps	2.8×10^{-3}	0.8×10^{-4}	0	94
6	250 taps, 250 taps	6.4×10^{-4}	3.9×10^{-4}	0	1489
6	60 taps, 120 taps	4.0×10^{-4}	1.1×10^{-4}	0	1398

Table 4.2 shows BER performance and complexity of the receiver, using SFs 5 and 6, with and without adjusting the equalizer length to the delay spread of directional signals. In the former case, both the equalizers are of length 250 ms, whereas in the later case, the equalizer length for the DOA $\hat{\theta}_1 = 8.4°$ is set to 60 ms and the equalizer length for the DOA $\hat{\theta}_2 = -9°$ is set to 120 ms. It can be seen that the shorter equalizers allow reduction in the complexity of the receiver with the proposed SF 5 by about 2 times. This is however is not

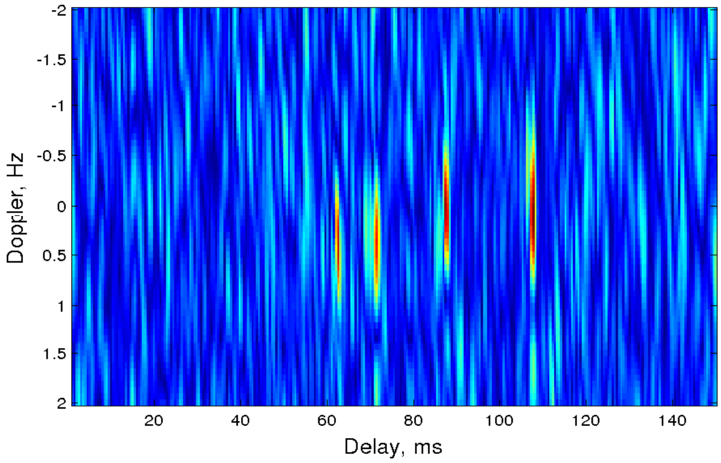

(a) Received signal at the first hydrophone.

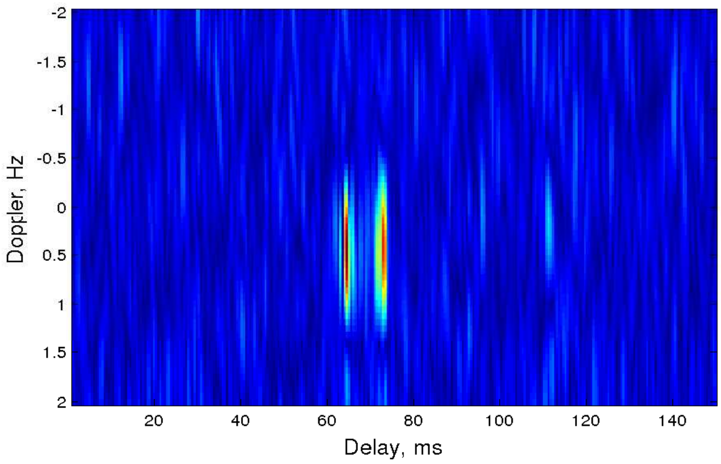

(b) Directional signal at $\hat{\theta}_1 = 8.4°$.

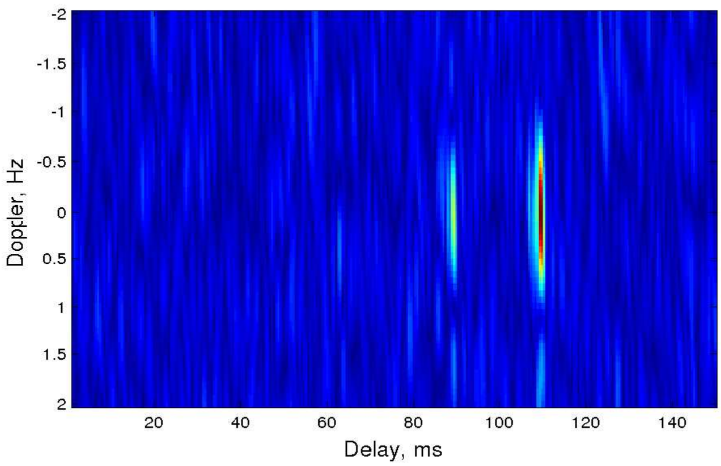

(c) Directional signal at $\hat{\theta}_2 = -9°$.

Figure 4.13: Doppler-delay spread of the signal received at the first hydrophone and directional signals.

the case for the receiver with SF 6, since the SF complexity dominates the receiver complexity.

With the stronger code with the polynomial [225 331 367] (see [104]), also used to obtain results in Table 4.1, the proposed SF with both long and short equalizers results in an error-free transmission. With weaker codes (polynomials [25 33 37] and [3 7 7]), the shorter equalizers allow a better detection performance. It can also be seen that the SFs 5 and 6 show similar detection performance for the stronger codes (polynomials [25 33 37] and [225 331 367]), and SF 6 shows somewhat better performance for only the weak code (polynomial [3 7 7]).

4.6 Summary

In this chapter, we investigated a receiver with various space filters for detection of OFDM signals in underwater acoustic communications. Analysis of signals recorded on a vertical linear antenna array in sea trials shows that the propagation channel is characterised by a number of space-time clusters. The use of the cluster structure of received signals in the spatial filter is shown to improve the detection performance of the receiver, compared to a multi-channel receiver with direct equalization of hydrophone signals or a receiver with directional signals generated based on the maxima of the spatial power distribution. Moreover, due to a reduced Doppler-delay spread of signals in clusters, extra performance improvement can be achieved with a reduced complexity. In this chapter, we have also proposed a spatial filter that has a significantly lower complexity compared to the spatial filter with fractional delays of hydrophone signals and still providing a high detection performance. In particular, an error-free data transmission with a spectral efficiency of 0.33 bps/Hz is achieved at a distance of 105 km.

Chapter 5

DOA Tracking in Time-varying UWA Communication Channels

Contents

5.1 Introduction

In UWA channels, the communication link depends on the positions of the transmitter and the receiver relative to the acoustic propagation medium, and it is practically impossible to make the medium or the transmitter/receiver stationary, especially when the transmitter/receiver are attached to surface platforms. Ocean physical dynamics, from endless undulations of the sea surface to internal waves as well as tides and currents, cause the channel medium to vary and alter the propagation speed of sound, further strongly change the direction of arrival (DOA) of the received signals in time. Although the measurement of the ocean dynamics has been studied at length [116–124], it remains one of the most daunting challenges of UWA communications. In order to improve the performance of communication systems, it is required to adapt to the temporal instability during processing, i.e., keeping track of the dynamics.

The existing DOA estimation techniques [35, 40] are formulated for beamforming problems, in which the DOAs are assumed to be static. In real applications, the receivers (e.g., vertical linear array (VLA) of hydrophones) are in fact dynamic due to the drift oscillations of platforms (e.g., vessel) caused by surface waves [116–119]. Apart from the platform motion, internal wave-induced variations in sound speed are dominant cause of the acoustic scintillations in the ocean interior [120–124]. The acoustic scintillations of the received signal in the ocean interior from a source/transmitter can vary rapidly in amplitude, travel time, and the DOA [120]. Hence, it is desirable to take into account both the platform oscillation and the internal wave-induced fluctuation to use the acoustic DOA estimates.

DOA estimation is often used to analyse spatial signals in UWA channels [35, 38, 40, 41, 106]. The spatial analysis provides information for beamforming and producing directional signals [40, 41]. Often, the spread of received signals in space (DOA) and time (delay) is limited to a small number of clusters [35]. However, if several directions from the same space cluster is chosen, the receiver performance is limited due to correlation of the diversity branches. Chapter 4 reveals that the space-time clusters introduce a natural diversity, which can be used to improve the detection performance and reduce the complexity. Chapter 4 also proposes a low complexity time-frequency-time (TFT) beamforming technique to estimate DOAs and produce directional signals with static angles over a whole communication session. However, this TFT beamforming technique with static angles does not consider DOA fluctuation.

In this chapter, we investigate DOA fluctuation in UWA communication channels, and propose a beamforming technique that tracks DOAs. In the investigation, guard-free orthogonal frequency-division multiplexing (OFDM) signals [4, 60] are transmitted. The investigation is based on numerical simulation of signals received by a 14-element VLA experiencing angular oscillations. The simulation is done using the *Waymark* propagation channel model described in Chapter 2 at a distance of 80 km between the transmitter and receiver. We also use data from two sea trials at transmitter/receiver distances of 30 km and 105 km, with a transducer towed by a vessel moving at high speeds (8 m/s and 6 m/s, respectively). In the simulation and the two sea trials, with the proposed DOA tracking beamforming technique, the receiver shows an improved detection performance.

5.2 DOA Fluctuation in UWA Channels

In this section, we analyse time-varying DOAs in the sea trial at a distance of 105 km; we call it the F1-2 session. The acoustic environment is characterised by the sound speed profile (SSP) shown in Figure 3.11. In the sea trial, communication signals with a duration of 200 s were transmitted in the frequency interval 2560-3584 Hz; the distance between the transmitter and the receiver varied from 105 to 106 km, and the transmitter was towed by a vessel moving away from the receiver at a speed of 6 m/s. The depth of the transmitter was around 250 m, and a non-uniform receive VLA (with a length of 8.1 m) of 14 hydrophones was placed at a depth of around 420 m as shown in Figure 4.1. The inter spacing between the hydrophones differs from 0.3 to 1.2 m.

The space-time distribution of the received signal in the F1-2 session is shown in Figure 4.3(c). Spatial power distribution of the received signals is shown in Figure 5.1(a), from which two discrete space clusters can be seen. The two clusters provide two natural diversity branches in design of a receiver. Moreover, it can also be seen that within each cluster, the DOAs (angles) are time-varying. The DOA fluctuation in Figure 5.1(a) are tracked from the highest average power in each time step Δt ($\Delta t = 1$ s here), as shown in Figure 5.2(a).

In physical oceans, wind (surface) waves, with periods of a few seconds (up to about 20 s) [121, 122, 125], and internal waves, with periods from tens of minutes to many hours [120, 121] are two real phenomenons. In our case, specifically, the periods of the drifting platform induced by the surface waves are considered to be within 5-20 s, corresponding to a typical frequency spectrum (0.05-0.2 Hz) of surface waves [121, 122, 125]; the periods of the internal waves are considered to be more than 20 s, corresponding to a lower frequency interval of 0-0.05 Hz. Figure 5.2(b) shows that the period of the ocean surface waves is approximately $T_{sur} \approx 10$ s, while Figure 5.2(c) shows relatively slow DOA fluctuations.

To show the strength of linear relationship between the two DOA fluctuations in the high

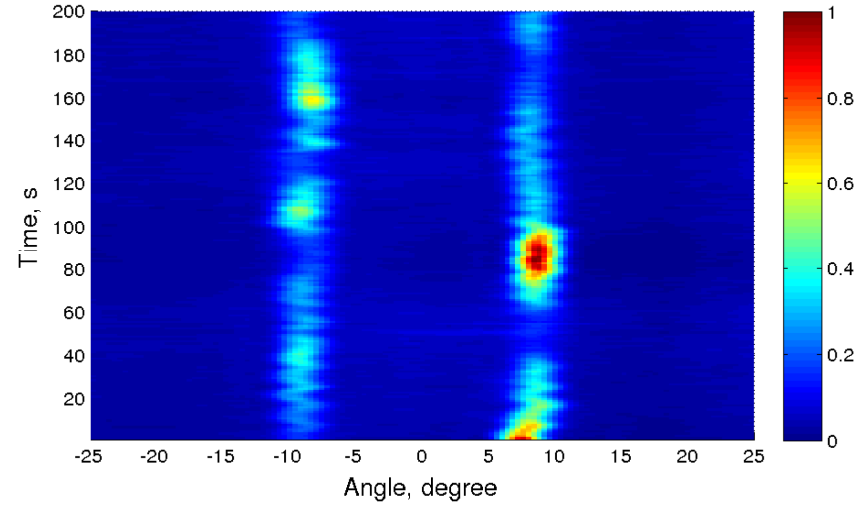

(a) Spatial power distribution in the F1-2 session; positive DOAs correspond to acoustic rays received from the sea surface direction while the negative DOAs show rays from the sea bottom direction.

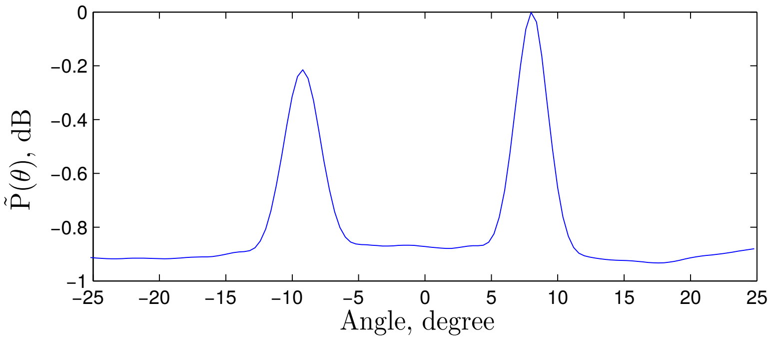

(b) The average spatial signal power $\tilde{\mathrm{P}}(\theta)$ obtained at an angle step of $0.1°$.

Figure 5.1: Spatial power in the F1-2 session.

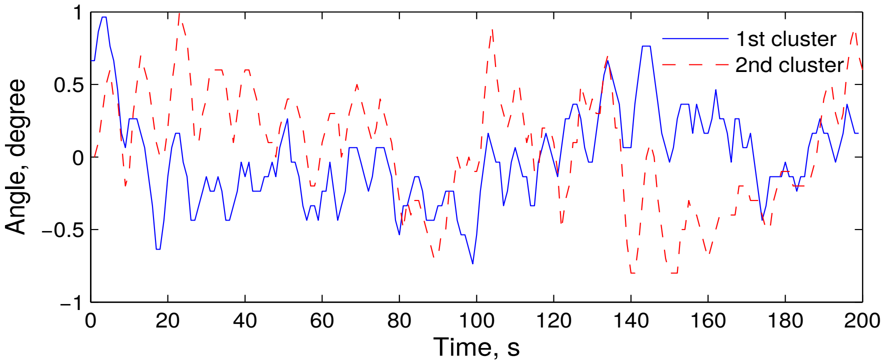

(a) Varying DOAs.

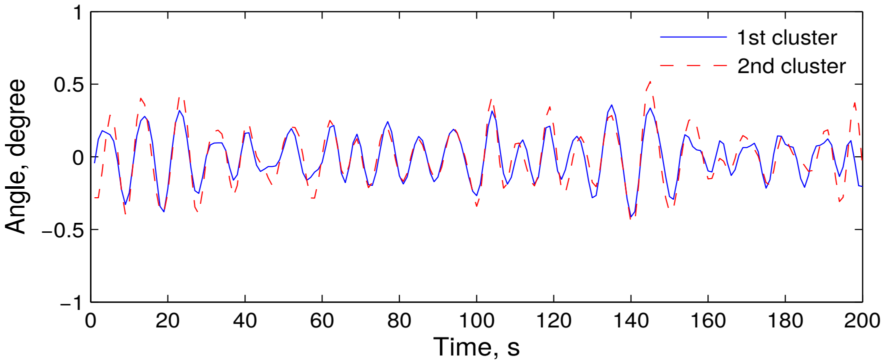

(b) DOA fluctuations in the frequency interval 0.05-0.2 Hz.

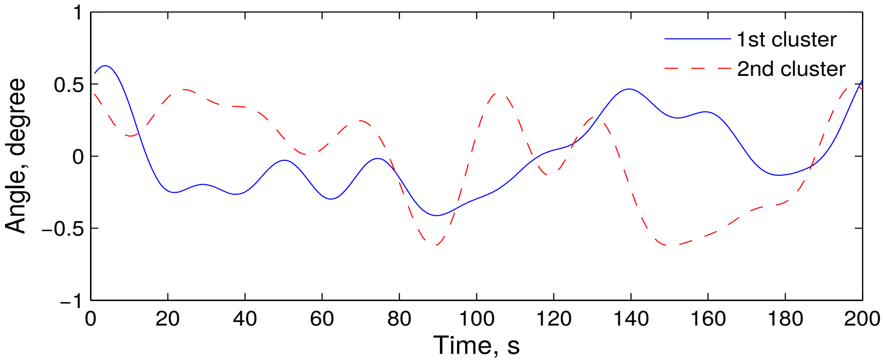

(c) DOA fluctuations in the frequency interval 0-0.05 Hz.

Figure 5.2: DOA fluctuations in the F1-2 session; 1st cluster: left in Figure 5.1(a); 2nd cluster: right in Figure 5.1(a).

and low frequency intervals, the Pearson correlation coefficient [126] is used as

$$\xi = \frac{\sum_{k=0}^{K-1} (\varphi_1(k\Delta t) - \bar{\varphi}_1)(\varphi_2(k\Delta t) - \bar{\varphi}_2)}{\sqrt{\sigma_1^2}\sqrt{\sigma_2^2}}, \tag{5.1}$$

where

$$\sigma_1^2 = \sum_{k=0}^{K-1} (\varphi_1(k\Delta t) - \bar{\varphi}_1)^2, \tag{5.2}$$

and

$$\sigma_2^2 = \sum_{k=0}^{K-1} (\varphi_2(k\Delta t) - \bar{\varphi}_2)^2, \tag{5.3}$$

are covariances of the two DOAs, $\Delta t = 1$ s is one frame duration of the transmitted signals (known as time step), $K = 200$, $\varphi_1(k\Delta t)$ and $\varphi_2(k\Delta t)$ are the two DOAs of the two space clusters at time instant $k\Delta t$, $\bar{\varphi}_1$ and $\bar{\varphi}_2$ are average DOA fluctuation of the two space clusters, respectively. As a result,

- The correlation coefficient for the relatively "high frequency" interval (0.05-0.2 Hz) is $\xi_h = 0.8725$. This shows a strong relationship between the two DOAs series of the two space clusters. In this session, the high wind speed (7-8 m/s) resulted in a complicated motion of the vessel connected with a receive VLA. The fluctuation of the VLA consequently induced fast DOA fluctuations in the frequency interval from 0.05 to 0.2 Hz.

- The correlation coefficient for the relatively "low frequency" interval (0-0.05 Hz) is $\xi_l = -0.0960$. This shows a weak relationship between the two DOA series of the two space clusters. During the communication session, propagation rays from the two space clusters experience two almost completely different medium in the channels, which results in the small correlation in the frequency interval from 0 to 0.05 Hz.

5.3 Transmitted Signal, Channel Model and Receiver

In this chapter, the transmitted signals are the same as that described in Section 3.4, the channel model is the same as that described in Section 4.3, and the receiver is the same as that described in Section 4.4 apart from techniques used in the spatial filter.

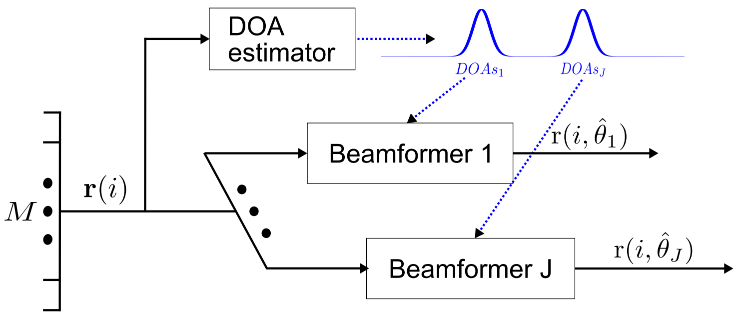

Figure 5.3: Block diagram of the spatial filter with J outputs based on J space clusters.

5.4 Beamforming Techniques in Spatial Filter

Figure 5.3 shows the block diagram of the spatial filter in the receiver. The DOA estimator computes the spatial power distribution to estimate DOAs. Then, the beamformers use these DOAs estimates to produce directional signals.

In the spatial filter, the following two beamforming techniques are considered:

- time-frequency-time beamforming technique with static DOA (TFT-SD) (Section 4.4.2);
- proposed time-frequency-time beamforming technique with DOA tracking (TFT-DT).

When describing the techniques below, for illustration, we will be using the sea trial data recorded in the F1-2 session.

5.4.1 Time-frequency-time beamforming with static DOA

The TFT-SD beamforming is modified from the beamforming described in Section 4.4.2, and the difference is that the TFT-SD beamforming considered in this chapter does not divide the frame into subframes. With the TFT-SD beamforming technique, J static DOAs (angles) are chosen from J space clusters for producing J directional signals.

The total power for all frequencies is shown in Figure 5.1(a). The average power over N_f frames is shown in Figure 5.1(b), obtained within the interval $\theta \in [-25°, 25°]$ with a step of $0.1°$.

In this chapter, the forgetting factor λ in (4.14) of the beamformer is different from that chosen in Section 4.4.2 and will be analysed in Sections 5.5 and 5.6.

5.4.2 Time-frequency-time beamforming with DOA tracking

We now describe the TFT-DT beamforming technique, in which J varying DOAs series are chosen from signal frames of J space clusters, to produce signal frames of J directional signals. Different from the TFT-SD beamforming, the TFT-DT beamforming chooses varying DOA series in a continuous communication session rather than a static DOA from each cluster for producing directional signal.

1. **DOA estimator**

   With (4.12), a peak detector $\mathbb{P}$ finds J local maxima of each frame $\mathrm{P}(i_f;\theta)$ from (4.11), which are considered to correspond to space clusters, as shown in Figure 5.1(a). With this technique, two ($J=2$) time-varying DOAs series are identified in the F1-2 session, as shown in Figure 5.2(a). In each cluster, varying DOAs series $\hat{\boldsymbol{\theta}}_j$ ($\hat{\boldsymbol{\theta}}_1 = [\hat{\theta}_{1,1},\ldots,\hat{\theta}_{1,N_f}]$ and $\hat{\boldsymbol{\theta}}_2 = [\hat{\theta}_{2,1},\ldots,\hat{\theta}_{2,N_f}]$) is chosen for further processing:

   $$[\hat{\theta}_{1,n_f},\hat{\theta}_{2,n_f}]^T = \mathbb{P}[\mathrm{P}(i_f;\theta)]. \tag{5.4}$$

   Note that in order to track the varying DOAs resulted from the dynamic ocean surface waves, we use Nyquist-Shannon sampling theorem [127] to set the time duration of one frame length $\Delta t \leqslant \frac{1}{2}T_{sur}$; in our experiments here, $\Delta t \leqslant 5$ s.

2. **Beamformer**

   For a chosen varying DOA series $\hat{\boldsymbol{\theta}}_j$, to cancel the interference arriving from other DOAs, the beamformer weight vector $\bar{\mathbf{w}}_{n_f}(\hat{\theta}_{j,n_f},k)$ in the n_fth frame is calculated as [112]:

   $$\bar{\mathbf{w}}_{n_f}(\hat{\theta}_{j,n_f},k) = \mathbf{Y}^{-1}(i_f;k)\mathbf{v}(\hat{\theta}_{j,n_f},k)\mathrm{P}_k(i_f;\hat{\theta}_{j,n_f}), \tag{5.5}$$

   where $\mathbf{Y}(i_f;k)$ is from (4.8), $\mathbf{v}(\hat{\theta}_{j,n_f},k)$ is from (4.9), and $\mathrm{P}_k(i_f;\hat{\theta}_{j,n_f})$ is from (4.10). The weight vector is smoothed in time:

   $$\mathbf{w}_{n_f}(\hat{\theta}_{j,n_f},k) \leftarrow \lambda\mathbf{w}_{n_f-1}(\hat{\theta}_{j,n_f-1},k) + (1-\lambda)\bar{\mathbf{w}}_{n_f}(\hat{\theta}_{j,n_f},k), \tag{5.6}$$

where $\mathbf{w}_0(\hat{\theta}_{j,n_f}, k) = \bar{\mathbf{w}}_1(\hat{\theta}_{j,n_f}, k)$. The directional signal is then computed as:

$$\mathrm{r}(i, \hat{\theta}_{j,n_f}) = \sum_{k=0}^{K-1} \mathbf{w}_{n_f}^H(\hat{\theta}_{j,n_f}, k)\mathbf{z}(i_f; k)e^{j\omega_k n/f_s}, \tag{5.7}$$

where $i = i_f + (n_f - 1)I_f + n$.

5.5 Numerical Results

To demonstrate the effectiveness of the proposed TFT-DT beamforming technique, we apply the technique to guard-free OFDM signals with superimposed data and pilot [4]. In a simulation with the *Waymark* propagation channel model described in Chapter 2, the transmitter is stationary at a depth of 300 m. The receive VLA is towed by an ocean surface platform, and has a periodic oscillation with a maximum oscillating angle of $\vartheta_M = 0.3°$. When the oscillating angle $\vartheta(t) = 0°$, the depth of the first hydrophone is 300 m, and the distance between the transmitter and the VLA is 80 km, as shown in Figure 5.4.

The VLA is the same as shown in Figure 4.1, and the SSP used in the simulation is as shown in Figure 3.11. During the simulation, 200 guard-free OFDM symbols are continuously transmitted. The signal-to-noise ratio (SNR) is set to 0 dB at receive hydrophones. The receive VLA oscillation is considered to be induced by the ocean surface waves, and the oscillating angle is given by

$$\vartheta(t) = -\vartheta_M \cos\left(\frac{2\pi t}{T_p}\right), \; t \in [0, T-1], \tag{5.8}$$

where $T_p = 10$ s is the period of the VLA oscillation, and $T = 200$ s the duration of the communication session, ignoring propagation time in the channel. Note that when the angle is on the left hand of the middle vertical line (see Figure 5.4), we set the $\vartheta(t)$ a negative value; vise versa.

In this simulation and in the sea trials described in Section 5.6 later on, when processing the received signals in the spatial filter, $K = 32$ frequencies are processed in the bandwidth of interest $F = 1024$ Hz, and the lowest frequency of interest $f_0 = \omega_0/(2\pi) = 2560$ Hz. The frame length I_f is considered to be one OFDM symbol length, and the loading factor $\kappa = 10^{-3}$. The

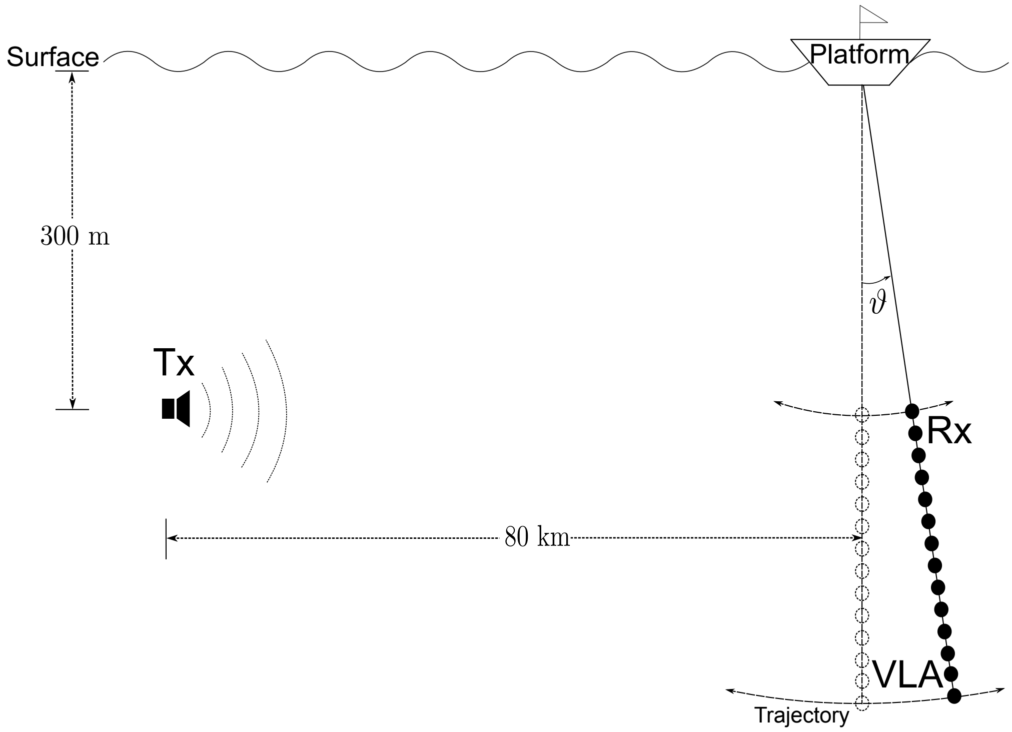

Figure 5.4: Simulation scenario with periodic oscillating receive VLA. Tx is the transmitter, and Rx is the receiver.

DOAs θ for DOA estimation are computed in the interval $[-25°, 25°]$ with a DOA step of $0.1°$.

Figure 5.5(a) shows spatial power distribution in this simulation. It can be seen that several (three) space clusters are identified, and the most outstanding cluster is the one with DOAs around $\theta = 12.5°$, which has much higher power than the other clusters (with angles of around $-5.5°$ and $2°$). It can also be seen that the DOAs in the outstanding cluster are time-varying but stationary. In the simulation, for simplicity, we only choose the outstanding cluster with the highest power to analyse.

Figure 5.5(b) shows the average spatial power $\tilde{\mathrm{P}}(\theta)$ in this simulation. With the peak detector $\mathbb{P}$, the angle corresponding to the highest power peak is $\hat{\theta}_j = 12.5°$ ($j = 1$ here), which is used to produce a single directional signal using the TFT-SD beamforming technique.

Figure 5.6 shows the VLA oscillating angle $\vartheta(t)$ (5.8) considered in the simulation and the estimated DOA fluctuation $\breve{\theta}(t)$ from the TFT-DT beamforming technique. The estimated

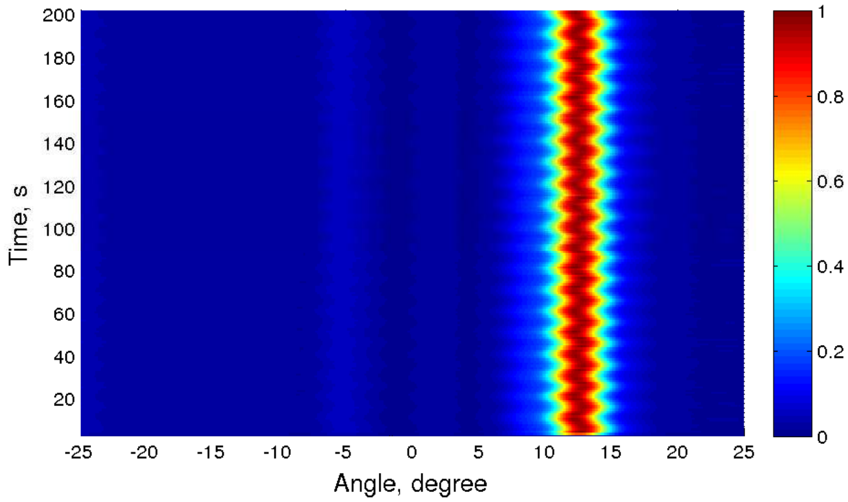

(a) Spatial power distribution.

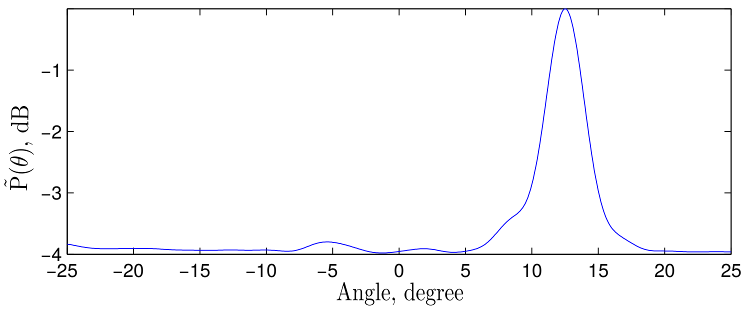

(b) The average spatial power $\tilde{\mathrm{P}}(\theta)$.

Figure 5.5: Spatial power in the simulation.

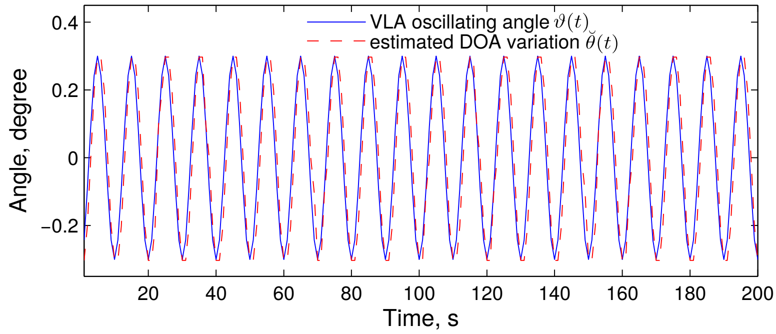

Figure 5.6: Comparison of the VLA oscillating angle $\vartheta(t)$ and the estimated DOA fluctuation $\breve{\theta}(t)$ in this simulation.

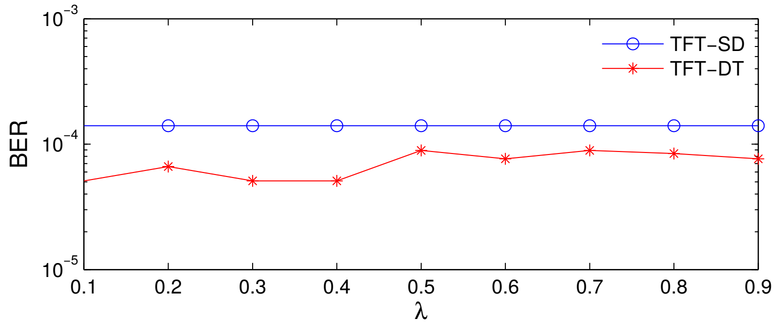

Figure 5.7: Coded BER performance of the receiver with the TFT-SD and the TFT-DT beamforming techniques in this simulation; the convolutional code described by the polynomial in octal [3 7].

DOA fluctuation $\breve{\theta}(t)$ is given by

$$\breve{\theta}(t) = \theta(t) - \bar{\theta}(t), \;\; t \in [0, T-1], \tag{5.9}$$

where $\theta(t)$ is the estimated DOA at time instant t, and $\bar{\theta}(t)$ is the average estimated DOA during a whole communication session. It can be seen that the VLA oscillating angle $\vartheta(t)$ and the estimated DOA fluctuation $\breve{\theta}(t)$ are almost coincide, including the amplitude and the period. Using (5.1) to compute the correlation coefficient of the VLA oscillating angle $\vartheta(t)$ and the estimated DOA fluctuation $\breve{\theta}(t)$, $\xi = 0.9518$ is obtained, which shows a strong relationship between the two variations.

We now analyse effects of the forgetting factor λ in the two beamforming techniques to the detection performance of the receiver. Figure 5.7 shows the bit error rate (BER) performance of the receiver with the TFT-SD and the TFT-DT beamforming techniques at a spectral efficiency of 0.5 bps/Hz; the convolutional code described by the polynomial in octal [3 7], being rate-1/2 code [104] is used.

It can be seen that the BER performance of the receiver with the TFT-SD beamforming does not change when the forgetting factor λ is increased from 0.1 to 0.9. The receiver with the TFT-DT beamforming outperforms that using the TFT-SD beamforming operating at forgetting factors λ varying from 0.1 to 0.9.

5.6 Sea Trial Results

Apart from the simulation data, data from two sea trials are also used to demonstrate the effectiveness of the proposed TFT-DT beamforming technique.

In this chapter, we consider two sea trial communication sessions. In one session, the distance between the transmitter and the receiver varied from 30 to 29 km, and the transmitter was towed by a vessel moving towards the receiver at a speed of 8 m/s; we call it the F1-1 session. In this session, 100 guard-free OFDM symbols were transmitted, and the space-time distribution of the received signals has been shown in Figure 4.2(a). In the F1-2 session, as described in Section 5.2, the distance between the transmitter and the receiver varied from 105 to 106 km, and the transmitter was towed by a vessel moving away from the receiver at a speed of 6 m/s. In the F1-2 session, 200 OFDM symbols were transmitted.

5.6.1 30 km between transmitter and receiver

In the F1-1 session, the high wind speed (7-8 m/s) resulted in a complicated motion of the vessel connected with a receive VLA. The motion indicates a fast DOA fluctuation (shown in Figure 5.8(b)) in the frequency interval between 0.05 and 0.2 Hz. In Figure 5.8(b), the period of the DOA fluctuation is approximately 10 s, which indicates a similar oscillation period as that shown in Figure 5.2(b). Figure 5.8(c) shows a slow DOA fluctuation in the frequency interval between 0 and 0.05 Hz. The ocean dynamics consequently resulted in a complicated DOA fluctuation of the received signals, shown in Figure 5.8(a) and Figure 5.9(a).

Figure 5.9(a) also shows the spatial power distribution in the F1-1 session. It can be seen that a space cluster with time-varying DOA around $\theta = -1.7°$, covers a range of angles from

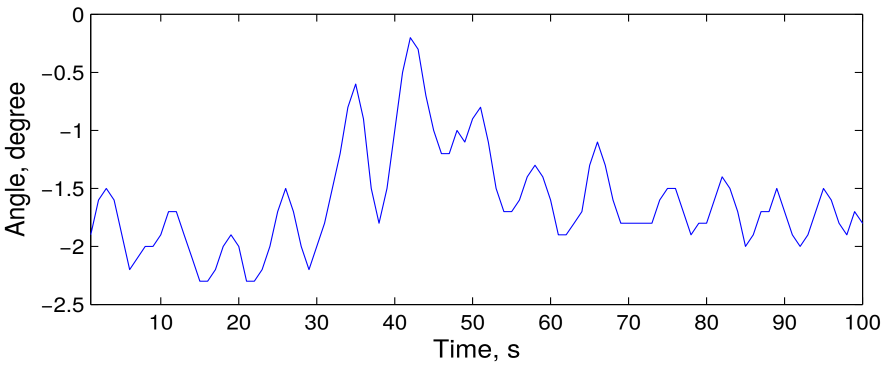

(a) Time-varying DOA.

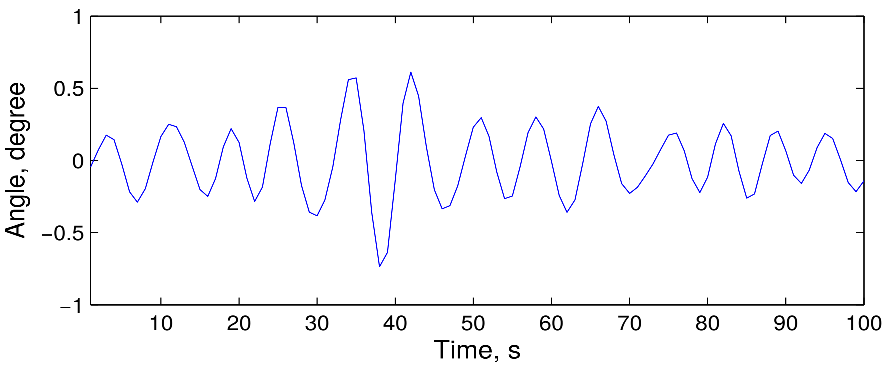

(b) DOA fluctuation in the frequency interval 0.05-0.2 Hz.

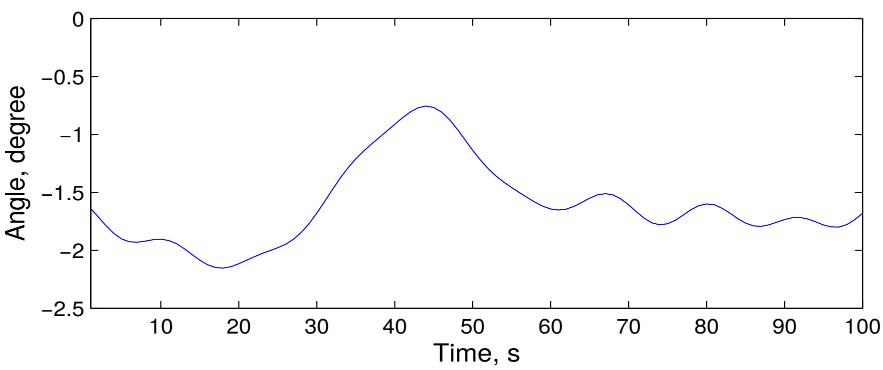

(c) DOA fluctuation in the frequency interval 0-0.05 Hz.

Figure 5.8: Time-varying DOAs in the F1-1 session.

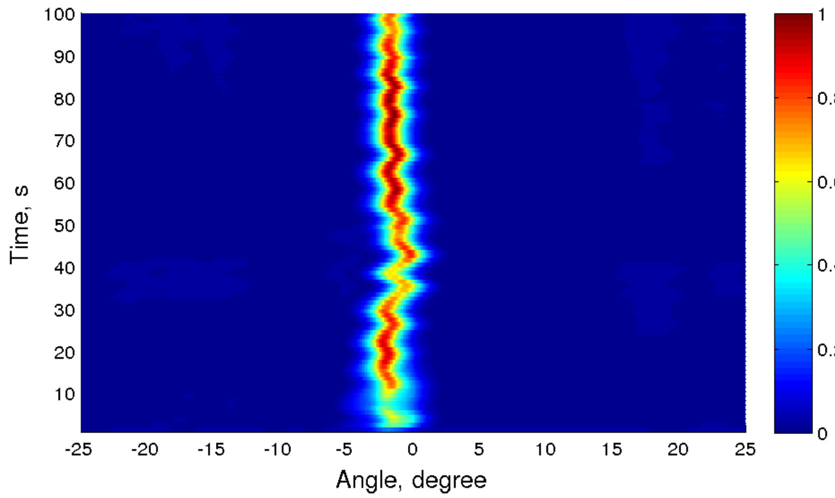

(a) Spatial power distribution.

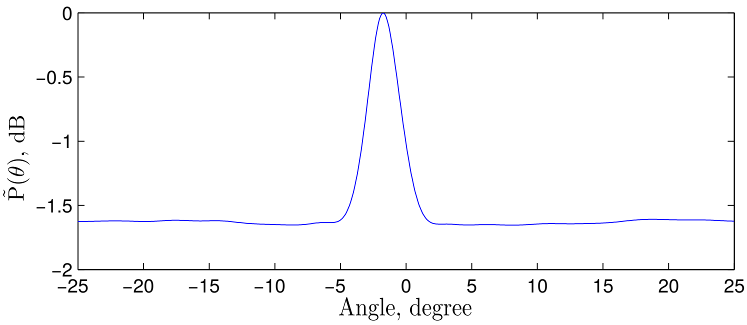

(b) The average spatial signal power $\tilde{\mathrm{P}}(\theta)$.

Figure 5.9: Spatial power in the F1-1 session.

$-4°$ to $1°$. Figure 5.9(b) shows the average spatial signal power $\tilde{\mathrm{P}}(\theta)$ in this session. The peak angle $\hat{\theta}_j = -1.7°$ ($j = 1$ here) is used to produce a single directional signal by the TFT-SD beamfoming. Figure 5.10 shows fluctuations of the channel impulse response over the F1-1 session at the first hydrophone.

We now compare BER performance of the receiver with the TFT-DT beamforming with that using the TFT-SD beamforming, when the forgetting factor λ varies from 0.1 to 0.9. Figure 5.12 presents the BER performance of the receiver applied to the sea trial data recorded in the F1-1 session at a spectral efficiency of 0.5 bps/Hz; the code represented by polynomial in octal [561 753], being rate-1/2 code [104] is used. The SNR in the F1-1 session (shown in Figure 5.11) is the result of the received signal energy divided by recorded noise energy in frames, which varies between -15 and -3 dB, and on average is -9 dB.

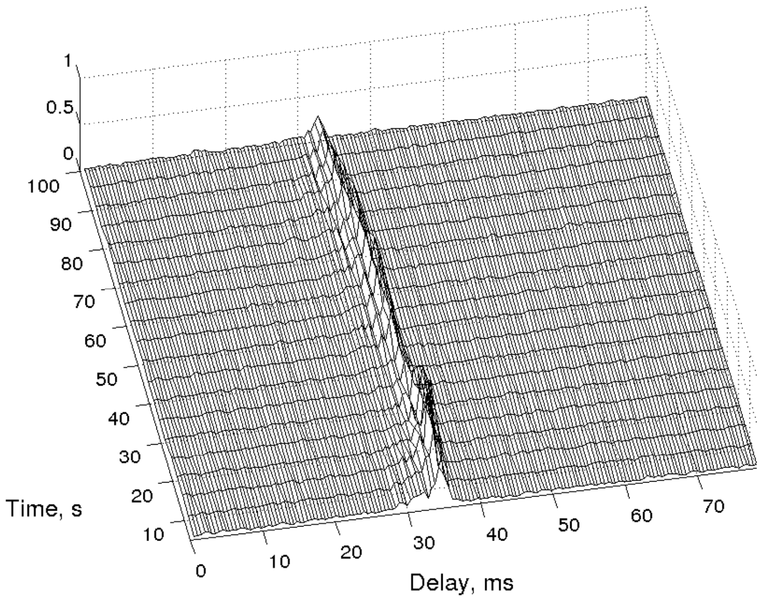

Figure 5.10: Fluctuations of the channel impulse response at the first hydrophone in the F1-1 session.

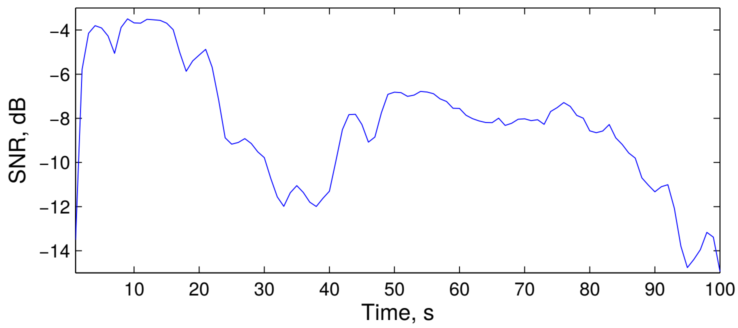

Figure 5.11: Time-varying SNR at the first hydrophone in the F1-1 session.

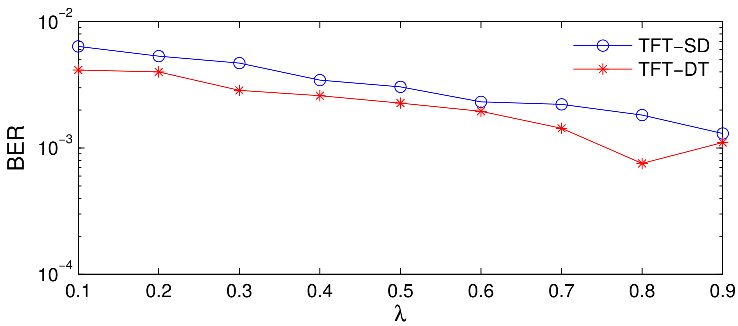

Figure 5.12: Coded BER performance of the receiver with the TFT-SD and the TFT-DT beamforming techniques in the F1-1 session; the code represented by polynomial in octal [561 753].

Results presented in Figure 5.12 demonstrate that the receiver with the TFT-DT beamforming outperforms that with the TFT-SD beamforming. When λ increases from 0.1 to 0.9, the receiver with the TDT-SD beamforming improves its detection performance. When λ increases from 0.1 to 0.8, the detection performance of the receiver with the TDT-DT beamforming is improved; and when $\lambda = 0.8$, the receiver with the TFT-DT beamforming achieves the best performance. However, with further increase in the forgetting factor to $\lambda = 0.9$, the receiver with the TFT-DT beamforming shows a degradation in the performance, but the performance is still better than that of the TFT-SD beamforming.

5.6.2 105 km between transmitter and receiver

In the F1-2 session, as described in Section 5.2, the distance between the transmitter and the receive VLA was 105 km at the beginning of the communication session. The SNR on a single hydrophone during the communication session is shown in Figure 4.11, with an average of -0.3 dB. Figure 4.12(a) shows fluctuations of the channel impulse response over the F1-2 session at the first hydrophone; there can be seen four discrete multipaths. We consider two signals, from directions $\hat{\theta}_1 = 8.4°$ and $\hat{\theta}_2 = -9°$; fluctuations of channel impulse responses for these directions are shown in Figure 4.12(b) and Figure 4.12(c), respectively. It can be seen that the four multipaths are now split between the two directions.

We now analyse the effects of the forgetting factor λ in the two beamforming techniques to the detection performance of the receiver. Figure 5.13 shows BER performance of the receiver at a spectral efficiency of 0.33 bps/Hz; the code represented by polynomial in octal [5 7 7], being rate-1/3 code [104] is used.

It can be seen that the performance of the receiver with the TFT-SD beamforming is improved when the forgetting factor λ is increased from 0.1 to 0.5, and achieves the best performance at $\lambda = 0.8$ and 0.9; the performance of the receiver with the TFT-DT beamforming is improved when the forgetting factor λ is increased from 0.1 to 0.8, and achieves the best performance at $\lambda = 0.8$. The receiver with the TFT-DT beamforming performs better than that with the TFT-SD beamforming.

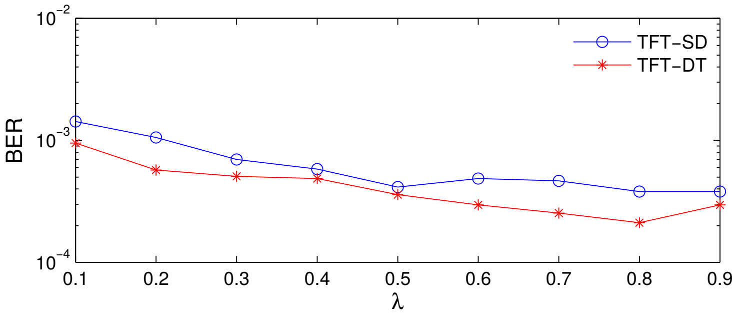

Figure 5.13: Coded BER performance of the receiver with the TFT-SD and the TFT-DT beamforming techniques in the F1-2 session; the code represented by polynomial in octal [5 7 7].

5.7 Summary

In this chapter, the acoustic DOA fluctuation in time-varying UWA communication channels is illustrated, and a receiver that exploits the DOA tracking is investigated. The DOA fluctuation of the received signals is resulted from the ocean surface and internal waves. The investigated receiver is designed for an UWA communication system with the transmission of guard-free OFDM signals with superimposed pilot symbols. In the receiver, the beamforming with DOA tracking is proposed, and compared with the beamforming without DOA tracking in the simulation and the two sea trials. The results show that the beamforming with DOA tracking outperforms the beamforming without DOA tracking.

Chapter 6

RLS Adaptive Filters for Estimation of Sparse UWA Channels

Contents

6.1 Introduction

The impulse response of an UWA channel is often sparse [17]. To identify the channel, sparse adaptive filters are used [33]. A high identification performance of the channel estimation is very important for improving the detection performance of a receiver. In a receiver of a high date rate communication system, signals are often processed using a linear equalizer whose weights are calculated based on accurate channel estimates [31]. However, the channel estimation is challenging due to a large delay spread and fast time-variation of the acoustic channel. For obtaining a good channel estimation performance, adaptive algorithms have been employed extensively [12], e.g., the least mean squares (LMS) algorithm, and classic recursive least squares (RLS) algorithms [128–132] are used. However, the LMS algorithm has a slow convergence [32], and these RLS algorithms have relatively high complexity [$\mathcal{O}(N^2)$

arithmetic operations, where N is the filter length] and lower performance compared to sparse RLS adaptive filters [32, 133].

For improving the performance, sparse adaptive filters were proposed [32, 33, 133]. In UWA channels, the impulse response spreads over delay areas where most of magnitudes are close to zero, which makes the channel sparse [17]. To reduce the complexity, dichotomous coordinate descent (DCD) iterations are used [133], making the filter complexity only linear in the filter length. In sparse adaptive filters, *a priori* information on the channel is incorporated into the adaptive algorithm to improve their performance. By taking into account the sparseness of the channel impulse response as an inherent property of the underwater acoustic propagation, adaptive filters can significantly improve the performance of channel estimation [17, 32, 34].

In this chapter, we investigate normalized LMS (NLMS) adaptive filter and sparse RLS adaptive filters [131] in UWA channels and propose two new sliding-window RLS adaptive filters, which are: (1) sliding-window RLS adaptive filter with diagonal loading; and (2) sliding-window RLS homotopy adaptive filter, to improve the detection performance of a receiver of guard-free orthogonal frequency-division multiplexing (OFDM) signals with superimposed pilot symbols [4].

In [133], the convergence of exponential-window in adaptive filters was compared with that of a sliding-window, and the comparison results showed that the sliding-window provides a faster convergence to the steady-state. The first proposed sliding-window RLS adaptive filter with diagonal loading is exploited in a channel estimator of the receiver. The proposed adaptive filter is based on sliding-window, diagonal loading, and DCD iterations [134, 135]. We investigate and compare performance of the receiver with the first proposed sliding-window RLS adaptive filter with diagonal loading and existing adaptive filters. More specifically, we consider: NLMS adaptive filter; exponential-window and sliding-window classic RLS adaptive filters [131, 132]; exponential-window and sliding-window RLS adaptive filters with penalties [133]; exponential-window RLS adaptive filter with diagonal loading [32]; and the proposed sliding-window RLS adaptive filter with diagonal loading. The comparison has been done using signals recorded in a sea trial at a distance of 80 km with a transducer moved at a speed of 6 m/s. In these conditions, with the first proposed sliding-window RLS adaptive filter with diagonal loading, the receiver demonstrates the best performance, whereas the complexity of the first proposed sliding-window RLS adaptive filter with diagonal loading is only linear in the filter length.

In [136], an exponential-window homotopy RLS-DCD adaptive filter possessing a high performance and low complexity was proposed. Here, we propose a sliding-window homotopy RLS-DCD algorithm and investigate it in application to estimation of sparse UWA channels. The second proposed sliding-window RLS homotopy algorithm has the same structure as the exponential-window homotopy RLS-DCD algorithm. The proposed homotopy algorithm is used for channel estimation in an UWA communication system. In the transmitter of the system, the guard-free orthogonal frequency-division multiplexing (OFDM) signals with superimposed pilot signals are transmitted. We investigate and compare performance of the receiver with five adaptive filters: NLMS adaptive filter; exponential-window and sliding-window classic RLS adaptive filters [128]; the exponential-window homotopy RLS-DCD adaptive filter [136]; and the second proposed sliding-window homotopy RLS-DCD adaptive filter. The comparison is done using signals recorded on a 14-element vertical linear antenna array (VLA) in a sea trial at a distance of 105 km with a transducer moved at a speed of 6 m/s. The proposed adaptive filter provides an improved performance and error-free transmission at a spectral efficiency of 0.33 bps/Hz.

6.2 Sparse System Identification

We consider adaptive filters with the task of finding a complex-valued $N \times 1$ vector $\mathbf{h}(n)$ that, at every time instant n, minimizes the cost function

$$\bar{J}[\mathbf{h}(n)] = \bar{f}_{\mathrm{LS}}[\mathbf{h}(n)] + f[\mathbf{h}(n)], \tag{6.1}$$

where $\bar{f}_{\mathrm{LS}}[\mathbf{h}(n)]$ is the least square (LS) error of the solution $\mathbf{h}(n)$ and $f[\mathbf{h}(n)]$ is a penalty function that incorporates *a priori* information on the sparse solution [133].

Let complex-valued $\mathbf{x}(n)$ and $d(n)$ be an $N \times 1$ regressor vector and desired signal, respectively, at time instant n. We denote

$$\mathbf{X}(n) = \begin{pmatrix} \mathbf{x}^H(1) \\ \vdots \\ \mathbf{x}^H(n) \end{pmatrix} \quad \text{and} \quad \mathbf{d}(n) = \begin{pmatrix} d^*(1) \\ \vdots \\ d^*(n) \end{pmatrix} \tag{6.2}$$

the $n \times N$ matrix of the regressor data and $n \times 1$ vector of the desired signal, respectively. In many adaptive filtering scenarios, $\bar{f}_{\text{LS}}[\mathbf{h}(n)]$ can be expressed as [137, 138]:

$$\bar{f}_{\text{LS}}[\mathbf{h}(n)] = \frac{1}{2}\mathbf{d}^H(n)\mathbf{D}(n)\mathbf{d}(n) + f_{\text{LS}}[\mathbf{h}(n)], \tag{6.3}$$

where $f_{\text{LS}}[\mathbf{h}(n)] = \frac{1}{2}\mathbf{h}^H(n)\mathbf{R}(n)\mathbf{h}(n) - \Re\{\mathbf{h}^H(n)\mathbf{b}(n)\}$, $\mathbf{R}(n) = \mathbf{X}^H(n)\mathbf{D}(n)\mathbf{X}(n)$ and $\mathbf{b}(n) = \mathbf{X}^H(n)\mathbf{D}(n)\mathbf{d}(n)$.

There are two important cases of the matrix $\mathbf{D}(n)$. The first one is when an exponential-window is used for computing the matrix $\mathbf{R}(n)$ and vector $\mathbf{b}(n)$, similarly to what is done in the classic exponential-window RLS algorithm [131, 132]. In this case, we have

$$\mathbf{D}(n) = \text{diag}[\lambda^{n-1}, \lambda^{n-2}, \ldots, \lambda, 1], \tag{6.4}$$

where λ is the forgetting factor, $\lambda \in (0, 1]$. The other one is when a sliding-window is used, in which case we have

$$\mathbf{D}(n) = \begin{pmatrix} \mathbf{0}_{(n-M)\times(n-M)} & \mathbf{0}_{(n-M)\times M} \\ \mathbf{0}_{M\times M} & \mathbf{I}_M \end{pmatrix}, \tag{6.5}$$

where M is the length of the sliding-window [133] and $\mathbf{I}_M$ is an $M \times M$ identity matrix.

These two matrices $\mathbf{D}(n)$ are considered below in eight adaptive filters, which are: exponential-window and sliding-window classic RLS adaptive filters; exponential-window and sliding-window RLS adaptive filters with penalties; exponential-window RLS adaptive filter with diagonal loading; the first proposed sliding-window RLS adaptive filter with diagonal loading; exponential-window homotopy RLS adaptive filter; and the second proposed sliding-window homotopy RLS adaptive filter.

6.3 Sliding-window Adaptive Filter with Diagonal Loading

6.3.1 Adaptive filters

In this section, we describe seven adaptive filters as follows.

1. **NLMS adaptive filters**

   In the case of NLMS adaptive filter, we have the following recursions for updating the impulse response $\mathbf{h}(n)$ of the input signal $\mathbf{x}(n) = [x(n), x(n-1), \ldots, x(n-N+1)]^T$ [139]:

$$\mathbf{h}(n) = \mathbf{h}(n-1) + \frac{\mu}{\varepsilon + ||\mathbf{x}(n)||^2} e(n)\mathbf{x}(n), \tag{6.6}$$

   where the adaptation constant μ satisfies the condition $1 < \mu < 2$ to make the NLMS algorithm convergent in the mean square, and the small regularization value ε satisfies the condition $\varepsilon > 0$ to avoid numerical instability. The initial $\mathbf{h}(n) = \mathbf{0}$. The error $e(n)$ at the time instant n is given by:

$$e(n) = d(n) - \mathbf{x}^T(n)\mathbf{h}(n-1), \tag{6.7}$$

   where $d(n)$ is the desired response. The NLMS algorithm can be viewed as a LMS algorithm with a time-varying step size $\mu(n) = \mu/(\varepsilon + ||\mathbf{x}(n)||^2)$, solving a gradient noise amplification problem in LMS algorithm.

2. **Exponential-window and sliding-window classic RLS adaptive filters**

   In the case of the classic exponential-window RLS adaptive filter, we have the following recursions for updating the correlation matrix $\mathbf{R}(n)$ of the input signal $\mathbf{x}(n) = [x(n), x(n-1), \ldots, x(n-N+1)]^T$ and vector $\mathbf{b}(n)$ [131, 132]:

$$\mathbf{R}(n) = \lambda\mathbf{R}(n-1) + \mathbf{x}(n)\mathbf{x}^H(n), \tag{6.8}$$

$$\mathbf{b}(n) = \lambda\mathbf{b}(n-1) + d^*(n)\mathbf{x}(n). \tag{6.9}$$

   In the case of the classic sliding-window RLS adaptive filter, we have the recursions for updating the matrix $\mathbf{R}(n)$ and vector $\mathbf{b}(n)$ are given by

$$\mathbf{R}(n) = \mathbf{R}(n-1) + \mathbf{x}(n)\mathbf{x}^H(n) - \mathbf{x}(n-M)\mathbf{x}^H(n-M), \tag{6.10}$$

$$\mathbf{b}(n) = \mathbf{b}(n-1) + d^*(n)\mathbf{x}(n) - d^*(n-M)\mathbf{x}^H(n-M). \tag{6.11}$$

In the classic RLS adaptive filters, the penalty term in (6.1) is zero, i.e., $f[\mathbf{h}(n)] = 0$. The solution to the optimization problem at every instant n can be found as a solution to the system of equation

$$\mathbf{R}(n)\mathbf{h}(n) = \mathbf{b}(n). \tag{6.12}$$

The complexity of solving this system directly is $\mathcal{O}(N^3)$. When recursions (6.8) and (6.10) are considered, the complexity can be reduced to $\mathcal{O}(N^2)$. However, we can use DCD iterations to further reduce the complexity to $\mathcal{O}(N)$ (see Table 6.2 below). When using DCD iterations, elements of the solution vector are represented in a fixed-point format with M_b bits within an amplitude interval [-H, H]. The DCD iterations start updating the most significant bits of the solution, proceeding towards less significant bits. This is controlled by a step-size $\delta > 0$ that starts with $\delta = H$ and is reduced as $\delta \leftarrow \delta/2$ for less significant bits; see [135] for more details.

3. **Exponential-window and sliding-window RLS adaptive filters with penalties**

   In sparse RLS adaptive filters with penalties [133], the penalty is often given by

$$f[\mathbf{h}(n)] = \tau||\mathbf{h}(n)||_p, \tag{6.13}$$

   where $||\mathbf{h}(n)||_p$ is a p-norm, and $\tau > 0$ is a regularization parameter that controls a balance between the LS fitting and the penalty. In the two adaptive filters with penalties, we consider the case of $p = 1$, which means that the penalty is the lasso penalty [133]. With the lasso penalty, the adaptive filter solves the minimization problem in (6.1) at every time instant n with DCD iterations.

4. **Exponential-window RLS adaptive filter with diagonal loading**

   In this sparse RLS adaptive filter [32], the penalty functions from (6.13) are used. The solution to the optimization problem at every instant n is found as a solution to the system of equations

$$\{\mathbf{R}(n) + \mathbf{W}(n)\}\mathbf{h}(n) = \mathbf{b}(n), \ n > 0, \tag{6.14}$$

where the diagonal matrix $\mathbf{W}(n) = \mathrm{diag}\{\mathbf{w}(n)\}$ depends on $\hat{\mathbf{h}}(n-1)$, and $\hat{\mathbf{h}}(n-1)$ is an estimate of the impulse response $\mathbf{h}(n-1)$. Then, the DCD algorithm is applied to iteratively solve the system (6.14) by reusing the solution found at the previous instant $n-1$ as a warm-start for the solution at time instant n.

As estimate $\hat{\mathbf{h}}(n)$ of the solution $\mathbf{h}(n)$ to the system in (6.14) is found as

$$\hat{\mathbf{h}}(n) = \hat{\mathbf{h}}(n-1) + \Delta\hat{\mathbf{h}}, \tag{6.15}$$

where $\Delta\hat{\mathbf{h}}$ is an estimate of the solution $\Delta\mathbf{h}$ of the system

$$[\mathbf{R}(n) + \mathbf{W}(n)]\Delta\mathbf{h} = \mathbf{c}(n|n-1), \tag{6.16}$$

where

$$\mathbf{c}(n|n-1) = \lambda\mathbf{c}(n-1|n-1) + e^*(n)\mathbf{x}(n) - [\mathbf{W}(n) - \mathbf{W}(n-1)]\hat{\mathbf{h}}(n-1), \tag{6.17}$$

$$\mathbf{c}(n|n) = \mathbf{c}(n|n-1) - [\mathbf{R}(n) + \mathbf{W}(n)]\Delta\hat{\mathbf{h}}, \tag{6.18}$$

$e(n) = d(n) - y(n)$ is the *a priori* estimation error, and $y(n) = \hat{\mathbf{h}}^H(n-1)\mathbf{x}(n)$ is the adaptive filter output at time instant n.

We consider here the case $p = 0$ in (6.13) and the weights of diagonal matrix $\mathbf{W}(n)$ are correspondingly given by [32]

$$w_i(n) = \frac{\tau}{|\hat{h}_i(n-1)|^2 + \epsilon}, \tag{6.19}$$

where $\epsilon > 0$ and $\tau > 0$ are adjusted parameters. When $|\hat{h}_i(n-1)|$ is close to zero, we have the diagonal loading entry $\tau w_i(n) \approx \tau/\epsilon$. Thus the ratio τ/ϵ should be high enough to almost remove (zero) the element $h_i(n)$ from the solution. However, when $|\hat{h}_i(n-1)|$ is close to a maximum value $h_{\max} = \max_i |h_i|$, we should have $\epsilon \ll h_{\max}^2$ to avoid degradation in the estimation accuracy. The parameter τ should also relate to the noise level: the higher is the noise level the higher should be τ.

Table 6.1: Sliding-window RLS adaptive filter with diagonal loading

	Input parameters: M, M_b, N_u, $\epsilon > 0$, $\tau > 0$ Output: $\hat{\mathbf{h}}(n) = \mathbf{h}, \mathbf{c}(n\|n) = \mathbf{c}$
Step	Initialization: for $n \leq 0$: $\mathbf{x}(n) = \mathbf{0}_L, \hat{\mathbf{h}}(0) = \mathbf{0}_L, \mathbf{c}(0\|0) = \mathbf{0}_L, \mathbf{R}(0) = \eta \mathbf{I}_L$, $\eta > 0$, $\mathbf{I}_L$ is the identity matrix
	for $n = 1, 2, \ldots$
1	Update: $\mathbf{R}(n) = \mathbf{R}(n-1) + \mathbf{x}(n)\mathbf{x}^H(n) - \mathbf{x}(n-M)\mathbf{x}^H(n-M)$
2	Filter output: $y(n) = \hat{\mathbf{h}}^H(n-1)\mathbf{x}(n)$
3	Error: $e(n) = d(n) - y(n)$
4	Filter delayed output: $y_M(n) = \hat{\mathbf{h}}^H(n-1)\mathbf{x}(n-M)$
5	Delayed error: $e_M(n) = d(n-M) - y_M(n)$
6	$\mathbf{c}(n\|n-1) = \mathbf{c}(n-1\|n-1) + e^*(n)\mathbf{x}(n) - e_M^*(n)\mathbf{x}(n-M)$ $-[\mathbf{W}(n) - \mathbf{W}(n-1)]\hat{\mathbf{h}}(n-1)$
7	Use DCD approximately solve: $[\mathbf{R}(n) + \mathbf{W}(n)]\Delta\mathbf{h} = \mathbf{c}(n\|n-1)$ to obtain a solution $\Delta\hat{\mathbf{h}}$ and $\mathbf{c}(n\|n) = \mathbf{c}(n\|n-1) - [\mathbf{R}(n) + \mathbf{W}(n)]\Delta\hat{\mathbf{h}}$ and update $\hat{\mathbf{h}}(n) = \hat{\mathbf{h}}(n-1) + \Delta\hat{\mathbf{h}}$
8	Update the diagonal matrix $\mathbf{W}(n)$

5. **Sliding-window RLS adaptive filter with diagonal loading**

   In this sparse RLS adaptive filter, the correlation matrix $\mathbf{R}(n)$ is recursively updated as in (6.10). The penalty functions from (6.13) are used. The solution to the optimization problem with the cost function (6.1) at every time instant n is then found by solving the linear system in (6.14).

   Table 6.1 shows the algorithm of the sliding-window RLS adaptive filter with diagonal loading, where M_b is the number of bits used for representation of filter entries in the solution vector and N_u is the number of DCD iterations per sample. The parameter M_b defines the accuracy of the fixed-point representation, whereas the parameter N_u limits the complexity.

6.3.2 Signal processing in the receiver

In this section, the transmitted signals are the same as that described in Section 3.4, and the receiver and adaptive filters are described below.

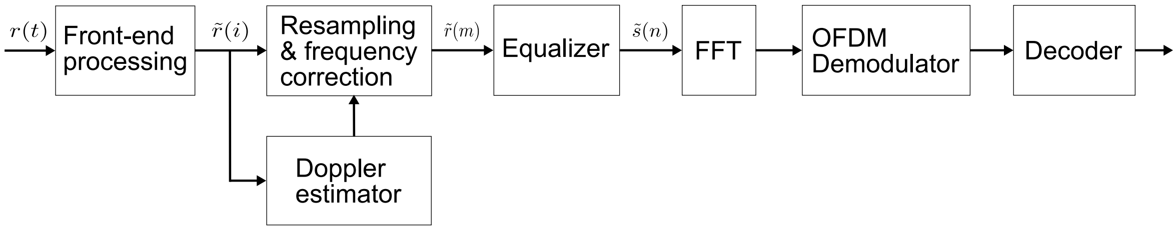

Figure 6.1: Block diagram of the receiver of guard-free OFDM signal.

1. **Receiver**

   The block diagram of the receiver is shown in Figure 6.1. It contains a block of front-end processing, Doppler estimator, block of resampling and frequency correction, equalizer, OFDM demodulator and decoder.

   In the front-end processing block, the received signal $r(t)$ is bandpass filtered, converted into the digital form, down-shifted, and low-pass filtered to produce the baseband digital signal $\tilde{r}(i)$.

   In the Doppler estimator, the time-varying dominant Doppler scale factor is estimated. The estimate is obtained by computing multiple sections of the cross-ambiguity function between the received and superimposed pilot signals on the *delay-Doppler scale* grid and finding the position of its peak [26, 57, 115]. The estimate is further rectified using a fine estimator that interpolates the peak. The discrete-time estimates of the Doppler scale factor are linearly interpolated and used to compensate for the dominant time-varying Doppler compression by resampling the signal $\tilde{r}(i)$ with the interpolated scale factor (see [4] for more details).

   The resampled signal $\tilde{r}(n)$ is applied to a time-domain linear equalizer. The equalized and combined signal $\tilde{s}(n)$ is transferred to a demodulator for symbol decision, and further to a decoder. Soft-decision Viterbi decoding [104] is applied to the recovered symbols.

2. **Equalizer**

   Figure 6.2 shows the block diagram of a single branch of the equalizer. The equalizer contains two branches: one dealing with even samples of $\tilde{r}(n)$, and the other dealing

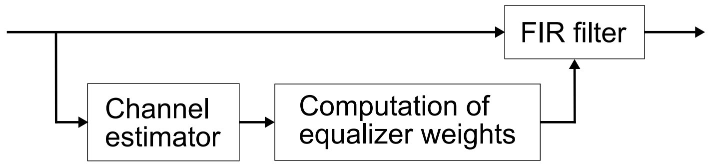

Figure 6.2: Block diagram of a single branch of the equalizer [4] (for convenience, we show Figure 3.5 again).

with odd samples of $\tilde{r}(n)$. The outputs of the equalizers are summed to produce the signal $\tilde{s}(n)$. The equalizer is implemented using the channel-estimate-based FIR scheme with a channel estimator based on an RLS adaptive filter [31, 43]. The linear equalizer compensates for scale factors of different multipath components and combines these components. The channel estimates are transformed into spline coefficients for the impulse response of the equalizer FIR filter to trace the time-varying channel fluctuations (see [4, 31] for details). Note that the bandpass signals, such as $\tilde{r}(n)$ and $\tilde{s}(n)$ are complex valued. Therefore, the adaptive filter should also be complex valued.

6.3.3 Sea trial results

In order to test the effectiveness of the proposed adaptive filter in an UWA channel, we applied the NLMS adaptive filter and the six RLS adaptive filters discussed in Section 6.3.1 to channel estimation in the receiver. In the sea trial, 376 OFDM symbols were continuously transmitted at a carrier frequency of 3072 Hz and with a bandwidth of 1024 Hz. The acoustic transducer was towed at a depth of 200 m by a vessel moved towards the receiver at a velocity of 6 m/s. The receiver was placed at a depth of 400 m. At the start of transmission, the distance between the transducer and receiver was 80 km. The SNR for the received signal in this session is shown in Figure 6.3. The average SNR during the session is about 11 dB. Figure 6.4 shows fluctuations of the channel impulse response in the sea trial. There can be seen fast variations of the channel delays and amplitudes that make the channel estimation and equalization a very challenging problem. As described in Section 3.4.2, the Doppler variation rate mainly depends on the acceleration of the transmitter/receiver, and the highest rate which can be tracked is $(2N_d + 1)\Delta f$.

In the NLMS adaptive filter, the adaptation constant μ is set to 0.1, and the regularization value ε is set to 10^{-3}. In the exponential-window adaptive filters, the forgetting factor is set to $\lambda = 0.998$, which satisfies $\lambda > 1 - 2/N$ [132], where $N = 176$ (with a sampling interval of

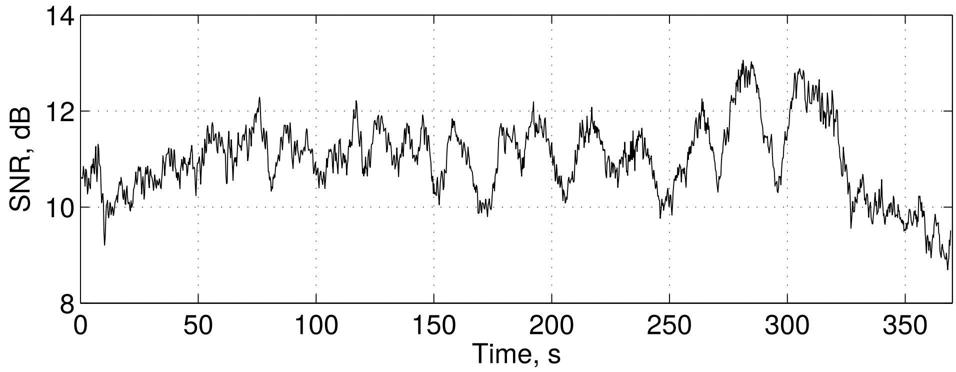

Figure 6.3: Time-varying SNR in the F1-10 sea trial; for convenience, Figure 3.12 is shown again.

Table 6.2: Performance of the receiver with various RLS adaptive filters and complexity of the adaptive filters.

Adaptive filters used in the receivers	**BER**	**Complexity** (multiplications)
NLMS	4.2×10^{-2}	$2N$
Classic RLS (Exponential-window)	8.1×10^{-4}	$3N^2$ $(3N)$
Classic RLS (Sliding-window)	2.2×10^{-4}	$5N^2$ $(5N)$
Penalties (Exponential-window)	1.1×10^{-4}	$7N$
Penalties (Sliding-window)	6.6×10^{-5}	$10N$
Diagonal loading (Exponential-window)	7.2×10^{-5}	$4N$
Diagonal loading (Sliding-window)	3.9×10^{-5}	$7N$

1 ms) is the filter length. The length of the sliding-window $M = 1024$ is chosen to obtain the best performance. In sparse RLS adaptive filters, the number of bits used for representation of filter entries is set to $M_b = 12$, the number of DCD iterations $N_u = 14$, the regularization parameter $\tau = 3 \times 10^{-4}$, and $\epsilon = 10^{-3}$. Table 6.2 shows BER performance of the receiver with various adaptive filters and complexity of the adaptive filters in terms of complex-valued multiplications per sample.

From Table 6.2, we observe that the NLMS adaptive filter shows the worst performance among these adaptive filters and requires the least complexity. In all other cases, compared to the exponential-window, the sliding-window results in a better detection performance of the receiver, but comes with a somewhat higher complexity. When DCD iterations are used, the complexity of the classic RLS adaptive filters reduces from $\mathcal{O}(N^2)$ to $\mathcal{O}(N)$. The RLS adaptive filter with penalties results in smaller BER and complexity than the classic RLS adaptive filters. However, the adaptive filter with diagonal loading allows even better performance and

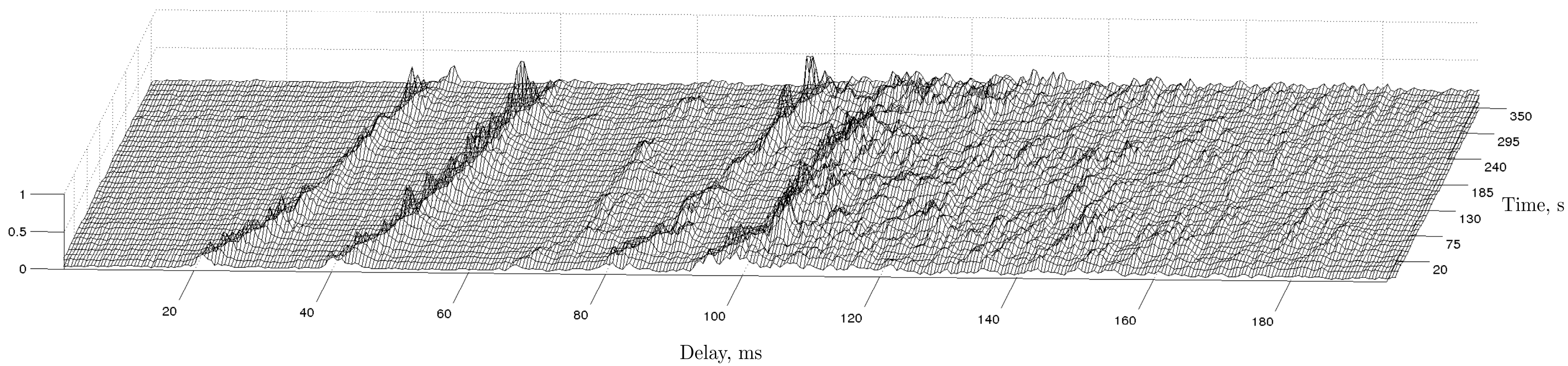

Figure 6.4: Fluctuations of the channel impulse response in the sea trial; (Figure 3.10(b) in a different view).

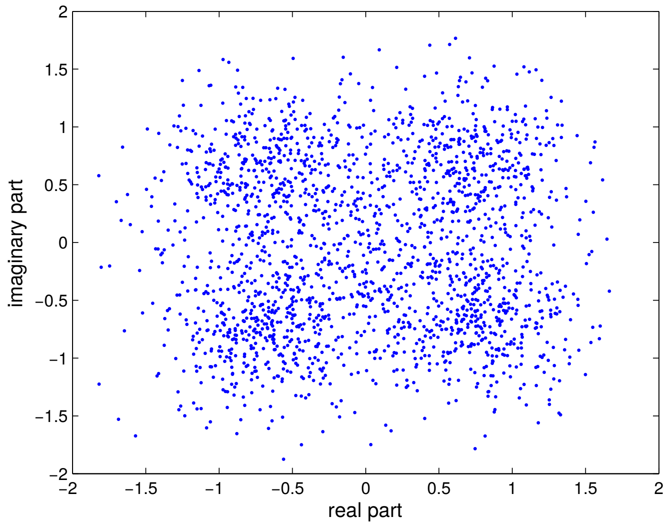

Figure 6.5: Constellation diagram of frequency domain signal before OFDM demodulator shown in Figure 6.1.

lower complexity than the adaptive filters with penalties. With the proposed sliding-window adaptive filter with diagonal loading, the receiver demonstrates the best performance. The constellation diagram of frequency domain signal before the OFDM demodulator is shown in Figure 6.5, from which we can see four clusters.

6.4 Sliding-window Homotopy Adaptive Filter

6.4.1 Adaptive filters

In this section, we describe two homotopy adaptive filters as follows.

1. **Exponential-window homotopy RLS-DCD adaptive algorithm**

   Here, we review the exponential-window homotopy RLS-DCD adaptive algorithm from [136]. In this algorithm, the matrix $\mathbf{D}(n)$ is defined as

   $$\mathbf{D}(n) = \mathrm{diag}[\lambda^{n-1}, \lambda^{n-2}, \ldots, \lambda, 1], \tag{6.20}$$

   where $\lambda \in (0, 1]$ is the forgetting factor. Then, the $N \times N$ matrix $\mathbf{R}(n)$ and $N \times 1$ vector $\mathbf{b}(n)$ can be recursively updated as (6.8) and (6.9) [131].

   The homotopy algorithm minimises the cost function in (6.1). A set of homotopy iterations is performed for exponentially decreasing values of the regularization parameter

τ: $\tau \leftarrow \gamma\tau$; $0 < \gamma < 1$. If the decreasing factor γ is close to one, large number of homotopy iterations are needed, which result in a high complexity. In adaptive filtering, for reducing the complexity, the homotopy iterations are distributed in time, and at every time instance, it is enough to perform only one homotopy iteration [136]. For further reducing the complexity, DCD iterations are used [134, 135]. In a DCD iteration, the previously obtained solution $\mathbf{h}(n-1)$ is used as a warm-start for minimizing the cost function in (6.1), so that the solution for time instant n is sought as:

$$\mathbf{h}(n) = \mathbf{h}(n-1) + \Delta\mathbf{h}(n). \tag{6.21}$$

Then, minimization of the cost function in (6.1) is replaced by minimization of the cost function [133]

$$\frac{1}{2}\Delta\mathbf{h}^H(n)\mathbf{R}(n)\Delta\mathbf{h}(n) - \Re\{\Delta\mathbf{h}^H(n)\mathbf{c}(n, n-1)\} + \tau\mathbf{w}^T(n)|\mathbf{h}(n)| \tag{6.22}$$

with respect to the vector $\Delta\mathbf{h}(n)$, where $\mathbf{c}(n|n-1)$ is a residual vector given by

$$\mathbf{c}(n|n-1) = \mathbf{b}(n) - \mathbf{R}(n)\mathbf{h}(n-1). \tag{6.23}$$

In the exponential-window algorithm, the residual vector $\mathbf{c}(n|n-1)$ is computed as [133, 135]

$$\mathbf{c}(n|n-1) = \lambda\mathbf{c}(n-1|n-1) + e^*(n)\mathbf{x}(n), \tag{6.24}$$

where $\mathbf{c}(n-1|n-1) = \mathbf{b}(n-1) - \mathbf{R}(n-1)\mathbf{h}(n-1)$.

The cost function in (6.22) is minimized using the leading ℓ_1-DCD algorithm from [136]. In the leading ℓ_1-DCD algorithm, a criterion for terminating computations in every iteration is a maximum number of DCD updates N_u. Typically, N_u is set to a small value for limiting the complexity of the algorithm.

2. **Sliding-window homotopy RLS-DCD adaptive algorithm**

In the sliding-window algorithm, the matrix $\mathbf{D}(n)$ can be defined as [131]

$$\mathbf{D}(n) = \begin{pmatrix} \mathbf{0}_{(n-M)\times(n-M)} & \mathbf{0}_{(n-M)\times M} \\ \mathbf{0}_{M\times M} & \mathbf{I}_M \end{pmatrix}, \tag{6.25}$$

where M is the length of the sliding-window and $\mathbf{I}_M$ is an $M \times M$ identity matrix. For a sliding-window RLS problem, the matrix $\mathbf{R}(n)$ and vector $\mathbf{b}(n)$ can be computed from the recursions (6.10) and (6.11) [128].

When minimizing the cost function in (6.22) with respect to the vector $\Delta\mathbf{h}(n)$, the residual vector can now be computed as

$$\mathbf{c}(n|n-1) = \mathbf{c}(n-1|n-1) + e^*(n)\mathbf{x}(n) - e_M^*(n)\mathbf{x}(n-M). \tag{6.26}$$

The other steps are similar to steps of the exponential-window homotopy RLS-DCD adaptive algorithm.

Table 6.3 shows the sliding-window homotopy RLS-DCD adaptive algorithm, where M_b is the number of bits used for representation of entries in the solution vector and defines the accuracy of the fixed-point representation, the weight matrix $\mathbf{w}$ is initialized to an all-ones vector $\mathbf{1}_N$, $e(n) = d(n) - y(n)$ is the error signal, and $y(n) = \mathbf{h}^H(n-1)\mathbf{x}(n)$ is the filter output at time instant n.

6.4.2 Signal processing in the receiver

We apply adaptive filters to channel estimation in a channel-estimate-based linear equalizer (Figure 6.2) of a multi-antenna receiver (Figure 6.6). In a sea trial, a package of guard-free OFDM signals with superimposed pilot signals was transmitted [4].

Figure 6.6 shows a block diagram of the receiver. The signals $r_1(t)$ to $r_M(t)$ from M hydrophones are filtered in a spatial filter, where $r(t, \hat{\theta}_j)$ are directional signals. The directional signals are equalized (see [4] for details) and combined using the maximum-ratio combining (MRC) [107]. The combined signal $\tilde{\mathrm{X}}_l(k)$ is demodulated and further decoded using the soft-decision Viterbi decoding [104].

Table 6.3: Sliding-window homotopy RLS-DCD adaptive algorithm

	Input parameters: M, τ, γ, M_b, N_u, ε
	Output: $\mathbf{h}, \mathbf{c}(n\|n) = \mathbf{c}$
Step	Initialization: $\mathbf{h} = \mathbf{0}$, $I = \emptyset$, $\mathbf{c} = \mathbf{0}$, $\mathbf{b} = \mathbf{0}$, $\mathbf{R} = \varepsilon\mathbf{I}_N$, $\mathbf{w} = \mathbf{1}_N$
	Repeat for $n = 1, 2, \ldots$
1	$\mathbf{R}(n) = \mathbf{R}(n-1) + \mathbf{x}(n)\mathbf{x}^H(n) - \mathbf{x}(n-M)\mathbf{x}^H(n-M)$
2	$\mathbf{b}(n) = \mathbf{b}(n-1) + d^*(n)\mathbf{x}(n) - d^*(n-M)\mathbf{x}(n-M)$
3	$y(n) = \mathbf{h}^H(n-1)\mathbf{x}(n)$
4	$e(n) = d(n) - y(n)$
5	$y_M(n) = \mathbf{h}^H(n-1)\mathbf{x}(n-M)$
6	$e_M(n) = d(n-M) - y_M(n)$
7	$\mathbf{c}(n\|n-1) = \mathbf{c}(n-1\|n-1) + e^*(n)\mathbf{x}(n) - e_M^*(n)\mathbf{x}(n-M)$
8	$\tau = \max_k \|c_k\|$
9	Remove tth element from $I (I \leftarrow I \setminus t)$, if
9.1	$t = \arg\min_{k \in I} \frac{1}{2}\|h_k\|^2 R_{k,k} + \Re\{h_k^* c_k\} - \tau w_k \|h_k\|$
9.2	and $\frac{1}{2}\|h_t\|^2 R_{t,t} + \Re\{h_t^* c_t\} - \tau w_t \|h_t\| < 0$
9.3	If the tth element is removed, then update:
	$\mathbf{c}(n\|n) = \mathbf{c}(n\|n-1) + h_t \mathbf{R}^{(t)}(n)$
10	Include tth element into the support ($I \leftarrow I \cup t$), if
10.1	$t = \arg\max_{k \in I^c} \frac{(\|c_k\| - \tau w_k)^2}{R_{k,k}}$
10.2	and $\|c_t\| > \tau w_t$
11	Update the regularization parameter: $\tau \leftarrow \gamma\tau$
12	Approximately solve the LS-ℓ_1 optimization on the support I using the ℓ_1-DCD algorithm [136]
13	Update the weight vector $\mathbf{w}$

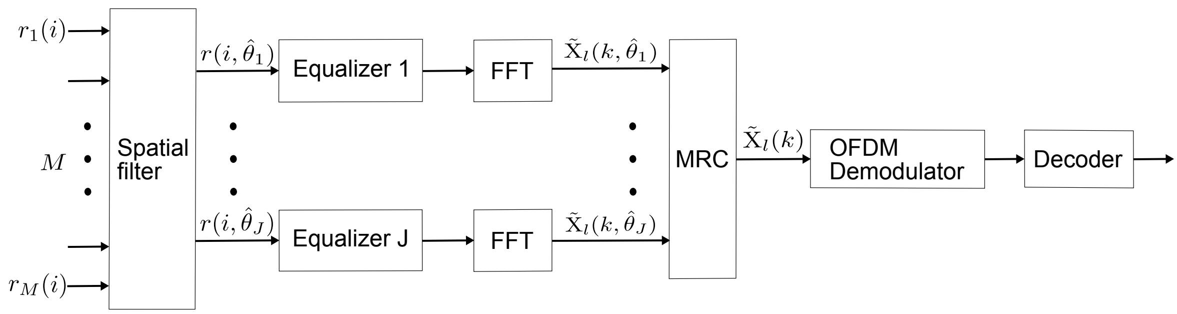

Figure 6.6: Block diagram of the receiver (for convenience, we show Figure 4.4 again).

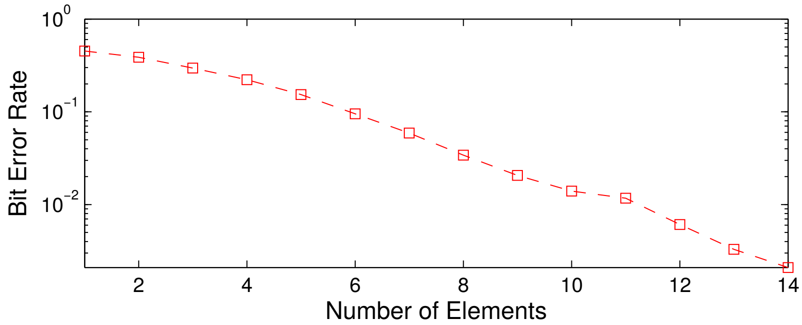

Figure 6.7: Coded BER performance with different number of elements; the convolutional code described by the polynomial in octal [225 331 367].

The equalizer (see Figure 6.2) is implemented using the channel-estimate-based finite impulse response (FIR) scheme with a channel estimator [4]. In the estimator, an adaptive filter is used for the channel estimation [31].

6.4.3 Sea trial results

To verify the effectiveness of the proposed adaptive filter in UWA channels, we applied the exponential-window and sliding-window classic RLS adaptive filters and the two homotopy RLS-DCD adaptive filters for channel estimation in the equalizer shown in Figure 6.2.

In the sea trial, $L = 200$ OFDM symbols were continuously transmitted. The frequency bandwidth of the transmitted signal is 3072 ± 512 Hz. The acoustic transducer was towed at a depth of 250 m by a vessel moved away from a receive VLA of 14 hydrophones at a velocity of 6 m/s; at the start of transmission, the distance between the transducer and receiver was 105 km. The VLA was placed at a depth of 420 m, as shown in Figure 4.1. The distances between the hydrophones are non-uniform (from 0.3 m to 1.2 m) and the length of the VLA is 8.1 m. The BER performance of the receiver applying equalizer directly to hydrophone elements can be seen in Figure 6.7. We can see that as increasing the number of hydrophone elements, the receiver achieves better performance. However, even with 14 elements, the receiver is still unable achieve error-free transmission. This is due to a low SNR on a single hydrophone, as seen in Figure 6.8, which is obtained from the result of the received signal energy divided by recorded noise energy in frames. For this reason, spatial filter is required to pre-process the received signal from the hydrophone elements. In the spatial filter, two

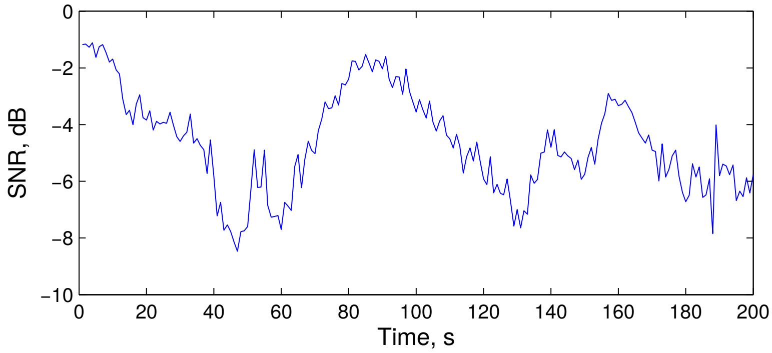

Figure 6.8: SNR at the first hydrophone in the sea trial at a distance of 105 km; for convenience, Figure 4.11 is shown again.

directional signals (for angles of arrival $\hat{\theta}_1 = 8.4°$ and $\hat{\theta}_2 = -9°$) are produced. Figure 4.12(b) and Figure 4.12(c) show fluctuations of the channel impulse response for the two directions, respectively.

In the exponential-window adaptive filters, the forgetting factor is set to $\lambda = 0.998$ and $N = 100$ is the filter length (with a sampling interval of 1 ms for the bandpass signal). The length of the sliding-window $M = 1024$ matches to the length of the OFDM symbol T_s. In the adaptive filters, the number of bits used for representation of the solution vector entries is $M_b = 12$, the number of DCD iterations $N_u = 14$, the regularization parameter $\tau = 3 \times 10^{-4}$, and $\epsilon = 10^{-3}$. Table 6.4 shows BER performance of the receiver with 1/2 and 1/3 convolutional codes and various adaptive filters, and the complexity of the adaptive filters in terms of complex-valued multiplications per sample.

Table 6.4: BER performance of the receiver and complexity of the adaptive filters

Adaptive filters used in the receivers	**BER (1/2)**	**BER (1/3)**	**Complexity** (multiplications)
Classic (Exponential-window)	8.9×10^{-2}	5.4×10^{-3}	$3N^2$
Classic (Sliding-window)	8.6×10^{-2}	4.2×10^{-3}	$5N^2$
Homotopy (Exponential-window)	1.1×10^{-2}	0	$7.5N$
Homotopy (Sliding-window)	1.0×10^{-2}	0	$10.5N$

From Table 6.4, it can be seen that the sliding-window adaptive filters perform better than the exponential-window adaptive filters. Due to the *a priori* information about sparseness

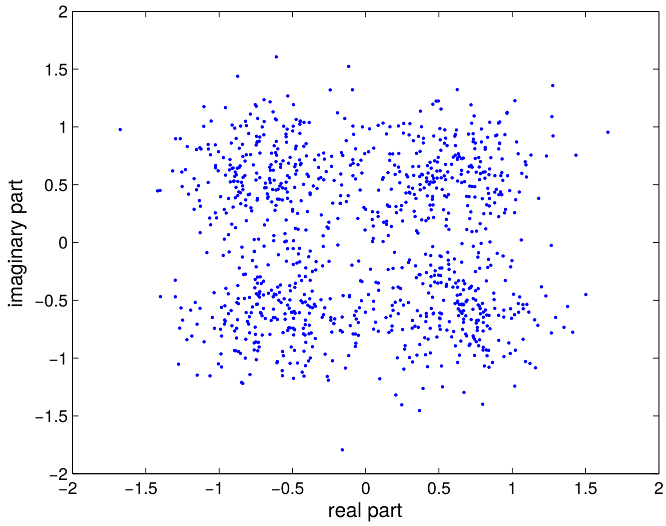

Figure 6.9: Constellation diagram of combined signal $\tilde{X}_l(k)$ before OFDM demodulator shown in Figure 6.6.

taken into account, the homotopy RLS-DCD adaptive filters allow a better performance than the classic RLS adaptive filters. Due to the DCD algorithm taken into account, the homotopy RLS-DCD adaptive filters allow a lower complexity than the classic RLS adaptive filters. The sliding-window homotopy RLS-DCD adaptive filter demonstrates an improved performance at a spectral efficiency of 0.5 bps/Hz and allows error-free transmission at a spectral efficiency of 0.33 bps/Hz. The constellation diagram of combined signal $\tilde{X}_l(k)$ before the OFDM demodulator is shown in Figure 6.9, from which we can see four clusters, even in such low SNR.

6.5 Summary

In this chapter, we proposed two RLS adaptive filters to identify the sparse impulse response in UWA channels. The two adaptive filters are used for channel estimation in two different UWA communication systems with guard-free OFDM signals and superimposed pilot symbols.

The first proposed adaptive filter is based on sliding-window, diagonal loading, and DCD iterations. We have investigated and compared performance of a LMS adaptive filter and six RLS adaptive filters. From the comparison, we have shown that RLS adaptive filters outperform LMS adaptive filter, sliding-window adaptive filters outperform exponential-window adaptive filters, and have shown that the first proposed adaptive filter demonstrates the best performance while its complexity is still only linear in the filter length.

The second proposed adaptive filter is based on sliding-window, homotopy, and DCD iterations. The adaptive filter is used for channel estimation in a multi-antenna based UWA communication system. We have investigated and compared the performance of four RLS adaptive filters, and have shown that the second proposed adaptive filter demonstrates an improved performance compared to other adaptive filters.

Chapter 7

Conclusions and Further Work

Contents

7.1 Summary of the Work

The goal of this thesis is to develop advanced signal processing techniques, suitable for UWA communications with high data rate OFDM transmission. Various signal processing techniques for processing received signals in UWA channels are developed (Chapter 3-6), providing low complexity and high performance; and the *Waymark* UWA channel model is modified (Chapter 2), providing low complexity, and used for simulation (Chapter 3 & 5). Our analysis of the OFDM receivers has provided ample proof that our techniques are capable of improving the performance and reducing the complexity of UWA communication systems.

Chapter 1 provides the necessary background material about underwater acoustic communications and signal processing techniques. Chapter 2 describes the *Waymark* baseband propagation channel model. Chapter 3 describes the multi-channel autocorrelation Doppler estimation method. Chapter 4 investigates the space-time clustering of the channel propagation and applies it to the receiver design. Chapter 5 investigates the direction of arrival (DOA) fluctuation in UWA channels, and proposes a beamforming with DOA tracking. Chapter 6 proposes and compares various recursive least squares (RLS) adaptive filters for channel estimation of sparse impulse responses in UWA channels.

Chapter 2 presents the *Waymark* UWA channel model. This model requires a lower computational complexity than *Waymark* passband UWA propagation model, and the performance of it is comparable to that of a relatively mature UWA propagation channel model (*VirTEX*). This extended work involves developing the channel model and signal representation at the baseband. In this work, a scenario was considered, in which the *Waymark* and *VirTEX* models were compared. The result shows similarity with a qualitative comparison, with the major feature such as the Doppler shifts and delays being the same. This gave us confidence that the results obtained from the *Waymark* channel model are accurate.

Chapter 3 presents a new method based on multi-channel autocorrelation (MCA) for Doppler estimation in fast-varying UWA channels. The proposed method not only measures the time compression over the estimation interval, but also the gradient of the time compression, thus allowing more accurate (with time-varying sampling rate) resampling of the received signal to compensate for the Doppler distortions. The proposed method has been compared with a single-channel autocorrelation (SCA) method and a method based on computing the cross-ambiguity function between the received and pilot signals. The results in shallow water simulation scenarios and in deep ocean sea trials demonstrate that the proposed method outperforms the SCA method, and it is comparable in the performance to the method based on computation of the cross-ambiguity function. However, the proposed method requires significantly less computations, which renders it a good candidate in low complexity UWA applications.

Chapter 4 exploits the space-time clustering in a proposed receiver designed for guard-free OFDM signals with superimposed data and pilot symbols. For separation of space clusters, the receiver utilises a vertical linear array (VLA) of hydrophones, whereas for combining delay-spread signals within a space cluster, a time-domain equalizer is used. A number of space-time processing techniques are compared, including a proposed reduced-complexity spatial filter. The results show that the techniques exploiting the space-time clustering demonstrate an improved detection performance. The comparison is done using signals transmitted by a moving transducer, and recorded on a 14-element non-uniform VLA in a sea trial at a distance of 105 km. At this distance, an error-free data transmission with a spectral efficiency of 0.33 bps/Hz is achieved.

Chapter 5 investigates direction of arrival (DOA) fluctuation in time-varying UWA communication channels, and proposes a beamforming technique with DOA tracking. The DOA fluctuation in UWA channels is investigated from ocean surface and internal waves. The investigation is used to develop a beamforming technique with DOA tracking. The beamforming technique is used in a receiver. The receiver is designed for a communication system using guard-free OFDM signals with superimposed pilot symbols and a 14-element receive VLA. The receiver with this DOA tracking demonstrates an improved detection performance than that without DOA tracking. The comparison is based on data from a simulation at a transmitter/receiver distance of 80 km, and two sea trials at transmitter/receiver distances of 30 km and 105 km.

Chapter 6 proposes two sparse recursive least squares (RLS) adaptive filters and applied them to channel estimation in a high data rate transmission in UWA channels. The first adaptive filter is based on sliding-window, diagonal loading and dichotomous coordinate descent (DCD) iterations, while the second is based on sliding-window, homotopy and DCD iterations. The two adaptive algorithms possess a complexity that only linear in the filter length. The two adaptive filters are used for channel estimation in two different UWA communication systems with guard-free OFDM signals and superimposed pilot symbols. Various RLS adaptive filters are investigated and compared. In the sea trial with a single receive element, the result shows that the first proposed RLS adaptive filter demonstrates better performance than other existing adaptive filters used for comparison. In the sea trial with multiple receive elements, the result shows that the second proposed RLS adaptive filter demonstrates better performance than other existing adaptive filters used for comparison. The results also show that adaptive filters with the sliding-window outperform adaptive filters with the exponential-window. The comparisons have been done using signals recorded in sea trials at distances of 80 km and 105 km transmitted by a fast moving transducers, resulting in fast-varying channels. In these conditions, an error-free data transmission is achieved with a spectral efficiency of 0.33 bps/Hz.

7.2 Future Work

Some suggestions for future work, based on this thesis, are given below:

1. In Chapter 4, a time-frequency-time (TFT) beamforming technique based on minimum variance distortionless response (MVDR) beamforming algorithm in DOA estimator is proposed to estimate the space-time clustering, and to produce directional signals. Similar TFT beamforming techniques based on other beamforming algorithms, such as conventional beamforming algorithm or multiple signal classification (MUSIC) beamforming algorithm, can also be applied and compared. It might be beneficial to the receiver to compare TFT techniques based on different beamforming algorithms, and find the most effective one for achieving the best performance.

2. In Chapters 4 and 5, the space-time clustering in UWA channels is investigated. The investigation is based on two-dimensional (2D) DOA estimation in a spatial filter. However, the DOA can be considered as sparse, and the DOA estimation can be considered as a part of channel estimation. Therefore, designing a channel estimator, which is capable of combining the estimation of the DOA and the channel impulse response, might be beneficial to the performance improvement and complexity reduction of the receiver. The sparse DOA estimation for UWA communications is certainly a topic of further exploration.

3. In this thesis, various advanced signal processing techniques are investigated with the transmission of guard-free OFDM signals with superimposed pilot symbols. These techniques can also be effective in the employment of different signal transmission schemes, e.g., cyclic prefix added OFDM signal transmission.

Glossary

2D	two-**D**imensional
3D	three-**D**imensional
ADC	**A**nalogue-to-**D**igital **C**onverter
AUV	**A**utonomous **U**nderwater **V**ehicles
BER	**B**it **E**rror **R**ate
CAF	**C**ross-**A**mbiguity **F**unction
CP	**C**yclic **P**refix
DAC	**D**igital-to-**A**nalogue **C**onverter
dB	**d**eci**B**el
DCD	**D**ichotomous **C**oordinate **D**escent
DFT	**D**iscrete **F**ourier **T**ransform
DOA	**D**irection **O**f **A**rrival
DT	**D**irection of Arrival **T**racking
ESPRIT	**E**stimation of **S**ignal **P**arameters via **R**otational **I**nvariance **T**echnique
FFT	**F**ast **F**ourier **T**ransform
FIR	**F**inite **I**mpulse **R**esponse
Hz	**H**ert**z**
IFFT	**I**nverse **F**ast **F**ourier **T**ransform
km	kilometre
LMS	**L**east **M**ean **S**quare
LPF	**L**ow **P**ass **F**ilter
LS	**L**east **S**quare
MAC	**M**ultiply-**AC**cumulate operations

MCA	**M**ulti-**C**hannel **A**utocorrelation
ML	**M**aximum **L**ikelihood
MRC	**M**aximal **R**atio **C**ombining
ms	millisecond
MUSIC	**MU**ltiple **SI**gnal **C**lassification
MVDR	**M**inimum **V**ariance **D**istortionless **R**esponse
NLMS	**N**ormalized **L**east **M**ean **S**quare
OFDM	**O**rthogonal **F**requency-**D**ivision **M**ultiplexing
PRBS	**P**seudo-**R**andom **B**inary **S**equence
RLS	**R**ecursive **L**east **S**quares
SCA	**S**ingle-**C**hannel **A**utocorrelation
SD	**S**tatic **D**irection of Arrival
SDM	**S**pectral **D**ensity **M**atrix
SF	**S**patial **F**ilter
SIMO	**S**ingle-**I**nput **M**ultiple-**O**utput
SNR	**S**ignal-to-**N**oise **R**atio
SSP	**S**ound **S**peed **P**rofile
ST	**S**pace-**T**ime
TFT	**T**ime-**F**requency-**T**ime
UUV	**U**nmanned **U**nderwater **V**ehicles
UWA	**U**nder**W**ater **A**coustic
VLA	**V**ertical **L**inear **A**rray

Bibliography

[1] C. Liu, Y. V. Zakharov, and T. Chen, “Doubly Selective Underwater Acoustic Channel Model for a Moving Transmitter/Receiver,” *IEEE Transactions on Vehicular Technology*, vol. 61, no. 3, pp. 938–950, 2012.

[2] R. M. Hamson and R. M. Heitmeyer, “Environmental and system effects on source localization in shallow water by the matched-field processing of a vertical array,” *The Journal of the Acoustical Society of America*, vol. 86, no. 5, pp. 1950–1959, 1989.

[3] D. F. Gingras, “Robust broadband matched-field processing: performance in shallow water,” *IEEE Journal of Oceanic Engineering*, vol. 18, no. 3, pp. 253–264, 1993.

[4] Y. V. Zakharov and A. K. Morozov, “OFDM transmission without guard interval in fast-varying underwater acoustic channels,” *IEEE Journal of Oceanic Engineering*, vol. 40, no. 1, pp. 144–158, 2015.

[5] M. A. Johnstone, “Aristotle on sounds,” *British Journal for the History of Philosophy*, vol. 21, no. 4, pp. 631–648, 2013.

[6] R. E. Hansen, “Introduction to sonar,” *Course Material to INF-GEO4310, University of Oslo*, 2009.

[7] “Discovery of Sound in the Sea,” http://www.dosits.org/people/history/pre1800/, approached on 07/Oct/2016.

[8] J. Heidemann, M. Stojanovic, and M. Zorzi, “Underwater sensor networks: applications, advances and challenges,” *Philosophical Transactions of the Royal Society A: Mathematical, Physical and Engineering Sciences*, vol. 370, no. 1958, pp. 158–175, 2012.

[9] M. Stojanovic, “Underwater acoustic communications,” in *Wiley Encyclopedia of Electrical and Electronics Engineering.*, pp. 688–698, 1998.

[10] M. Chitre, S. Shahabudeen, and M. Stojanovic, "Underwater acoustic communications and networking: Recent advances and future challenges," *Marine technology society journal*, vol. 42, no. 1, pp. 103–116, 2008.

[11] M. Stojanovic, "Underwater acoustic communications," in *Proceedings. Electro/95 International. Professional Program*, pp. 435–440, IEEE, 1995.

[12] M. Stojanovic, "Recent advances in high-speed underwater acoustic communications," *IEEE Journal of Oceanic Engineering*, vol. 21, no. 2, pp. 125–136, 1996.

[13] A. Quazi and W. Konrad, "Underwater acoustic communications," *IEEE Communications Magazine*, vol. 20, no. 2, pp. 24–30, 1982.

[14] M. Chitre, S. Shahabudeen, L. Freitag, and M. Stojanovic, "Recent advances in underwater acoustic communications & networking," in *IEEE OCEANS'08, Quebec*, vol. 2008, pp. 1–10.

[15] D. B. Kilfoyle and A. B. Baggeroer, "The state of the art in underwater acoustic telemetry," *IEEE Journal of Oceanic Engineering*, vol. 25, no. 1, pp. 4–27, 2000.

[16] M. Siderius and M. B. Porter, "Modeling broadband ocean acoustic transmissions with time-varying sea surfaces," *The Journal of the Acoustical Society of America*, vol. 124, p. 137, 2008.

[17] C. R. Berger, S. Zhou, J. C. Preisig, and P. Willett, "Sparse channel estimation for multicarrier underwater acoustic communication: From subspace methods to compressed sensing," *IEEE transactions on Signal Processing*, vol. 58, no. 3, pp. 1708–1721, 2010.

[18] B. Li, S. Zhou, M. Stojanovic, L. Freitag, and P. Willett, "Multicarrier communication over underwater acoustic channels with nonuniform Doppler shifts," *IEEE Journal of Oceanic Engineering*, vol. 33, no. 2, pp. 198–209, 2008.

[19] P. C. Carrascosa and M. Stojanovic, "Adaptive channel estimation and data detection for underwater acoustic MIMO–OFDM systems," *IEEE Journal of Oceanic Engineering*, vol. 35, no. 3, pp. 635–646, 2010.

[20] M. Stojanovic, "MIMO OFDM over underwater acoustic channels," in *2009 Conference Record of the Forty-Third Asilomar Conference on Signals, Systems and Computers*, pp. 605–609, IEEE, 2009.

[21] H. Eghbali, M. Stojanovic, and S. Muhaidat, "Differential decoding for SFBC OFDM systems in underwater MIMO channels," in *IEEE International Conference on Acoustics, Speech and Signal Processing (ICASSP)*, pp. 8102–8105, 2014.

[22] H. Nguyen, Z. Zhao, F. Zheng, and T. Kaiser, "Preequalizer design for spatial multiplexing SIMO-UWB TR systems," *IEEE Transactions on Vehicular Technology*, vol. 59, no. 8, pp. 3798–3805, 2010.

[23] M. Stojanovic, "OFDM for underwater acoustic communications: Adaptive synchronization and sparse channel estimation," in *IEEE International Conference on Acoustics, Speech and Signal Processing*, pp. 5288–5291, 2008.

[24] M. Stojanovic, J. Catipovic, J. G. Proakis, *et al.*, "Phase-coherent digital communications for underwater acoustic channels," *IEEE Journal of Oceanic Engineering*, vol. 19, no. 1, pp. 100–111, 1994.

[25] M. Johnson, L. Freitag, and M. Stojanovic, "Improved Doppler tracking and correction for underwater acoustic communications," in *IEEE International Conference on Acoustics, Speech, and Signal Processing. ICASSP-97.*, vol. 1, pp. 575–578, 1997.

[26] B. S. Sharif, J. Neasham, O. R. Hinton, and A. E. Adams, "A computationally efficient Doppler compensation system for underwater acoustic communications," *IEEE Journal of Oceanic Engineering*, vol. 25, no. 1, pp. 52–61, 2000.

[27] T. J. Riedl and A. C. Singer, "Broadband Doppler compensation: Principles and new results," in *Conference Record of the Forty Fifth Asilomar Conference on Signals, Systems and Computers (ASILOMAR)*, pp. 944–946, IEEE, 2011.

[28] K. A. Perrine, K. F. Nieman, T. L. Henderson, K. H. Lent, T. J. Brudner, and B. L. Evans, "Doppler estimation and correction for shallow underwater acoustic communications," in *IEEE Conference Record of the Forty Fourth Asilomar Conference on Signals, Systems and Computers*, pp. 746–750, 2010.

[29] B. Li, S. Zhou, M. Stojanovic, L. Freitag, and P. Willett, "Non-uniform Doppler compensation for zero-padded OFDM over fast-varying underwater acoustic channels," in *IEEE OCEANS'07-Europe*, pp. 1–6, 2007.

[30] W. Li and J. C. Preisig, "Estimation of rapidly time-varying sparse channels," *IEEE Journal of Oceanic Engineering*, vol. 32, no. 4, pp. 927–939, 2007.

[31] Y. V. Zakharov and A. K. Morozov, “Adaptive sparse channel estimation for guard-free OFDM transmission in underwater acoustic channels,” in *International conference on Underwater Acoustic Measurements: Technologies and Results, 12th European Conference on Underwater Acoustics*, 2013.

[32] Y. V. Zakharov and V. H. Nascimento, “Sparse RLS adaptive filter with diagonal loading,” in *Conference Record of the Forty Sixth Asilomar Conference on Signals, Systems and Computers (ASILOMAR)*, pp. 806–810, IEEE, 2012.

[33] K. Pelekanakis and M. Chitre, “Comparison of sparse adaptive filters for underwater acoustic channel equalization/estimation,” in *IEEE International Conference on Communication Systems (ICCS), Singapore*, pp. 395–399, 2010.

[34] J. Huang, C. R. Berger, S. Zhou, and J. Huang, “Comparison of basis pursuit algorithms for sparse channel estimation in underwater acoustic OFDM,” in *IEEE OCEANS'10-Sydney*, pp. 1–6, 2010.

[35] Z. Xu, Y. Zakharov, and V. P. Kodanev, “Space-time signal processing of OFDM signals in fast-varying underwater acoustic channel,” in *IEEE Oceans'07-Europe*, pp. 1–6, 2007.

[36] M. Stojanovic and J. Preisig, “Underwater acoustic communication channels: Propagation models and statistical characterization,” *IEEE Communications Magazine*, vol. 47, no. 1, pp. 84–89, 2009.

[37] K. T. Wong and M. D. Zoltowski, “Self-initiating MUSIC-based direction finding in underwater acoustic particle velocity-field beamspace,” *IEEE Journal of Oceanic Engineering*, vol. 25, no. 2, pp. 262–273, 2000.

[38] M. Stojanovic, J. A. Catipovic, and J. G. Proakis, “Reduced-complexity spatial and temporal processing of underwater acoustic communication signals,” *The Journal of the Acoustical Society of America*, vol. 98, no. 2, pp. 961–972, 1995.

[39] T. S. Alexander, *Adaptive signal processing: theory and applications.* Springer Science & Business Media, 2012.

[40] S. Ijaz, A. Silva, and S. M. Jesus, “Arrival-based equalizer for underwater communication systems,” *Ucomms'12 Conference, Sestri Levante, Italy*, September, 2012.

[41] A. Amar, Y. Buchris, and M. Stojanovic, “Angle-of-arrival-based detection of underwater acoustic OFDM signals,” in *IEEE 16th International Workshop on Signal Process-*

ing Advances in Wireless Communications (SPAWC), Stockholm, Sweden, pp. 326–330, 2015.

[42] M. Stojanovic, J. Catipovic, and J. G. Proakis, "Adaptive multichannel combining and equalization for underwater acoustic communications," *The Journal of the Acoustical Society of America*, vol. 94, no. 3, pp. 1621–1631, 1993.

[43] M. Stojanovic, L. Freitag, and M. Johnson, "Channel-estimation-based adaptive equalization of underwater acoustic signals," in *IEEE OCEANS'99 Seattle, Washington. Riding the Crest into the 21st Century*, vol. 2, pp. 590–595, 1999.

[44] M. Stojanovic, "Acoustic (underwater) communications," *Encyclopedia of Telecommunications*, 2003.

[45] M. Feder and J. A. Catipovic, "Algorithms for joint channel estimation and data recovery-application to equalization in underwater communications," *IEEE journal of oceanic engineering*, vol. 16, no. 1, pp. 42–55, 1991.

[46] J. G. Proakis, "Adaptive equalization techniques for acoustic telemetry channels," *IEEE Journal of Oceanic Engineering*, vol. 16, no. 1, pp. 21–31, 1991.

[47] M. Stojanovic and L. Freitag, "Hypothesis-feedback equalization for direct-sequence spread-spectrum underwater communications," in *MTS/IEEE OCEANS Conference and Exhibition*, vol. 1, pp. 123–129, 2000.

[48] T. C. Yang and W. B. Yang, "Performance analysis of direct-sequence spread-spectrum underwater acoustic communications with low signal-to-noise-ratio input signals," *The Journal of the Acoustical Society of America*, vol. 123, no. 2, pp. 842–855, 2008.

[49] M. Stojanovic, J. G. Proarkis, J. A. Rice, and M. D. Green, "Spread spectrum underwater acoustic telemetry," in *Proceedings. IEEE OCEANS'98 Conference*, vol. 2, pp. 650–654, 1998.

[50] L. Freitag, M. Stojanovic, S. Singh, and M. Johnson, "Analysis of channel effects on direct-sequence and frequency-hopped spread-spectrum acoustic communication," *IEEE journal of oceanic engineering*, vol. 26, no. 4, pp. 586–593, 2001.

[51] S. Azou, G. Burel, and C. Pistre, "A chaotic direct-sequence spread-spectrum system for underwater communication," in *MTS/IEEE OCEANS'02 Conference*, vol. 4, pp. 2409–2415, 2002.

[52] J. A. Bingham, "Multicarrier modulation for data transmission: An idea whose time has come," *IEEE Communications Magazine*, vol. 28, no. 5, pp. 5–14, 1990.

[53] Y. Zhao and A. Huang, "A novel channel estimation method for OFDM mobile communication systems based on pilot signals and transform-domain processing," in *IEEE 47th Vehicular Technology Conference*, vol. 3, pp. 2089–2093, 1997.

[54] A. Burr, *Modulation and coding for wireless communications.* Pearson Education, 2001.

[55] E. Bejjani and J. C. Belfiore, "Multicarrier coherent communications for the underwater acoustic channel," in *Proceedings. MTS/IEEE OCEANS'96. Prospects for the 21st Century. Conference, Fort Lauderdale, Florida*, vol. 3, pp. 1125–1130, 1996.

[56] W. K. Lam and R. F. Ormondroyd, "A coherent COFDM modulation system for a time-varying frequency-selective underwater acoustic channel," in *IET Proceedings of Seventh International Conference on Technology Transfer from Research to Industry, Electronic Engineering in Oceanography*, June, 1997.

[57] Y. V. Zakharov and V. P. Kodanev, "Multipath-Doppler diversity of OFDM signals in an underwater acoustic channel," in *Proceedings IEEE International Conference on Acoustics, Speech, and Signal Processing. ICASSP'00.*, vol. 5, pp. 2941–2944, 2000.

[58] B. C. Kim and I. T. Lu, "Parameter study of OFDM underwater communications system," in *MTS/IEEE Oceans'00 Conference and Exhibition*, vol. 2, pp. 1251–1255, 2000.

[59] M. Stojanovic, "Low complexity OFDM detector for underwater acoustic channels," in *IEEE OCEANS'06*, pp. 1–6.

[60] Y. V. Zakharov and V. P. Kodanev, "Experimental study of an underwater acoustic communication system with pseudonoise signals," *Acoustical Physics*, vol. 40, no. 5, pp. 707–715, 1994.

[61] Y. V. Zakharov and V. P. Kodanev, "Doppler scattering adaptive reception in a hydroacoustic communication channel," *Journal of Acoustical Physics*, vol. 41, no. 2, pp. 219–223, 1995.

[62] J. K. Tugnait and X. Meng, "On superimposed training for channel estimation: performance analysis, training power allocation, and frame synchronization," *IEEE Transactions on Signal Processing*, vol. 54, no. 2, pp. 752–765, 2006.

[63] V. P. Kodanev and Y. V. Zakharov, "Experimental research of underwater acoustic long-range transmission of high-rate data," *Le Journal de Physique IV*, vol. 4, no. C5, pp. C5–1105, 1994.

[64] P. A. Walree, "Propagation and scattering effects in underwater acoustic communication channels," *IEEE Journal of Oceanic Engineering*, vol. 38, no. 4, pp. 614–631, 2013.

[65] J. C. Peterson and M. B. Porter, "Ray/beam tracing for modeling the effects of ocean and platform dynamics," *IEEE Journal of Oceanic Engineering*, vol. 38, no. 4, pp. 655–665, 2013.

[66] P. Qarabaqi and M. Stojanovic, "Statistical characterization and computationally efficient modeling of a class of underwater acoustic communication channels," *IEEE Journal of Oceanic Engineering*, vol. 38, no. 4, pp. 701–717, 2013.

[67] M. B. Porter, "The Bellhop manual and user's guide: Preliminary draft," *Heat, Light, and Sound Research, Inc., La Jolla, CA, USA, Tech. Rep*, 2011.

[68] M. B. Porter, "The KRAKEN normal mode program," tech. rep., DTIC Document, 1992.

[69] M. B. Porter and H. P. Bucker, "Gaussian beam tracing for computing ocean acoustic fields," *The Journal of the Acoustical Society of America*, vol. 82, no. 4, pp. 1349–1359, 1987.

[70] X. Geng and A. Zielinski, "An eigenpath underwater acoustic communication channel model," in *MTS/IEEE Proceedings OCEANS'95. Challenges of Our Changing Global Environment, San Diego, California.*, vol. 2, pp. 1189–1196, 1995.

[71] R. Otnes, P. A. Walree, and T. Jenserud, "Validation of replay-based underwater acoustic communication channel simulation," *IEEE Journal of Oceanic Engineering*, vol. 38, no. 4, pp. 689–700, 2013.

[72] W. Tranter, K. Shanmugan, T. Rappaport, and K. Kosbar, *Principles of communication systems simulation with wireless applications.* Prentice Hall Press, 2003.

[73] M. Stojanovic, "Underwater acoustic communications: Design considerations on the physical layer," in *IEEE Fifth Annual Conference on Wireless on Demand Network Systems and Services, Garmisch-Partenkirchen, Germany.*, pp. 1–10, 2008.

[74] K. Gentile, "The care and feeding of digital, pulse-shaping filters," *RF DESIGN*, vol. 25, no. 4, pp. 50–58, 2002.

[75] G. L. Stüber, *Principles of mobile communication.* Kluwer Academic (Boston), 1996.

[76] M. Unser, A. Aldroubi, and M. Eden, "B-spline signal processing. I. Theory," *IEEE transactions on signal processing*, vol. 41, no. 2, pp. 821–833, 1993.

[77] G. Bertolotto, T. Jenserud, and P. Walree, *Initial design of an acoustic communication channel simulator.* Citeseer, 2007.

[78] S. Stein, "Algorithms for ambiguity function processing," *IEEE Transactions on Acoustics, Speech and Signal Processing*, vol. 29, no. 3, pp. 588–599, 1981.

[79] S. W. Golomb *et al.*, *Shift register sequences.* Aegean Park Press, 1982.

[80] N. S. Alagha and P. Kabal, "Generalized raised-cosine filters," *IEEE transactions on Communications*, vol. 47, no. 7, pp. 989–997, 1999.

[81] S. Yerramalli and U. Mitra, "Optimal resampling of OFDM signals for multiscale–multilag underwater acoustic channels," *IEEE Journal of Oceanic Engineering*, vol. 36, no. 1, pp. 126–138, 2011.

[82] G. Eynard and C. Laot, "Blind Doppler compensation scheme for single carrier digital underwater communications," in *IEEE OCEANS'08, Quebec*, pp. 1–5, 2008.

[83] J. S. Dhanoa and R. F. Ormondroyd, "Combined differential Doppler and time delay compensation for an underwater acoustic communication system," in *MTS/IEEE OCEANS'02, Biloxi, MI, USA*, vol. 1, pp. 581–587, 2002.

[84] S. F. Mason, C. R. Berger, S. Zhou, and P. Willett, "Detection, synchronization, and Doppler scale estimation with multicarrier waveforms in underwater acoustic communication," *IEEE Journal on Selected Areas in Communications*, vol. 26, no. 9, pp. 1638–1649, 2008.

[85] A. Y. Kibangou, C. Siclet, and L. Ros, "Joint channel and Doppler estimation for multicarrier underwater communications," in *ICASSP*, pp. 5630–5633, 2010.

[86] X. Xu, Z. Wang, S. Zhou, and L. Wan, "Parameterizing both path amplitude and delay variations of underwater acoustic channels for block decoding of orthogonal frequency

division multiplexing," *The Journal of the Acoustical Society of America*, vol. 131, no. 6, pp. 4672–4679, 2012.

[87] Z. Wang, S. Zhou, J. C. Preisig, K. R. Pattipati, and P. Willett, "Clustered adaptation for estimation of time-varying underwater acoustic channels," *IEEE Transactions on Signal Processing*, vol. 60, no. 6, pp. 3079–3091, 2012.

[88] N. Santos, A. Matos, and N. Cruz, "Navigation of an autonomous underwater vehicle in a mobile network," *IEEE OCEANS'08, Quebec*, vol. 1-4, 2008.

[89] R. N. Smith, Y. Chao, B. H. Jones, D. A. Caron, P. P. Li, and G. S. Sukhatme, "Trajectory design for autonomous underwater vehicles based on ocean model predictions for feature tracking," in *Field and Service Robotics*, pp. 263–273, Springer, 2010.

[90] B. He, H. Zhang, C. Li, S. Zhang, Y. Liang, and T. Yan, "Autonomous navigation for autonomous underwater vehicles based on information filters and active sensing," *Sensors*, vol. 11, no. 11, pp. 10958–10980, 2011.

[91] F. García C., A. Guerrero G., *et al.*, "Intelligent navigation for a solar powered unmanned underwater vehicle," *International Journal of Advanced Robotic Systems*, vol. 10, p. 185, 2013.

[92] O. Gal, "Unified trajectory planning algorithms for autonomous underwater vehicle navigation," *ISRN Robotics*, vol. 2013, 2013.

[93] J. McColgan and E. W. McGookin, "Coordination of multiple biomimetic autonomous underwater vehicles using strategies based on the schooling behaviour of fish," *Robotics*, vol. 5, no. 1, p. 2, 2016.

[94] N. Parrish, S. Roy, and P. Arabshahi, "Symbol by symbol Doppler rate estimation for highly mobile underwater OFDM," in *Proceedings of the Fourth ACM International Workshop on UnderWater Networks, Berkeley, CA, USA*, pp. 1–8, ACM, Nov. 2009.

[95] T. C. Yang, "Underwater telemetry method using Doppler compensation," Jan. 28 2003. US Patent 6,512,720.

[96] L. Wan, Z. Wang, S. Zhou, T. C. Yang, and Z. Shi, "Performance comparison of Doppler scale estimation methods for underwater acoustic OFDM," *Journal of Electrical and Computer Engineering*, p. 1, 2012.

[97] T. Arikan, T. Riedl, A. Singer, and J. Younce, "Comparison of OFDM and single-carrier schemes for Doppler tolerant acoustic communications," in *IEEE OCEANS-2015, Genova*, pp. 1–7, 2015.

[98] G. Jourdain, "Characterization of the underwater channel application to communication," in *Issues in Acoustic Signal-Image Processing and Recognition*, pp. 197–209, Springer, 1983.

[99] S. M. Kay and S. B. Doyle, "Rapid estimation of the range-Doppler scattering function," *IEEE transactions on Signal Processing*, vol. 51, no. 1, pp. 255–268, 2003.

[100] A. E. Abdelkareem, B. S. Sharif, C. C. Tsimenidis, J. A. Neasham, and O. R. Hinton, "Low-complexity doppler compensation for OFDM-based underwater acoustic communication systems," in *IEEE OCEANS'11-Spain*, pp. 1–6, 2011.

[101] A. E. Abdelkareem, B. S. Sharif, and C. C. Tsimenidis, "Adaptive time varying Doppler shift compensation algorithm for OFDM-based underwater acoustic communication systems," *Ad Hoc Networks*, vol. 45, pp. 104–119, 2016.

[102] W. W. S. Wei, *Time series analysis.* Addison-Wesley publ Reading, 1994.

[103] I. S. Gradshteyn and I. M. Ryzhik, *Table of integrals, series, and products.* Academic Press, Inc., San Diego, CA, 2000.

[104] J. G. Proakis, "Digital communications. 1995," *McGraw-Hill, New York.*

[105] P. Sweeney, *Error control coding.* Prentice Hall UK, 1991.

[106] M. Pajovic and J. C. Preisig, "Performance analysis and optimal design of multichannel equalizer for underwater acoustic communications," *IEEE Journal of Oceanic Engineering*, vol. 40, no. 4, pp. 759–774, 2015.

[107] D. G. Brennan, "Linear diversity combining techniques," *Proceedings of the IRE*, vol. 47, no. 6, pp. 1075–1102, 1959.

[108] S. Zhou and Z. Wang, *OFDM for Underwater Acoustic Communications.* John Wiley & Sons, 2014.

[109] K. T. Wong and M. D. Zoltowski, "Extended-aperture underwater acoustic multi-source azimuth/elevation direction-finding using uniformly but sparsely spaced vector hydrophones," *IEEE Journal of Oceanic Engineering*, vol. 22, no. 4, pp. 659–672, 1997.

[110] S. Yerramalli and U. Mitra, “On optimal resampling for OFDM signaling in doubly-selective underwater acoustic channels,” in *IEEE OCEANS'08, Quebec*, pp. 1–6, 2008.

[111] S. Haykin, J. H. Justice, N. L. Owsley, J. L. Yen, and A. C. Kak, *Array signal processing*. Prentice-Hall, Inc., Englewood Cliffs, NJ, 1985.

[112] J. Capon, “High-resolution frequency-wavenumber spectrum analysis,” *Proceedings of the IEEE*, vol. 57, no. 8, pp. 1408–1418, 1969.

[113] H. Krim and M. Viberg, “Two decades of array signal processing research: the parametric approach,” *IEEE Signal Processing Magazine*, vol. 13, no. 4, pp. 67–94, 1996.

[114] M. Li, “Advanced array processing techniques and systems,” *International Journal of Computer Research*, vol. 17, no. 4, pp. 381–414, 2009.

[115] T. H. Eggen, A. B. Baggeroer, and J. C. Preisig, “Communication over Doppler spread channels. part I: Channel and receiver presentation,” *IEEE Journal of Oceanic Engineering*, vol. 25, no. 1, pp. 62–71, 2000.

[116] F. H. Hsu, K. A. Blenkarn, *et al.*, “Analysis of peak mooring force caused by slow vessel drift oscillation in random seas,” in *Second annual Offshore Technology Conference, Houston*, April 22-24, 1970.

[117] O. M. Faltinsen and A. E. Løken, “Slow drift oscillations of a ship in irregular waves,” *Applied Ocean Research*, vol. 1, no. 1, pp. 21–31, 1979.

[118] J. A. Pinkster, “Mean and low frequency wave drifting forces on floating structures,” *Ocean Engineering*, vol. 6, no. 6, pp. 593–615, 1979.

[119] G. F. M. Remery, A. J. Hermans, *et al.*, “The slow drift oscillations of a moored object in random seas,” *Society of Petroleum Engineers Journal*, vol. 12, no. 03, pp. 191–198, 1972.

[120] C. Garrett and W. Munk, “Internal waves in the ocean,” *Annual Review of Fluid Mechanics*, vol. 11, no. 1, pp. 339–369, 1979.

[121] R. Salmon, “Introduction to ocean waves,” *Scripps Institution of Oceanography, University of California, San Diego*, 2008.

[122] A. Techet, “Free-Surface Waves,” *Department of Mechanical Engineering, Massachusetts Institute of Technology*, 2005.

[123] S. M. Flatté and G. Rovner, "Calculations of internal-wave-induced fluctuations in ocean-acoustic propagation," *The Journal of the Acoustical Society of America*, vol. 108, no. 2, pp. 526–534, 2000.

[124] R. Dashen, S. M. Flatté, W. H. Munk, K. M. Watson, and F. Zachariasen, *Sound transmission through a fluctuating ocean.* Cambridge University Press, 2010.

[125] S. R. Massel, *Ocean surface waves: Their physics and prediction*, vol. 11. World scientific, 1996.

[126] J. Benesty, J. Chen, Y. Huang, and I. Cohen, "Pearson correlation coefficient," in *Noise reduction in speech processing*, pp. 1–4, Springer, 2009.

[127] C. E. Shannon, "Communication in the presence of noise," *Proceedings of the IRE*, vol. 37, no. 1, pp. 10–21, 1949.

[128] G. C. Goodwin and R. L. Payne, "Dynamic system identification: experiment design and data analysis," 1977.

[129] G. Carayannis, D. G. Manolakis, and N. Kalouptsidis, "A fast sequential algorithm for least-squares filtering and prediction," *IEEE Transactions on Acoustics, Speech and Signal Processing*, vol. 31, no. 6, pp. 1394–1402, 1983.

[130] J. M. Cioffi and T. Kailath, "Fast, recursive-least-squares transversal filters for adaptive filtering," *IEEE Transactions on Acoustics, Speech and Signal Processing*, vol. 32, no. 2, pp. 304–337, 1984.

[131] S. S. Haykin, *Adaptive Filtering, 2nd.* Englewood Cliffs, NJ, USA:Prentice Hall, 1991.

[132] A. H. Sayed, *Fundamentals of adaptive filtering.* John Wiley & Sons, 2003.

[133] Y. V. Zakharov and V. H. Nascimento, "DCD-RLS adaptive filters with penalties for sparse identification," *IEEE Transactions on Signal Processing*, vol. 61, no. 12, pp. 3198–3213, 2013.

[134] Y. V. Zakharov and T. C. Tozer, "Multiplication-free iterative algorithm for LS problem," *Electronics Letters*, vol. 40, no. 9, pp. 567–569, 2004.

[135] Y. V. Zakharov, G. P. White, and J. Liu, "Low-complexity RLS algorithms using dichotomous coordinate descent iterations," *IEEE Transactions on Signal Processing*, vol. 56, no. 7, pp. 3150–3161, 2008.

[136] Y. V. Zakharov and V. H. Nascimento, "Homotopy RLS-DCD adaptive filter," in *Proceedings of the Tenth International Symposium on Wireless Communication Systems (ISWCS)*, pp. 1–5, VDE, 2013.

[137] B. Babadi, N. Kalouptsidis, and V. Tarokh, "SPARLS: The sparse RLS algorithm," *IEEE Transactions on Signal Processing*, vol. 58, no. 8, pp. 4013–4025, 2010.

[138] Y. Murakami, M. Yamagishi, M. Yukawa, and I. Yamada, "A sparse adaptive filtering using time-varying soft-thresholding techniques," in *IEEE International Conference on Acoustics Speech and Signal Processing (ICASSP)*, pp. 3734–3737, 2010.

[139] S. Makino, Y. Kaneda, and N. Koizumi, "Exponentially weighted stepsize NLMS adaptive filter based on the statistics of a room impulse response," *IEEE transactions on speech and audio processing*, vol. 1, no. 1, pp. 101–108, 1993.